PROTOTYPE SYSTEM FOR AUTONOMOUS DETECTION AND EXTRACTION OF
FLOATING POLLUTION FROM AQUATIC ENVIRONMENTS

by

Jeremy McKenzie Brake

A thesis submitted to the faculty of
The University of North Carolina at Charlotte
in partial fulfillment of the requirements
for the degree of Master of Science in
Applied Energy and Electromechanical Systems

Charlotte

2021

Approved by:

_____
Dr. Aidan Browne

_____
Dr. Elizabeth Smith

_____
Dr. Michael Smith

ABSTRACT

JEREMY MCKENZIE BRAKE. Prototype System for Autonomous Detection and Extraction of Floating Pollution from Aquatic Environments. (Under the direction of DR. AIDAN F. BROWNE)

This research aims to develop an autonomous system for pollution acquisition and extraction within waterways. Currently, there are approximately 270,000 tons of pollution within the world's oceans, with 80% originating from inland waterways. The environmental effects of this include marine mammals, fish, sea birds, and even coral. As the amount of pollution continues to increase, the need for a solution has never been greater. The proposed design provides a potential solution to alleviate the problem near the source (inland waterways). To accomplish this, a system prototype was created using an unmanned surface vehicle (USV) accompanied by a suite of sensors, allowing for object recognition and extraction. Two vision systems were used, one to provide object localization and the other to verify pollution upon extraction. The control system used information extracted from the object discovery system to provide heading commands to the unmanned surface vehicle. The control system also utilized an extraction mechanism that removes pollution from the environment upon detection and deposits it onto the USV. The USV prototype successfully detected, maneuvered, and extracted five different pollution samples from an aquatic environment.

DEDICATION

I would first like to dedicate this thesis to my parents, brother and grandmother for pushing me to always follow my dreams and that anything is possible. I would also like to dedicate this to my fiancé, who always provided unwavering love and support to keep me going even when times were tough. Finally, for my late grandfather, who instilled in me the values of hard work and determination. It is thanks to them that I was able to follow my passion and achieve things I never dreamed possible.

ACKNOWLEDGEMENTS

TABLE OF CONTENTS

LIST OF TABLES

LIST OF FIGURES

LIST OF ABBREVIATIONS

USV   Unmanned Surface Vehicle

UNEP   United Nations Environment Program

NOAA   National Oceanic and Atmospheric Administration

ASV   Autonomous Surface Vehicle

ASC   Autonomous Surface Craft

CPU   Central Processing Unit

AEEO   Assembler Encoding with Evolvable Operations

CCENN   Cooperative Co-Evolutionary Neural Networks

PTT   Platform transmitters terminals

ANN   Artificial Neural Networks

IKF   Interval Kalman filter

KF   Kalman filter

UKF   Unscented Kalman Filter

EKF   Extended Kalman Filter

IMU   Inertial Measurement Unit

3D   Three-Dimensional

RSDC   RealSense Depth Camera

RGB   Red Green Blue

VRM   Voltage Regulated Module

GPS   Global Positioning System

NI   National instruments

ROI   Region of Interest

IMAQ   Image Acquisition

FOV   Field of View

AM   Additive Manufacturing

OLARP   Object Localization Acquisition robot prototype

AGM   Absorbent Glass Mat

DC   Direct Current

IP   Internet Protocol

PWM   Pulse Width Modulation

AOA   Angle of Attack

ADPS   Adjusted Degrees Per Step

ft   Feet

ft-lbs   foot-pounds

in   inches

oz   Ounce

m	Meter
s	Seconds
km	Kilometers
kg	Kilogram
V	Volts
A	Amps
Ah	Amp-Hour
mA	milli-Amps

CHAPTER 1: INTRODUCTION

1.1   Problem Statement

Over the past five decades, the world's yearly consumption of plastic products has increased from 2 million tons to a staggering 350 million. In this process, the world's oceans have seen a steady increase in plastic pollution. This ever-increasing problem threatens aquatic life and the marine environment more than ever. However, this problem does not start in the world's oceans; it starts upstream, in inland waterways such as lakes, rivers, and canals. A recent study showed that 80 percent of pollution located in the world's oceans originated upstream, and 90 percent of that pollution was deposited by ten major river systems.

 At present, acquisition of this pollution is done mainly through passive collection systems or large-scale extraction devices, all involving human intervention. Passive designs utilize a barrier system that stops debris as it moves downstream and guides it to a central catch basin to be extracted. This design can be seen in "The Bubble Barrier" and New Naval's Tactical Recovery Accumulation System Hellas [1]. The other primary collection method is the use of large-scale extraction devices. A newer approach to the problem was introduced by The Ocean Cleanup Organization in the Netherlands. This device is capable of extracting up to 50,000 kg of pollution a day. However, this design is extremely limited due to two main issues, size and automation.

Today's technology offers a unique solution for detecting, locating, and removing pollution debris from the world's inland waterways. The primary focus of this research is autonomous debris detection and acquisition within aquatic environments using a vision-guided unmanned surface vehicle (USV). Object detection within aquatic environments offers many challenges, including ever-changing environments, water reflection, object presentation, size variations, and

processing speed. This limits the ability to use machine learning capabilities to recognize specific shapes and make decisions based on them. In this research, video is streamed into a localized processing unit from an Intel RealSense depth camera. The processing unit controls all post-processing algorithms applied to captured video with the goal of filtering out any excess information within the video.

There are four major systems of this project: frame, discovery, controls, extraction. The frame is where all electronics and controls are located. It is the limiting factor for the overall size of debris captured and how much can be stored. Due to funding, a previously purchased platform was used for this system. The discovery system was utilized to identify debris and its location relative to the platform. The third system, controls, allow the USV to maneuver towards the located object. Finally, the extraction system is comprised of two subsystems. The first is the extraction mechanism designed to capture the most commonly found plastic debris. The size of this debris varies from a 16 oz aluminum can (5 in by 3 in) to a 2-liter plastic bottle (12 in by 5 in). The second subsystem is for capture verification. This comprises a camera that is utilized to verify that the scooping mechanism successfully captured the debris.

Plastic pollutions affect ranges far and wide throughout the world's oceans. It affects fish, sea birds, sea turtles, marine mammals, and even coral. As evidence of these effects becomes apparent, the need for a solution has never been greater. This research aims to provide a valued solution by implementing autonomous features working jointly to remove plastic waste from aquatic environments.

<center>1.2   Objectives and Scope</center>

The objectives of the study were as follows:

<center>2</center>

- Implement an object recognition (discovery) system that can identify "sample pollutants" along the surface of an aquatic environment.

- Deploy control suite to allow USV to maneuver towards detected object's location for extraction from the environment.

- Once the "sample pollutant" is located, develop a waste disposal mechanism to remove and extract the content from the water *(aluminum can (5 in by 3 in) to a 2-liter plastic bottle (12 in by 5 in))*.

- During deployment of the waste disposal mechanism, verify that the located floating debris was extracted from the environment.

- Implement the above four systems working collectively to accomplish the designated task of removing "sample pollutant" from an aquatic environment.

1.3 Organization of Thesis

The thesis is organized into seven chapters. The first chapter explains the motivation behind the research and presents the objectives and scope of this project. Chapter two presents a review of previous work done on robotic sensing and visual recognition. Chapter three provides a system overview of the design concept. Chapter four introduces the methodology of each system used in the proposed design. Chapter five provides test procedures for each test conducted in this research. Chapter six includes the results from each of the previously discussed tests in chapter five, followed by a discussion of the results. The last chapter discusses the overall results of the autonomous functions working collectively to fulfill the objectives of this thesis.

CHAPTER 2: LITERATURE REVIEW

2.1   Defining Plastic Pollution and Where it Originates

The first step in identifying possible solutions to an ever-growing problem is to define the problem. As plastic products continue to be utilized, there is an increase in the amount of accumulated waste. One of the significant issues surrounding plastic is the extremely long lifespan between 300 to1000 years, resulting in an ever-growing problem. For example, the average use of a plastic bag is approximately 12 minutes. However, it may take up to 100 years for that bag to degrade in a landfill [2]. Plastic that does not make it to the landfill or is not recycled must end up deposited somewhere, and this place is typically the world's ocean. Plastic pollution can be described as the "accumulation of plastic products in the environment that adversely affects wildlife, its habitat and humans" [3].

2.1.1   Current and Future Problems

Currently, it is estimated that by the year 2050, there will be over 12 billion metric tons of plastic pollution in the world's oceans [2]. This is due to the exponential growth of the use of plastic products over the past six decades. In the early 1950s, approximately 2 million metric tons of plastic were created annually, and as of 2015, plastic production is at an astonishing 380 million metric tons per year. Components of this plastic pollution include microbeads and microfibers, plastic containers, discarded fishing lines and nets, plastic office tools, cellophane, food wrappers, straws, smoking paraphernalia, and plastic bags [4].One publication suggests there are approximately 270,000 tons of plastic pollution afloat in the world's oceans [5].
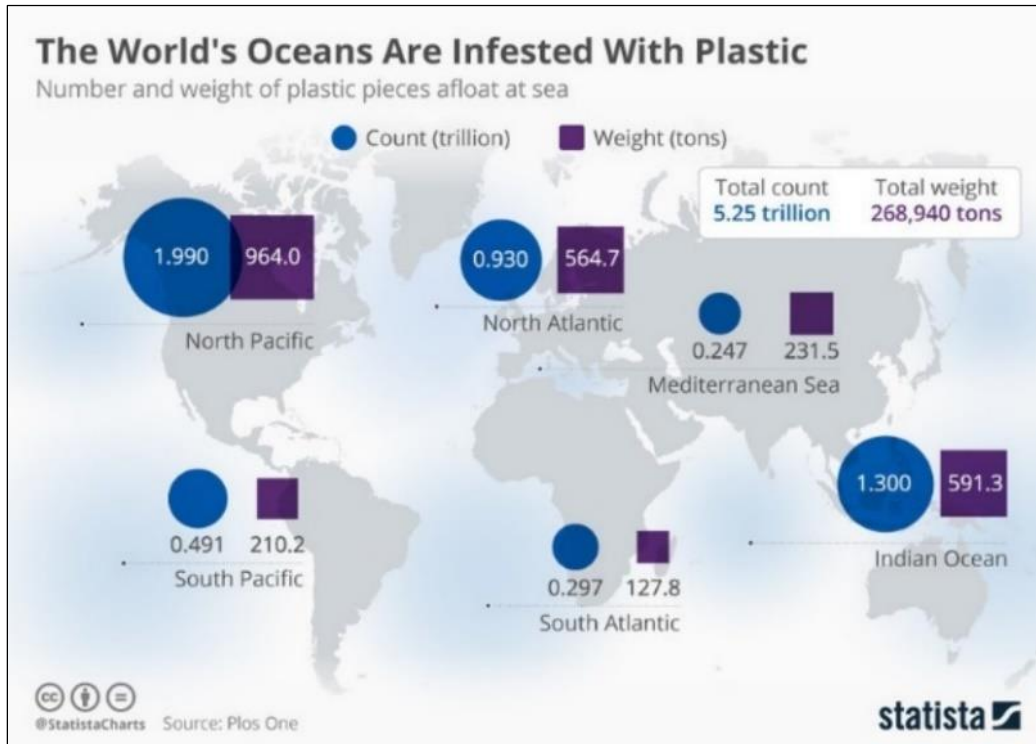
FIGURE 2-1: Breakdown of pollution afloat per location [6]

FIGURE 2-1 provides a detailed breakdown of the approximate count and weight of plastic

pollution afloat at sea. This figure also suggests that most of the pollution is located in the North

Pacific and Indian Oceans.

2.1.2   Origins of Pollution

Though most pollution ends up in the ocean, this is not where a majority of it originated.

A recent study [7] shows that 80% of the plastic is washed into the ocean by rivers, with ten

major river systems contributing 90% of all plastic. This is directly related to how river systems

are interlinked with the marine environment by river discharge areas. This means that all the

plastic pollution accumulated through inland waterways across each country will eventually lead

to the ocean if certain precautions or countermeasures are not in place. In a recent study, mass

estimates of plastic pollution carried by waterways can range from less than one kilogram a day

(Hilo, Hawaii) to as much as 4,200 kilograms per day (Danube River) [8]. The amount of plastic

pollution within these waterways directly correlates with local watershed characteristics, local laws on recycling, the population along the river, and the overall length and size of the waterway.

As plastic enters the ocean, new challenges arise in collecting and removing it from the marine environment. This is especially true the further away from the coast it gets. Removing the pollution before it reaches the ocean can reduce the overall effect on marine wildlife and the surrounding environment. A recent study showed that all known species of sea turtles, 54% of all species of marine mammals, 0.68% of Fish, and 56% of all seabirds were affected by either entanglement or ingestion of plastic pollution [9]. This is an increase compared to a study by Laist done in 1997 where the rate was 86%, 49%, 0.36%, and 44%, respectively [10]. Plastic pollution is also responsible for over one million seabirds and over 100,000 marine mammal deaths each year [11].

2.1.3   Microplastics, Mesoplastics, and Macroplastics

Plastic pollution can be classified into three separate categories, microplastics, mesoplastics, and macroplastics. These three categories can be broken down by the size of the plastic debris: <5 mm (microplastic), 5 mm to 25 cm (mesoplastic), and >25 mm (macroplastic). This size standard has been adopted by the United Nations Environment Program (UNEP) [12], Marine Strategy Framework Directive technical subgroup on marine litter [13], and also by the National Oceanic and Atmospheric Association (NOAA) [14]. TABLE 2-1 confirms these accepted standards by analyzing other research conducted in this field of study. These standards are not the same when the research team combines meso- and macro- plastics into one category.

TABLE 2-1: Reference Studies focusing on Different plastic sizes and their relative definitions

Reference	Use of Microplastic	Use of Mesoplastic	Use of Macroplastic	Size Definition Microplastic	Size Definition Mesoplastic	Size Definition Macroplastic
[15]	X	X	X	<5 mm	5mm< >25mm	>25 mm
[16]	X	X	X	<5 mm	5mm< >25mm	>25 mm
[17]	-	-	X	-	-	> 5mm
[18]	X	-	X	<5 mm	-	> 5mm
[19]	X	X	X	<5 mm	5mm< >25mm	>25 mm
[20]	X	X	X	<5 mm	5mm< >25mm	>25 mm
[21]	X	X	X	<5 mm	5mm< >25mm	>25 mm
[22]	X	-	X	<5 mm	-	> 5mm
[23]	-	-	X	-	-	> 5mm
[14]	X	X	X	<5 mm	5mm< >25mm	>25 mm
[12]	X	X	X	<5 mm	5mm< >25mm	>25 mm
[13]	X	X	X	<5 mm	5mm< >25mm	>25 mm

Macro plastics tend to be located at or near the surface of the water and typically consist of intact plastic items and packaging as well as fragments of plastic. However, density varies between different plastic polymers resulting in some plastics sinking to the sea floor [24]. Mesoplastics

tend to be larger fragments of macroplastics that have not yet reached the size to be considered

microplastic. Microplastics are the fragmented product of macro- and meso- plastics and are

primarily created under various environmental processes such as biodegradation,

photodegradation, thermal-oxidative degradation, and hydrolysis [25]. Due to the size of these

particles and ease of transportation via currents, they tend to be harder to track and capture.

2.2   Current Methods of Tracking and Acquiring Pollution

2.2.1   Tracking

As technology continues to improve, new methods arise in the fight to track plastic

pollution. One of the most used methods is the utilization of satellites to track drifts and currents.

This method can utilize platform transmitters terminals (PTT) which include an antenna, radio

frequency modulator, power amplifier, message generation logic, a sensor interface unit, an

ultra-stable oscillator, and power supply. This transmitter is designed to drift along the surface of

the water, similar to plastic pollution. This method transmits location and sensor data to an Argos

satellite equipped with a receiver that can store the data. Many types of PTT's are currently

being used for plastic pollution tracking, marine wildlife tracking, managing marine resources,

fisheries, detecting oil spills, and many other applications. Each PTT must be by CLS/Service

Argos so that there is no interference with previously deployed PTT's. One specific PTT is the

MAR-GE/T. This PTT is designed specifically for drifting applications. It utilizes a global

positioning system (GPS) location, which is transmitted regularly to the Argos satellites and then

relayed to the CLS data center. Once there, the data is made available through a web-based portal

allowing the data to be mapped and plotted [3].

Like the approach above, one research team constructed a tracking device using a plastic

bottle with several sensors inside that transmitted location. Their study used empirical data to

link inland freshwater inputs into marine systems. These "bottle tags" were released in the Ganges River, which runs through India, and worked their way through the river system and into the Bay of Bengal marine system. The total distance tracked was 2845 km over 94 days [26]. In other studies, oceanographic modeling and current drifter data have been utilized in predicting the movement and accumulation of plastic pollution from localized coastal areas to a large oceanic scale [27-30]. As seen from these studies, one of the best ways to track plastic is to create something that can model the plastic pollutions characteristics. By employing this method, it shows the path the plastic travels along and where it ends up. Though these methods provide adequate results, they can be unpredictable due to surface winds, currents, and other adverse scenarios.

2.2.2   Acquiring Methods

Once plastic pollution is found, the question becomes how it can be removed from the environment. Typical methods include simply using human resources and crews to clean up the shoreline and nearby areas. However, this approach is not as practical cleaning up larger patches of trash collected in the middle of the ocean, such as the Great Pacific garbage patch. If conventional methods were used, it might take thousands of years and tens of billions of dollars to complete. One company has proposed a quicker and much cheaper solution. It utilizes a passive design targeted at using wind, waves, and currents to navigate the patches. However, to successfully capture the plastic, the capture system must move slower than the plastic. To accomplish this, a sea anchor is attached to slow the system down enough so that the plastic starts to accumulate in one centralized location. The anchor acts very similar to how a drogue chute helps add slight resistance to a parachute to ensure correct deployment.
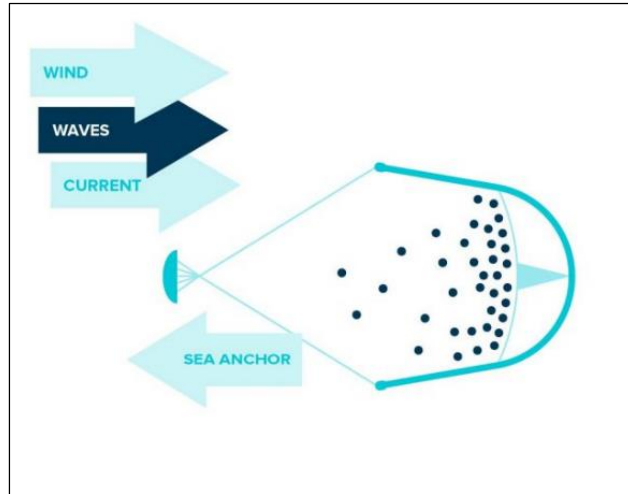
FIGURE 2-2: Simplistic approach to removing plastic pollution (OCEANCLEANUP, 2020)

FIGURE 2-2 shows the methodology behind the OCEANCLEANUP team's approach. It creates an artificial coastline for the plastic to accumulate on by deploying a chain of floaters that sit on the surface of the water. Attached to these floaters is a skirt that hangs beneath, allowing no plastic to escape underneath.

2.2.3   River Collecting Methods

The OCEANCLEANUP teams' passive design that removes pollution from the marine environment offers a vailed solution for ocean plastic pollution; however, it does not attack the problem where it originates. For this, the OCEANCLEANUP team is taking a different approach. The idea implements a USV, "the interceptor," which uses a conveyer system to extract plastic pollution gathered along a deployed barricade. This design can gather up to 50,000 kg per day, continuous operation while entirely solar-powered, making the design energy neutral. However, this system still requires trash to be post-processed and separated from trash and recyclables, as well as being extremely large (8 m x 24 m x 5 m) and ineffective in smaller waterway systems.

Another method that has been recently introduced in the waterways of Amsterdam is known as "The Bubble Barrier" [1]. This system implements a perforated tube laid across the bottom of the canal where compressed air is pushed through it. As this compressed air moves through the tube, it creates a screen of bubbles that catch floating debris. As the plastic is pushed to the top, the current carries it to a catchment pool, where it is then collected for analysis. Similar to the first method is Baltimore's own "Mr. Trash Wheel." This system uses the same technology as the OCEANCLEANUP team's "interceptor; however, it implements a waterwheel for its primary source of power, using the river's current. On slower days, solar panels provide backup power to the conveyor, which extracts the debris from the river. This method has shown great success, extracting 907 tons of trash and pollution [31]. A different approach is New Naval's Tactical Recovery System Hellas, or TRASH. This is a floating boom located at the mouth of the Kifissos River in Athens, Greece. This system uses a mesh barrier to collect river plastic and channel it towards a centrally located floating cage. This cage then lifts the collected plastic up to the level of the harbor wall to be extracted. Each of these methods provides advantages and disadvantages. Some can collect more plastic pollution than others before stopping, and some can be implemented in smaller locations, while others require minimum maintenance. To tackle this problem, more than one solution is needed; this is where smaller USV can excel.

2.3   Defining USV

As seen by some of the previous applications, USVs can be very useful for retrieving trash. However, understanding what a USV is and how it works must come first; [32] defines a USV as an "unmanned vehicle which performs a task in a variety of cluttered environments without any human intervention, and essential exhibits highly nonlinear dynamics." USVs are

also called autonomous surface vehicles (ASVs) or autonomous surface crafts (ASCs). No matter what name they go by there job is the same, to work remotely and independently to accomplish a set task. However, many USVs are only semi-autonomous due to limited autonomy from the challenges in automated and reliable guidance, navigation, and control functions for all operating conditions that they may experience. However, the need for USVs continues to grow due to the need to minimize human control, human error, and cost while increasing the reliability and safety of an operation [33].

2.3.1   Different Marine Applications

As technology begins to expand with the use of USVs, so do the number of applications in which they can be used. As more compact, effective, and affordable navigation tools become available, there is an increased opportunity for USVs to be useful. They offer several benefits: (1) USVs can perform longer and more hazardous missions than manned vehicles without risking lives; (2) maintenance costs tend to be lower; (3) the low weight and compact dimensions of USVs give them enhanced maneuverability and deployment in shallow waters (rivers and coastal areas) [32]; (4) USVs also have greater potential payload capacities and can perform in deeper water. With these advantages, USVs are being developed for a wide range of applications, such as scientific research, environmental missions, ocean resource exploration, military, and many other applications.

2.3.2   Scientific Research

There are several areas where USVs can be used within the scientific community. One example includes a team of researchers that developed a USV using a low-cost kayak to provide housing for an array of sub-systems that allowed the tracking of large fish and marine animals previously tagged. This system included several sensors, batteries, a propulsion system, GPS for

navigational purposes, a prime mission sensor, and an acoustic transducer. This system also utilized three separate computers, one for mission controls, one for propulsion motor control, and the last one for sensor orientation. The goal of this project was to reduce the overall cost of gathering data on marine wildlife movements. This is just one specific case where a USV may offer advantages such as cost-effectiveness. Another team in Germany was tasked with developing an unmanned surface vehicle that could be deployed with high accuracy of positioning and track guidance and under shallow water conditions as a carrier of measuring devices. Such a device could have applications including death surveying, current profile measuring, sediment research, and sample extraction for drinking water areas [34]. The same team also envisioned a rescue vehicle that could be deployed automatically in a "man overboard" incident. Other examples of scientific research include the utilization of USVs to test different hull designs, communication and sensor equipment, propulsion systems, and a variety of control schemes [35].

2.3.3   Environmental Missions

Similar to scientific research, many environmental missions have been carried out using USV technology. This can be anything from environmental monitoring to disaster relief. One research team used a sea surface autonomous modular unit (SESAMO) to study interactions between sea and air. As seen from past experiences, understanding the interaction between the hydrosphere and atmosphere could help predict global-scale climatic circumstances [36]. This USV was purposefully designed to analyze the water's very top surface, known as the microlayer. In this layer, several different things can be analyzed. For example, the water can be tested for surface pollution, including pesticides, poly-cycled hydrocarbons, oil remains, the structural composition of the water, as well a unique community of life-forms named neuston. To

13

accomplish this complicated task, the USV was equipped with a compass, pumps and valves, anemometer, wireless LAN antenna, GPS antenna, thermometer, and microlayer sampler. The onboard computing system included a single-board computers board and three PC 104 modules supporting digital input/output and analog input/output. As tasks become more complicated, so do the tools and communication to make everything function appropriately.

Another excellent example of utilizing USVs is the development of the small water plane area twin-hull (SWATH) vehicle for bathymetric mapping of underwater features [37]. The purpose of using a SWATH design is that it allows for a platform with excellent wave disturbance rejection and natural stability in pitch and roll compared to the standard boat hull. This is accomplished by reducing the amount of hull located directly at the waterline where waves could interject, creating unequal forces on either side of the hull. To perform the bathymetric scanning, an Imagenix 837 "Delta" multibeam imaging sonar was used. This system was capable of 20 pings per second and a depth range of 100 m. The sonar system is then linked to a Trimble GPS unit which matches the images produced with coordinates. As far as the navigation and controls go for this design, several methods were implemented. These included a human-piloted mode, a heading control mode, a waypoint control mode, and a path following mode. Again, this shows the diversity in which USVs can be implemented. Other environmental mission examples include disaster-aided prediction and management as well as emergency response [38].

2.3.4   Ocean Resource Exploration

Following the trend of ocean/water applications, ocean resource explorations are another excellent example of where USVs can be used. This can be everything from oil, gas, and mine exploration [39, 40] to the construction and maintenance of offshore platforms/pipelines [41]. In

the example presented in [39], an ASV was created to autonomously locate and stay locked on a

target to allow a human operator back on the shore to make appropriate classifications of the

object. Though this does not provide full autonomy, the system of locating and acquisition

methods do. This scenario perfectly shows how a USV can be implemented to reduce danger to

human operators. This would require an individual to dive down and visually inspect each object,

whereas by using the USV, the operator never has to leave the safety of the USV deployment

location.

2.3.5 Military

USVs have been utilized for several decades within the US and other countries'

militaries. Offering some of the latest technologies, USVs utilized within the military stayed top

secret for many years before becoming public. Some of the known uses for USVs include coastal

surveillance and reconnaissance [39, 42, 43]), search and rescue missions [38], anti-terrorism/

force protection [33], remote weapons platform [40], and target drone boats [34]. Each of these

USV applications serves a strict purpose and is retrofitted to accomplish each task with a high

accuracy percentage. In the example given by [43], the proposed design required the USV to

utilize reactive planning complemented by short-term forward planning to generate specific

maneuvers for blocking enemy vessels approaching. This system requires quick comprehension

of the surroundings to allow for an adequate reaction to the evolving situation. As previously

mentioned, the utilization of these USVs, especially in military applications, allows for the

operator to either be removed entirely from the situation or to be located in a safer location than

if that individual had to complete the given task without the use of a USV.

2.3.6   Other Applications

USV can be used in many other applications, including transportation [44], mobile communication relays [45], boat hull inspections, and several others. Similar to earlier examples, these applications require precise and advanced sensor technology to complete their given task. However, a common theme is their emphasis on the USVs navigation, guidance, and control system. Due to the diversity of scenarios a USV may experience, full autonomy without any human interventions has remained a common barrier. This becomes particularly true with larger and more complex situations such as the previous applications discussed. However, looking back at the definition of a USV, all of these applications express highly nonlinear dynamics.

2.4   USV Subsystems

As seen previously, USVs can be implemented into numerous applications, each having its own design requirements. This is similar to the saying about having the "right tool for the job." A USV used for bathymetric mapping of underwater features has different sensors and systems than a USV designed for search and rescue missions. To accomplish a complex task, there are several key systems that a USV must encompass. These subsystems include the frame, visual recognition system, navigation, and guidance system, independent task system (specific to each USV based on the given goal), control system, propulsion system, and communication system. Each of these systems must work collectively for the USV to be able to perform its given task.

2.4.1   Frame Design

Wang et al. (2016) demonstrate a SWATH design USV that exhibits excellent seakeeping performance while reducing overall resistance from the water. Typical frame design experiences increased fluid resistance as velocity increases. However, this design improves this situation by

reducing the depth of draft at high speeds so that part of the volume of the hulls is located on the surface of the water rather than beneath. This is accomplished by using hulls that are planning shaped, providing lift force for the USV as the speed increases [46]. Brizzolara et al. (2011) looked at several SWATH designs using an advanced computational fluid dynamic (CFD) flow solver and a differential evolution global minimization algorithm to ensure design optimization. This process allowed the team to do comparative analysis between drop-shaped body SWATH design and what they found to be the optimal SWAT hull design. This design reduced the overall resistance from waves by utilizing the positive interference between the wave trains generated by the components of each hull, resulting in a cancelation effect [47].

Zaghi (2016) utilizes a SWATH design to monitor protected coastal regions without using any fossil fuel pollutants. This design was chosen over other hull designs to increase stability while reducing overall resistance to lower energy consumptions. The SWATH design minimizes hull cross-section area at the surfaces, in turn increasing the vessel's stability. Reducing the cross-sectional area of the hull located at the surface reduces the area in which wave energy can impact the USV. This directly correlates with the stability and energy use of the USV[48, 49]. Lin and Yang (2018) utilized a high-fidelity CFD solver based on Reynolds Average Navier-Stokes equation to predict and model accurate flow predictions for SWATH-based design. These simulations were then tested using a 2.7 m USV test model to validate the simulation results. The optimization results showed the advantages of SWAT hull design to have lower resistance in marine environments. The team's design reduced the overall resistance force experienced by the hull by approximately 100 newtons at max speeds [50]. Each of these studies showed the advantages of a twin-hull SWATH design. This design exhibits optimal stabilization and a reduction in resistance forces resulting in lower overall energy consumption.

2.4.2   Visual Recognition Systems

The key component of this project is being able to identify macro-sized plastic pollution that is located on the surface of the ocean. By utilizing a visual recognition system, the USV can locate and identify debris located along the water's surface. Vision involves the physical elements of illumination, geometry, reflectivity image formation, and the intelligence aspects of recognition and understanding [51]. With the technology available today, there are several ways to accomplish this, with the end goal of developing an array of sophisticated sensors that provide a high degree of accuracy in visual recognition than current systems utilized today. Sensors being utilized today for similar processes include ultrasonic sensors, LIDAR sensors, thermal sensors, spectroscopic sensors, spectroradiometers, and many other remote sensing elements. These sensors allow for images of these objects to be captured; however, they do not analyze or process any of the images captured. The processing and analysis are completed by software packages run by the onboard central processing unit (CPU).

2.4.3   Case Studies

Advancement in this area has developed over the past two decades as sensors and computer processors have improved. One team from the University of Hamburg utilized muti-sensor fusion to create a perception system that could be used for object recognition [52]. The perception system combines a three-dimensional (3D) laser range finder and a camera. A calibration process is also used to define the extrinsic parameters and calculate the transformation between the laser range finder and the camera. The resulting transform allows an exact position and color to be assigned to an exact point resulting in an unorganized point cloud. This data is then visualized using OpenGL, a cross-platform application programming interface for rendering two-dimensional and three-dimensional vector graphics. However, this method

required the analysis to be post-processed before the point cloud could produce a reconstructed figure. Automating this process would dramatically help the end-user and reduce the overall time needed in reconstructing the original figure.

Ecemis and Gaudiano (1991) from the Boston University Neurobotics Laboratory created a system for object recognition using ultrasonic sensors. This recognition system consisted of a polaroid sonar coupled with an A/D data acquisition board in a LINUX-based PC. It then uses an ARTMAP neural network classification system to recognize objects at varying distances. ARTMAP is a neural network architecture that autonomously learns to classify arbitrarily many, arbitrarily ordered vectors into recognition categories based on predictive success [53]. However, before ARTMAP could be utilized, the echo data was first transformed into its respective power spectral density (PSD) frequency using MATLAB or its respective envelope in the time domain. The PSD method showed a slightly larger error in object recognition than the envelope method, especially at closer distances. When the object was at a distance of four to five feet, the average accuracy for the envelope and PSD method was approximately 97% and 85%, respectively [54].

2.4.4   Navigation System and Guidance System

Once the USV is able to recognize plastic pollution, it must then be able to navigate to a location allowing for the extraction of the debris from the environment. This required implementing two main systems, a navigation (or guidance) system and an avoidance system. Each of these systems is instrumental in ensuring the overall functionality of the USV. The guidance subsystem ensures the ability of the USV to be able to navigate its way through different waterways based on navigation and locational algorithms. This system can comprise several different features such as GPS, radar, acceleration sensors, wind sensors, and current sensors. The avoidance system ensures that the USV avoids obstacles that may impede the

intended mission, such as wake buoys, shorelines, docks, and other boats. This system can utilize technologies such as LIDAR, 3D vision, and ultrasonic sensing to detect these objects before the USV reaches them.

Several different navigational algorithms have been implemented in the past to accomplish USV navigation and avoidance. These include path planning, fuzzy LQG- and GA-based MPC, PD controller linear quadratic, PID -EKF, waypoint following, trajectory planning, priority task approach, Kalman filter algorithms, and potential fields. Considering that each algorithm is implemented on different USVs, each has its advantages and disadvantages. These algorithms utilize their own correct and effective parameters to allow for faultless navigation and obstacle avoidance.

2.4.5 Locational Algorithms and Kalman Filters

Praczyk (2014) presented an anti-collision system based on an evolutionary neural network. This system was built using two neuro-evolutionary techniques, Assembler Encoding with Evolvable Operations (AEEO) and Cooperative Co-Evolutionary Neural Networks (CCENN). AEEO evolved from Assembler Encoding (AE), where an artificial neural network [30] is represented in the form of a linear program consisting of different operations with predefined implementations and data. This data is then used to create a Network Definition Matrix, which defines a single ANN. For AEEO, the final NDM comprises two smaller matrices, topology (binary values) and the parameters of the network. For CCENN, an ANN is composed of a set of unconnected sub-ANNs and a vector of numbered output registers. By combining these two methods, an adaptive collision avoidance method is obtained for a rapidly changing environment that cannot be predetermined [55].

Zereik (2015) addressed three control tasks: path following, obstacle avoidance, and speed regulation. Each of these control tasks was captured by the overall algorithm "Priority Task Approach." The main objective of this algorithm was to correctly execute a path-following task while ensuring obstacle avoidance and speed regulation of the USV. This method allows for several tasks to be defined and given a priority value based on the level of importance. However, this value is fluid and can be altered based on the different conditions the USV may encounter. This allows the USV to prioritize the path following control when in safe environments. However, this priority can be inverted as soon as obstacles are encountered. This ensures that obstacle avoidance control has the highest priority. Once the obstacle is no longer a threat, the path following control regains the highest value [56].

Motwani (2013) introduces the use of an Interval Kalman Filter (IKF) algorithm that can estimate the heading angle of a vessel under erroneous modeling assumptions [57]. The use of a Kalman Filter (KF) can be found in numerous applications. This type of filter allows the user to combine measurements from various sensors, weighing their respective precisions. This tool has been used for combining data from low-cost sensors to obtain greater reliable estimates that otherwise would require more precise sensors. In the case of Motwani, the IKF was used to estimate heading angle based on data gathered from differential thrust data, true heading, and compass measurements that were captured. It took the upper range of this data and the lower range and took the universal average of these to estimate the heading angle of the USV. This method has also been used to integrate GPS localization data, inertial measurement units (IMUs), and magnetic compass sensor readings to assist in the navigation of USVs. This can be seen in [58], where a group of researchers from Dalhousie University used an Unscented Kalman Filter (UKF) to combine data from the three sensors to give system state estimations with high

21

accuracy compared to Extended Kalman Filters (EKF). More information regarding these UKFs and EKFs can be found in Pierre and Gingras (2004) [59].

Onunka et al. (2013) integrated ultrasonic sensors and radar to help reduce the overall uncertainties present in the guidance and controls of the USV while also improving the obstacle detection and avoidance capacity in near field-regions of the USV. The autonomous control algorithm of the USV used data captured from the sonar. At the same time, this data also projected the distance for each ultrasonic sensor to the external frame of reference of the USV. This allowed the USV to reference its positions based on the objects present around it. The reduced the overall uncertainties present in the guidance and control system of the USV [60]. Each of these methods provides insight into navigational theories that have been implemented both past and present. These USV systems all utilize fast learning algorithms to allow for adverse conditions to be accounted for in every situation encountered.

CHAPTER 3: OVERVIEW AND SYSTEM DESIGN

To achieve the overall goal of this project, a prototype of the conceived USV concept was built and tested. The terminology used to describe key features of the USV are:

- *Extraction mechanism* – Scoop design that removes located debris from aquatic environments

- *Object discovery system* – Vision system utilized in object localization in reference to the USV platform

- *Verification system* – Camera and vision processing hardware that provides feedback to the extraction mechanism

- *Control base* – Central hub for all components allowing for system mobility and functionality

- *OLARP* – Object Localization Acquisition Robot Prototype

- *Floating debris* – Sample Pollution

The USV systems were categorized into five main subsystems: floating platform, object discovery system, maneuverability system, extraction system, and debris verification system. Each subsystem contains supporting hardware to complete the designated task. All of the subsystems are connected to create the vision-guided USV for debris removal from aquatic environments. The prototype for this experiment will be referred to as the object localization acquisition robot prototype (OLARP).

3.1   USV Overview

The USV subsystems are pictured in FIGURE 3-1, with all functional hardware connected. The control base for the USV was positioned at the stern. The drive motor provided

the USV forward motion and the ability to turn right or left. This motor was placed directly to

the rear of the control base. The placement of this motor allowed for increased maneuverability,

commonly found in similar catamaran-style boats. The control base housed the majority of the

USV weight. This weight was comprised mainly of the three 12V DC batteries. The weight

distribution was across the control base platform, ensuring that the center of gravity was between

the two hulls of the USV. Another key part of the control base was the image processor. The

image processor performed all vision-based algorithms and filtering. Also seen in FIGURE 3-1,

the object discovery camera was mounted at the bow of the USV. Located behind the discovery

system was the extraction mechanism and the dump area for extracted debris. Located directly

over the extraction mechanism was the verification system.
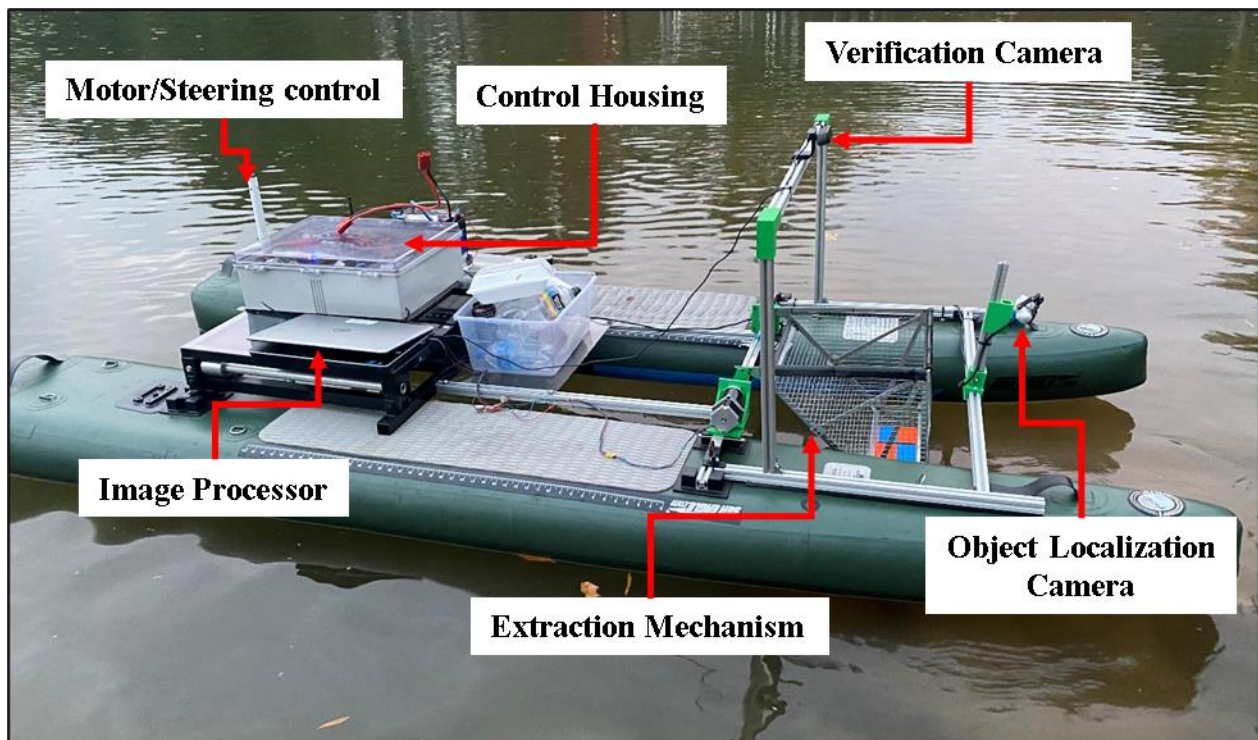
FIGURE 3-1: Final USV design

A layout of the control base is presented in FIGURE 3-2. The rear platform was used to

house the control base. This provided a solid platform to keep all components away from the

aquatic environment. All components that were not waterproof were stored within the NEMA box. These included the USV controller, buck converter, motor controller, voltage regulated module (VRM), and stepper driver. The laptop was located outside the NEMA box to allow quick and easy access to monitor the image processing algorithms in real-time. The GPS unit and the servo were also located on the outside as both are waterproof rated. The overall dimensions of this base were 2 ft by 3 ft and set approximately 1 ft above the water's surface.
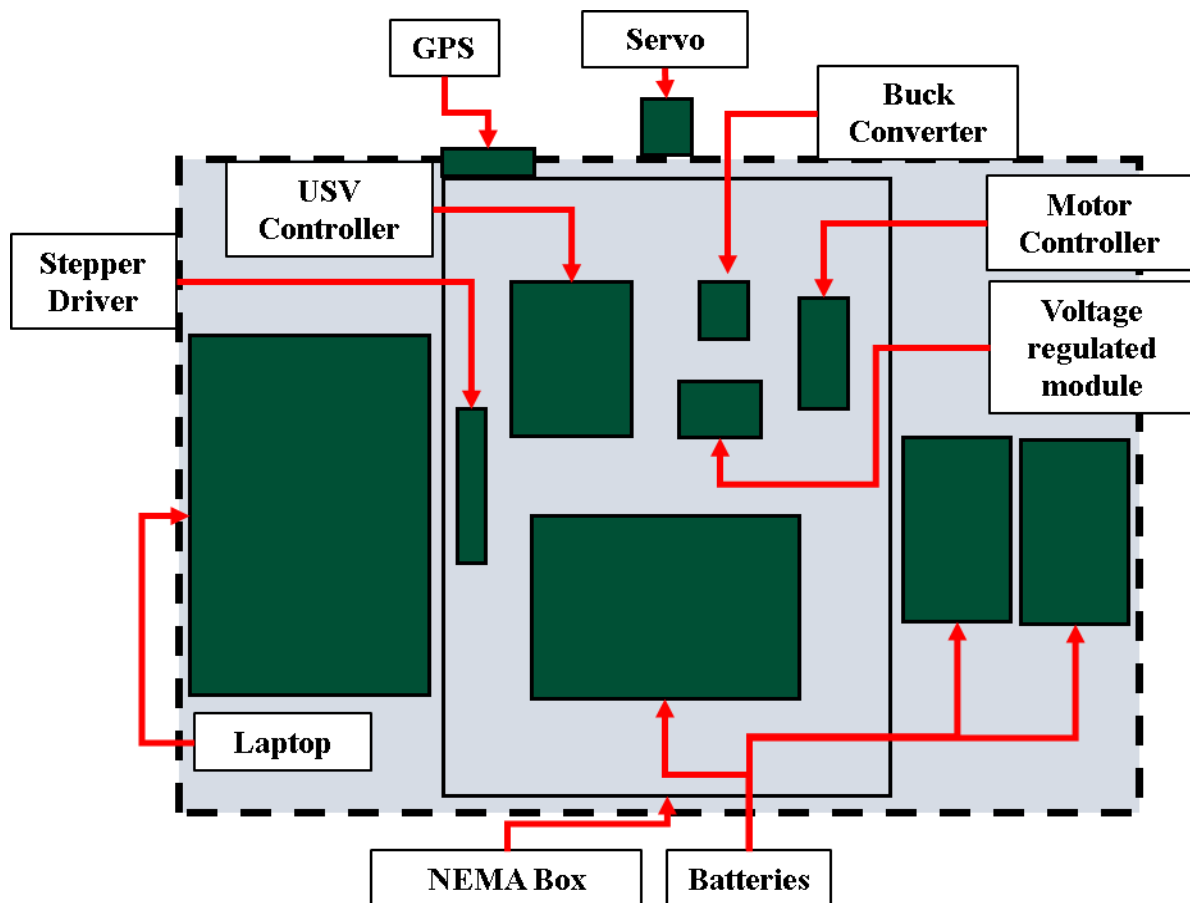
FIGURE 3-2: Control Housing

3.2   USV Frame

The frame of the USV was critical to ensure the overall success of a mission. This was where all the control systems were located as well as any sensors used for data collection. There are several different types of frame design, such as twin hull, catamaran, single-hull, pontoon, swath,

and sailboat design. Each of these designs has advantages and disadvantages; however, the chosen hull design's primary advantages over the other designs were storage capacity and overall size. The platform used for the research of this project was a SEA EAGLE SUPCat 10, as shown in FIGURE 3-3.The frame utilized a twin-hull design measuring 12ft x 4ft x 3ft (L x W x H). One advantage of this design included reducing the overall drag resistance from the water while also being lightweight and agile compared to a single hull USV. Another advantage specific to this research prototype was that it allowed the extraction system to be located directly between the two hulls.
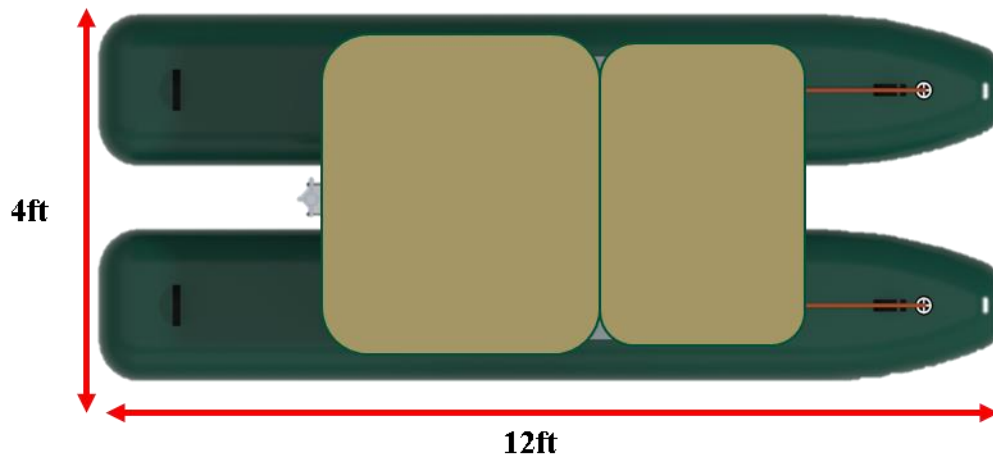
FIGURE 3-3: SEA EAGLE SUPCat 10 USV frame with dimensions

3.3   Object Discovery System

The object discovery system implemented an Intel RealSense D455 depth camera (RSDC). The RSDC utilizes three imagers, a right-imager, a left-imager, and a Red Green Blue (RGB) imager to capture both RGB images and depth images. The RSDC provided a field of view (FOV) of 90° by 65° and 87° by 58° for the RGB and depth images, respectively. The stereo vision implementation consists of a left imager, right-imager, and an optional infrared projector. The data captured by the RSDC is sent to the onboard Intel RealSense Vision D4

processing board to allow for depth values to be assigned to each individual pixel. This is done

using the two parallel imagers (right and left) to capture images and then calculates the depth by

estimating discrepancies between matching key points in the two images. *FIGURE 3-4* shows

how disparities were found to calculate depth images. Though this was a key feature of the

RSDC, it was found not beneficial in the overall design.
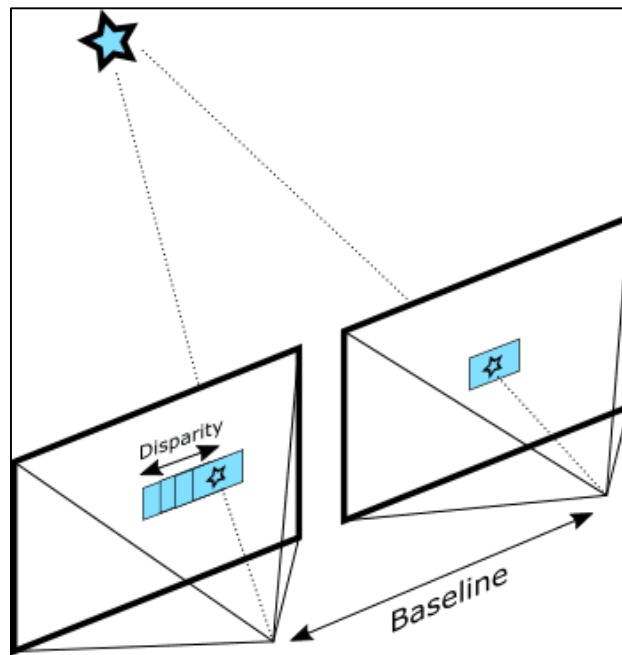
FIGURE 3-4: Utilizing disparity to calculate depth [61]

Additionally, a polarized lens was added to the RSDC RGB imager to filter out excess

glare captured by the camera's lens. This helped reduce excessive noise from surface reflection

seen during image processing by filtering out horizontal light glare coming from the water's

surface.

Two separate brackets were 3D printed using additive manufacturing (AM) techniques to

allow mounting and correct angle alignment. The RSDC was mounted 1.5 ft above the water's

surface. It was also fixed at a downward angle of 36 degrees from horizontal. This was selected

due to the vertical FOV of the camera being 65 degrees. At this position, the RSDC captured

objects up to 24 ft away due to the mounting angle. The angle was selected to reduce excess

noise that may be captured within the image and the particle size of the sample debris being used

in this research.   shows the mounting brackets and the angle setup used for the RSDC.
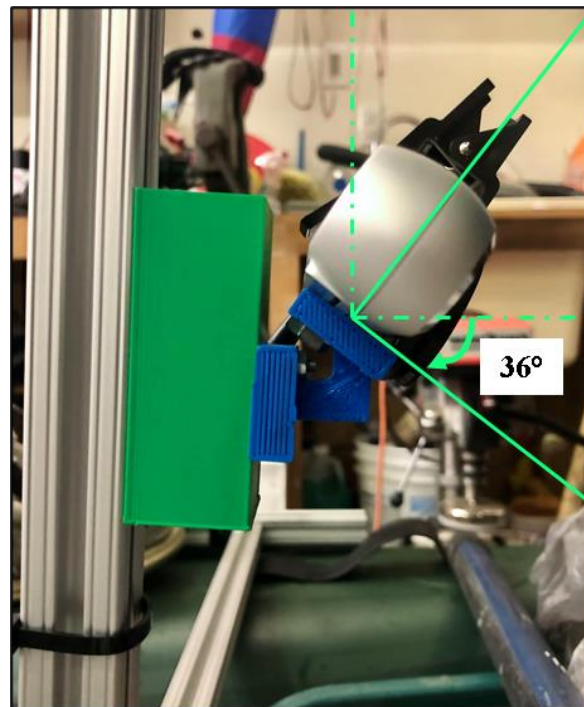
FIGURE 3-5: 3D brackets and setup angle of RSDC

Once the images were captured, they were relayed to the laptop processing unit to be

processed. National Instruments (NI) LabVIEW scripts were used to filter out the noise and

excessive background information, and this required the use of several key LabVIEW virtual

instruments (VI). The captured images included one 32-bit RGB image and one flattened

pixmap. The image formats were converted to greyscale images and then to binary images to

remove unwanted information. Once the excessive information was extracted, the remaining

information was used to calculate the object's centroid location relative to the RSDC location on

the OLARP. The coordinate data was transferred to the myRIO via wireless communication. The

myRIO used the extracted values to adjust input signals to control the motor speed and direction

of the USV to maneuver towards the detected object.

3.4 Maneuverability System

The maneuverability system comprised three components, a TRAXXAS 400 servo

motor, trolling motor, and a talon SRX motor controller. Each of these components received

signals from the myRIO which allowed for a full range of motion control for the servo motor and

speed and direction control of the trolling motor. The TRAXXAS 400 servo motor offered a

fully waterproof design and provided 2.1 ft-lbs of torque. The servo was mounted directly to the

trolling motor mount utilizing a four-bar linkage system to allow for heading adjustment. The

USV speed adjustment was accomplished using varying voltages sent from the motor controller.

FIGURE 3-6: Servo connection to trolling motor

3.5   Extraction System

The extraction system was comprised of two main components, the extraction

mechanism, and the driving system. FIGURE 3-7 presents the extraction system used to remove

floating debris from the environment. The extraction mechanism was constructed using an

aluminum frame with a mesh on the back and sides. The overall size of the scoop was 17 in x 15

in x10 in (length by width by depth). The outer dimensions of the scoop were determined

through testing of the sample pollution at various floating depths. Driving the extraction

mechanism was a NEMA23 stepper motor with an integrated planetary gearbox with a 77:1

gearing ratio. Due to the additional gearing, the shaft's maximum output and holding torques

were 69.4 ft-lbs and 17.3 ft-lbs, respectively. This allowed for adequate torque to be supplied to

the extraction mechanism during all phases of the deployment.
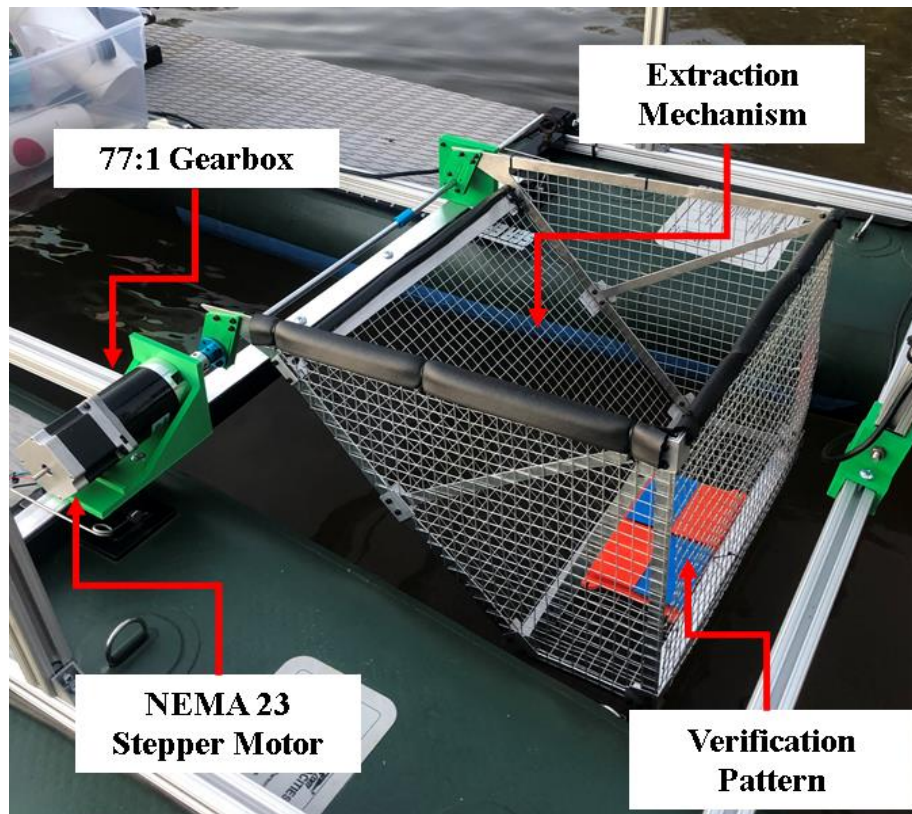
FIGURE 3-7: Extraction System used on the OLARP

During the testing of the OLARP, the extraction mechanism had four set positions that it was instructed to reach: standby, deployed, authenticate, and dispose. FIGURE 3-8 shows each of the extraction mechanism states. During the standby position, the extraction mechanism was set parallel with the water. Once an object was detected, the extraction mechanism would be lowered 90 degrees into the deployed state. This allowed the scoop to be partially submerged, ensuring complete capture of the floating debris. Following this, the extraction mechanism would rotate counterclockwise to the authentication position. The last position was disposal, where the extraction mechanism would rotate a final 90 degrees counterclockwise to deposit the debris.
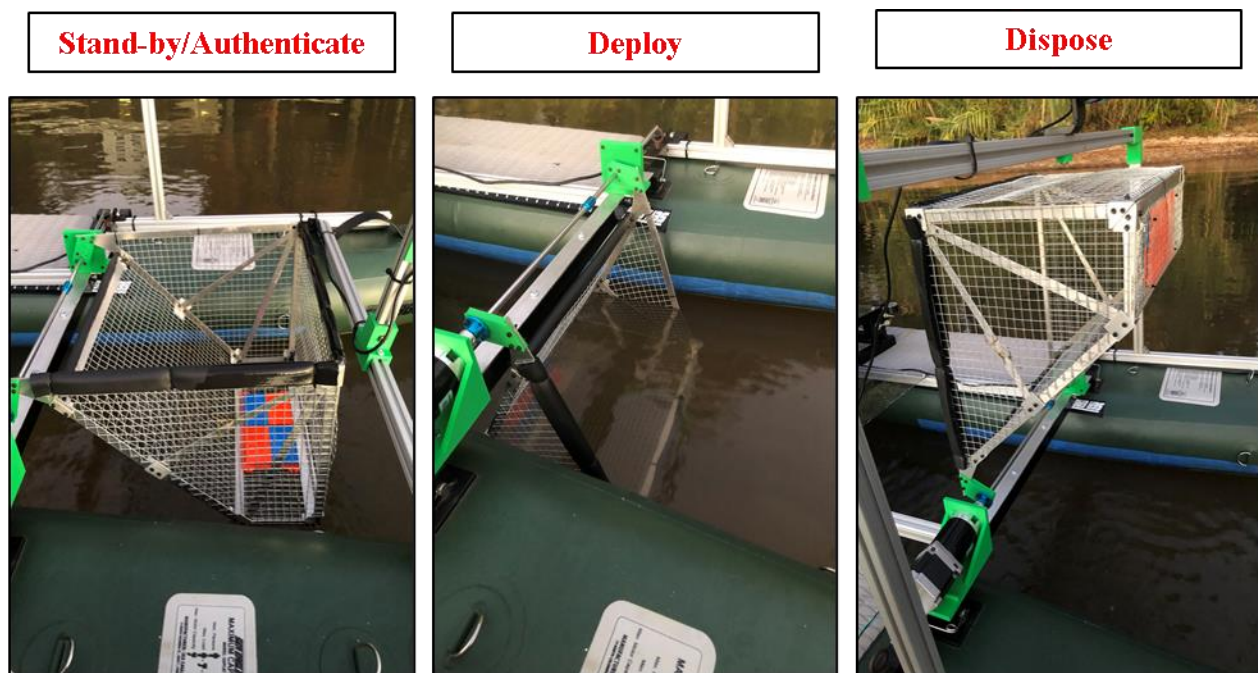
FIGURE 3-8: Each position of the extraction mechanism

3.6   Debris Verification System

To determine whether the detected floating debris was extracted from the environment, a verification system was implemented. This system used a j5create USB webcam to capture images that would be processed on the laptop. The j5create has a FOV of 80 degrees allowing for adequate capture of the extraction mechanism when in the authentication position. The camera

was positioned 21 inches above the extraction mechanism. This height was chosen to provide

sufficient clearance as the extraction mechanism traveled to the disposal position. The height

also ensured that the extraction mechanism was well within the FOV of the camera.

FIGURE 3-9 presents the pattern used during the verification process. The pattern was

implemented as a template against which an acquired image could be compared to determine the

presence of the debris. The pattern was composed of two blue squares and two orange squares

arranged in a checkered pattern. These colors were selected based on testing to reduce false

positives. During the setup, the pattern was saved on the laptop to use for comparison during

USV operations. When the extraction mechanism reached the authentication position, an image

was captured and processed using LabVIEW suite of express VI's. This was compared to the

pre-existing template for discrepancies. Based on this comparison, the myRIO would send

signals to continue to the disposal position or return to a deployed state.

FIGURE 3-9: Greyscale pattern used for verification process

3.7 Control System Breakdown

The control system of the USV was divided into two processing units, as previously discussed. FIGURE 3-10 shows an overview of each component used in the control system and their respective communication type. The first processing unit that was chosen was the NI myRIO-1900. The myRIO provides all controls for USV maneuverability as well as actuating the extraction mechanism. A myRIO is an embedded device that provides 62 expansion port connectors to allow analog input, analog output, as well as digital input and output (DIO) signals. The myRIO also provides regulated +3.3 V, +5 V, and ±15 V sources. Connected with the myRIO was a suite of supporting hardware that allowed complete and accurate control of the OLARP. The Talon SRX motor controller enabled speed and direction control using pulse width modulation (PWM) signals. The STEPPERONLINE stepper motor driver allowed interfacing between the myRIO and the NEMA23 stepper motor. The myRIO controlled the speed and direction of the stepper motor utilizing PWM signals and digital high/low signals, respectively. The TRAXXAS 2255 was controlled using PWM signaling to provide steering capabilities to the OLARP. Lastly, the GPS provided the longitude, latitude, and ground speed of the USV via USB. All non-waterproof components were housed within an NBF-32238 NEMA box. This housing was chosen to provide water resistance to hardware that was not ingress protection rated.

The second processing unit of the control system was the laptop, to which the two cameras were connected. The first camera was utilized to capture debris location and the second to verify that the debris was extracted. The RSDC, which was used to detect an object's location, makes use of USB 3.0 for high-speed data transfer between the camera and the onboard laptop. The verification camera utilized USB 2.0 for relaying data to the onboard laptop. The laptop

used wireless communication to transfer critical data captured from the images to the myRIO

Controller. A network was set up on the myRIO to allow for this relay of data.

FIGURE 3-10: Control diagram

3.7.1   User Interface Overview

Due to the test environment, a remote-control interface was required since direct control was not possible. This was accomplished using a Samsung tablet loaded the NI data dashboard application and connected to the myRIO network via Wi-Fi. The NI data dashboard application allowed simple indicators and controls to be used during testing. The two indicator types used were numerical and boolean. The numerical indicators are boxes containing corresponding values. The boolean indicators can be seen as circles and light up blue when the value is TRUE. FIGURE 3-11 displays the USV control dashboard. The dashboard contained two controls, *Initiate State Machine* and *Data logging*. *Initiate State Machine* started the USV operations. *Data logging* allowed critical values to be written to a file during operation. These values included: *Center of Mass X(ft), Center of Mass Y(ft), Angle (Degrees), Ground Speed, Motor Command, Rudder Command, Detection Variable, Trash location (Lat), and Trash Location (long).* Chapter four describes the variables in further detail. Indicators were also used on the control interface to allow for specific data to be displayed.
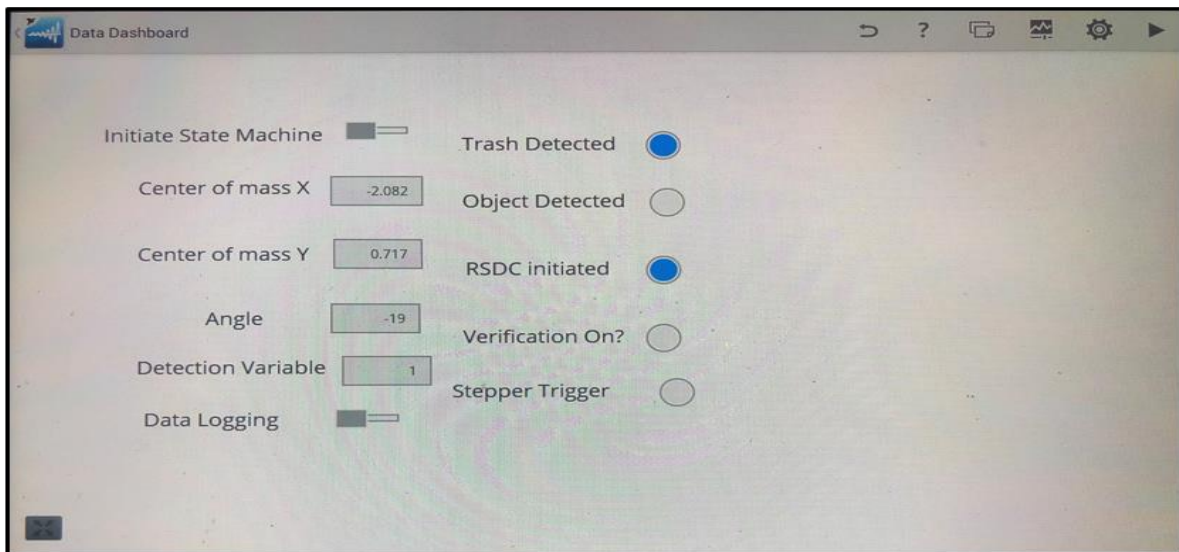
FIGURE 3-11: User control interface

3.8   Power Distribution

Power distribution is critical for any robotic system, ensuring functionality and controllability. FIGURE 3-12 shows the power distribution for the OLARP design. The USV was divided into three main power distribution sections: controls, extraction, and image processing. The control section was powered using one 12 V 18.1 Ah Absorbent Glass Mat (AGM) battery. The 12 V AGM battery was directly wired to the motor controller to provide 12 V. Also powered by the 12 V AGM battery was the CTR electronics VRM. The VRM supplied a regulated 12 V/ 2 A peak to the DROK buck converter, which steps down the regulated 12 V to a rated voltage of 7.5 V for the TRAXXAS 2255 servo motor. The VRM also supplied a regulated 12 V/ 0.5 A to the myRIO. The myRIO then provided power to the GlobalSat GPS receiver through USB. The extraction power distribution included two 12 V 18.1 Ah AGM batteries wired in series to provide 24 V to the stepper motor driver and then to the stepper motor. The image processing power distribution included both the discovery camera and the verification camera. The discovery camera is powered via USB at 5 V/ 700 mA, and the verification camera was powered via USB at 5V/ 160 mA.
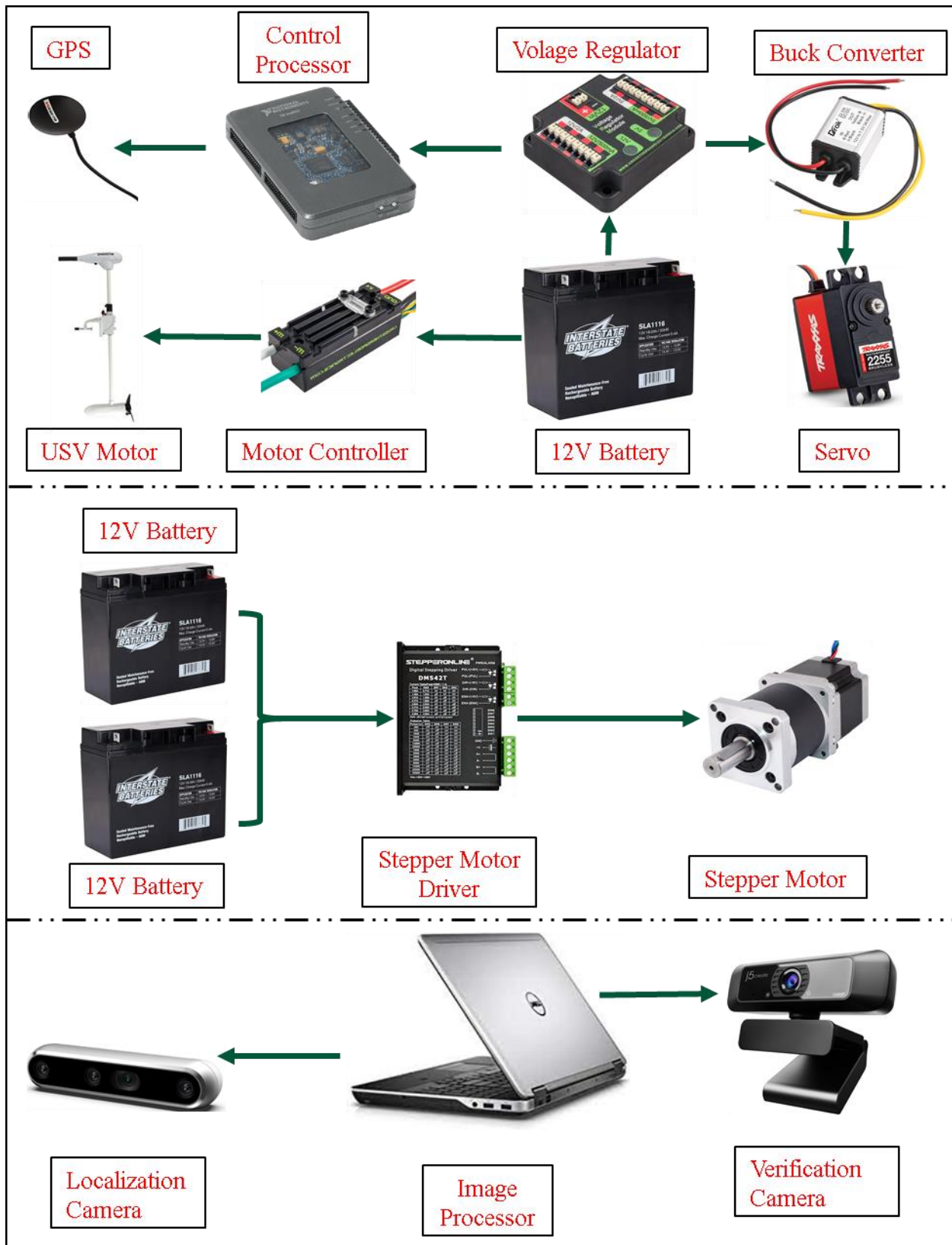
FIGURE 3-12: Power distribution on the USV

CHAPTER 4: SYSTEM AUTONOMY AND METHODOLOGY

4.1   Overall USV Autonomy

As discussed in the introduction, the main goal of this design was implementing the ability to operate without human assistance. To complete this, several key aspects of the design had to be automated. A flowchart of this automation overview is presented in FIGURE 4-1. The USV program was initiated after the USV was placed in the test environment. Once initiated, the program ensured the motor speed was disabled and that the prop was oriented in the correct position. Following this, the vision system, tasked with locating the floating debris, began acquiring images and locating any possible object within the RSDC's FOV. Once an object was located, commands were sent to the servo from the myRIO to re-orient the USV in the direction of the located debris. Subsequently, the extraction mechanism was positioned into the deployed state. After ten seconds had elapsed, the extraction mechanism was placed in the authentication position to allow for object verification. The deployment time of the extraction mechanism was determined from the known speed of the USV and the max distance in which an object could be located (24 ft). At this point, there was a feedback loop allowing a second iteration of the loop if the object was not detected within the extraction mechanism during the first iteration. During the second iteration, either a false positive was recorded, or the extraction mechanism continued to the disposal position. To complete the operation, the extraction mechanism disposed of the captured floating debris, if verified, into a catch bin located on the USV and returned to the standby state. For the USV design to be validated, floating debris was deposited within the FOV of the RSDC before the initiation of the OLARP. The OLARP was then deployed, and the task was considered completed upon extraction and verification of the floating debris.

To reduce the overall complexity of this system, the automation was separated into three main tasks with defined sub-tasks for specialized processes. All tasks were tested independently of each other. Once the testing of each component was completed, they were merged to create the overall operational program. Each of the automation tasks is as follows:

- *USV operation autonomy*
    - o Data acquisition
    - o Heading adjustment
- *Object discovery autonomy*
    - o Image acquisition
    - o Particle filter
    - o Centroid extraction
- *Extraction system autonomy*
    - o Deployment operation
    - o Verification system
    - o Dispose operation
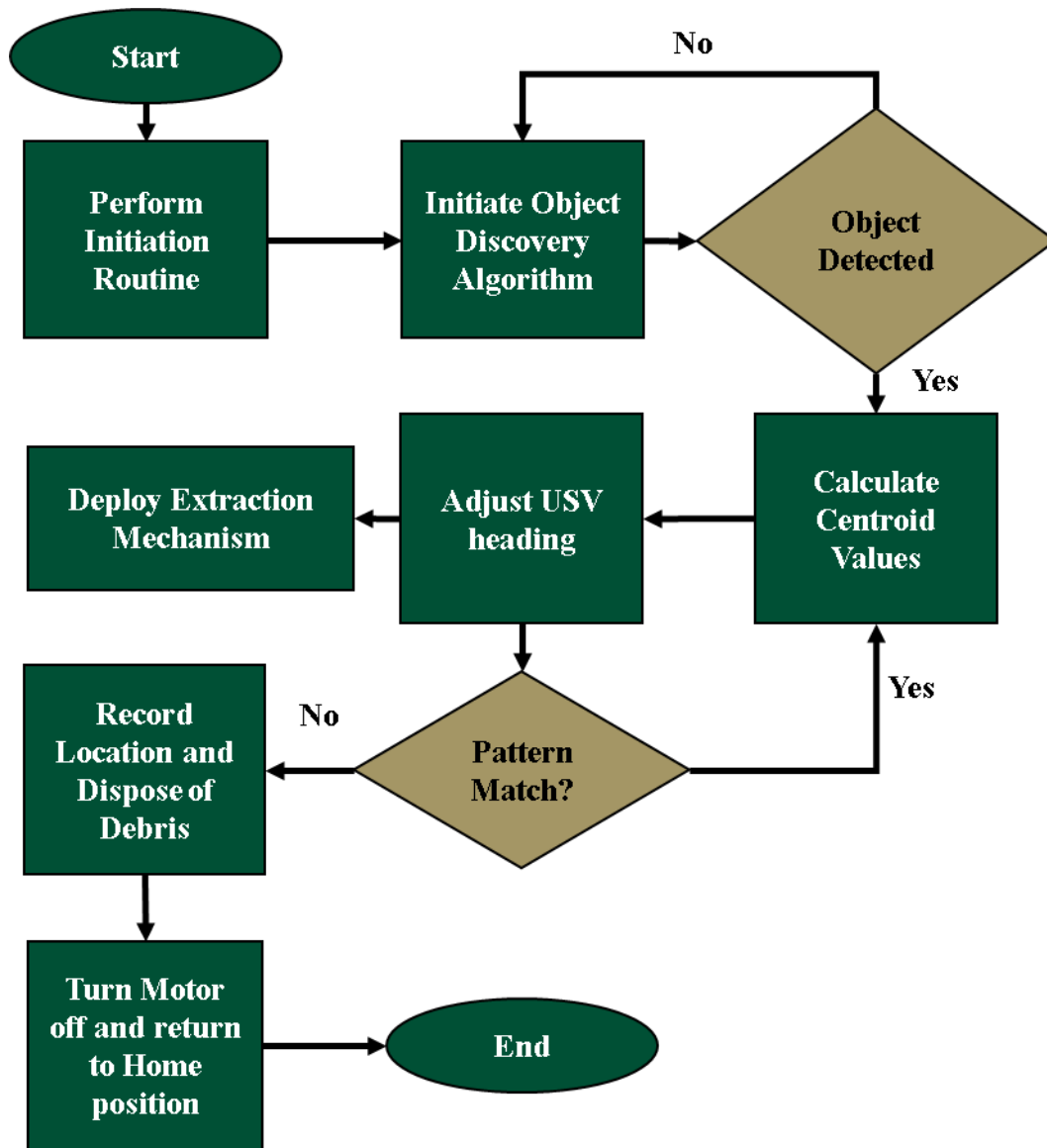
FIGURE 4-1: Automation overview

During the programming, a naming convention was created as follows:

- *Throttle* – a function that controls the velocity of the USV

- *Heading* – a function that adjusts the angle of attack of the motor

- *Centroid extraction* – a function to extract the centroid of an object within an image

- *Verification pattern matching* – a function to verify established pattern

To improve simplicity and allow critical data to be shared between VI across the established network, network-published shared variables were used. The two data types used for each shared variable were double-precision and boolean. Double types required 64-bit storage, providing 15-digit precision. Shared variables stored as double-precision types were used for numerical data that was either recorded or used to give future commands. Boolean data types were saved as either TRUE or FALSE. These were used to either trigger a specific program loop or act as an indicator to the user. Every shared variable used in this research is as listed:

- *Shared Variable Name* – Definition; **Data type**

- *Adjusted Angle (Left)* – Angle from the center of the USV to floating debris (adjusted for objects to the left of center); **Double**

- *Adjusted Angle [60]*– Angle from the center of the USV to floating debris (adjusted for objects to the right of center); **Double**

- *Angle (Degrees)*– Angle from the center of the USV to floating debris; **Double**

- *Begin Capturing* – Triggers the object discovery program to begin capturing and processing images; **Boolean**

- *Center of Mass X(ft)* – X coordinate of the center of mass of the located debris; **Double**

- *Center of Mass Y(ft)* – Y coordinate of the center of mass of the located debris; **Double**

- *Data Logging* – Triggers data logging program to write data to excel; **Boolean**

- *Detection Variable* – Returns either 0 or 1 if the debris was identified within the extraction mechanism; **Double**

- *End* – Ends the extraction system loop; **Boolean**

- *GPS Lat*– Records current GPS Latitude; **Double**

- *GPS Long*– Records current GPS Longitude; **Double**

- *Ground Speed*– Records the relative speed of the USV in ft/sec; **Double**

- *Motor Command*– Records the dc controlling motor speed; **Double**

- *Object Detected (Water)* – Returns TRUE if the RSDC detects an object; **Boolean**

- *Position Reached* – Designates when the extraction system reaches the authentication state; **Boolean**

- *Rudder Command*– Records the dc controlling servo motor/ motor orientation; **Double**

- *Start* – Triggers the state machine when TRUE; **Boolean**

- *Stepper Trigger*– Initiates extraction system; **Boolean**

- *Take Image (Verification)*– Triggers the verification camera to verify debris was captured; **Boolean**

- *Trash Detected* – Set to TRUE if debris was detected within the extraction mechanism; **Boolean**

- *Debris Location (Lat)* – Records the current GPS Latitude when trash detected is set to TRUE; **Double**

- *Debris Location (long)*– Records the current GPS Longitude when trash detected is set to TRUE; **Double**

4.2   State Machine Design

A "state machine" was used to ensure that certain aspects of the code were initiated in the correct order. State machines focus on three main concepts: state, event, and action. The first concept, state, refers to the program's status when approaching the problem. The event was triggered through input, and a known action was taken in response to this event. In this case, the action either repeated the current state or proceeded to a new state. For this research, a state machine with three separate states was used to ensure the correct sequencing of the algorithms.

FIGURE 4-2 illustrates the three states and what each state contains. The first state, *Start-Up* state, ensured that all the shared variables were set to their default values, the servo motor was in the home orientation, and the drive motor was disabled. The second state was known as the *Operation* state. During this state, all critical sub-programs were initiated. These included the object discovery VI, heading control, and extraction system deployment. Key sub-functions included within the sub-programs include centroid extraction, angle calculation, and the pattern matching algorithm. This state was maintained until the extraction mechanism reached the first authentication state of the extraction mechanism. The final state was considered the *End* state. During the *End* state, the motor thrust was switched off, and the motor orientation was set back to a neutral position. This marked the end of the USV operations.
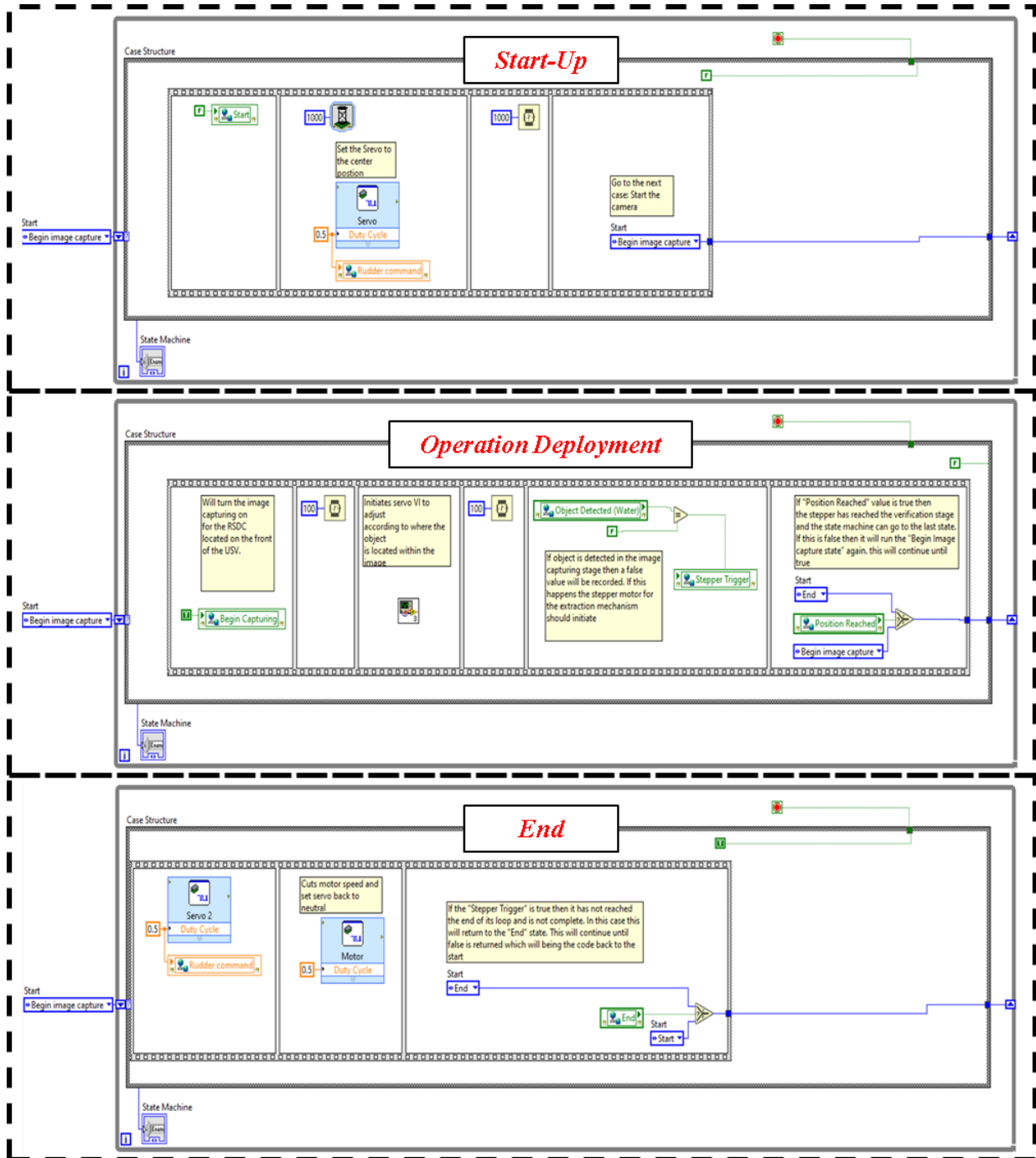
FIGURE 4-2: State machine including each state

4.3 Object Discovery Autonomy

The object discovery system provided crucial data, captured by the RSDC, to the myRIO, which directed the USV to maneuver towards floating debris. To accomplish faster autonomy, frames from the RSDC were processed via an onboard laptop. The required processing scripts

were written and uploaded to the laptop prior to deployment. LabVIEW software offered a suite

of express VI's that allowed fast and accurate processing of the captured images. FIGURE 4-3

shows the flow diagram of the object discovery algorithm. Once the RSDC was triggered, it

captured an image at a rate of two frames per second. This allowed adequate time for the data to

be transferred from the laptop to the myRIO and then to an output signal to the servo motor.

Once an image was captured, a calibrated template was overlaid on the captured image to allow

for real-world units to be computed. Following this, several image filtering VIs were used to

extract as much miscellaneous information as possible. The remaining information within the

image was assumed to be floating debris. The centroid of the remaining object(s) was calculated,

and the X and Y coordinates were reported in real-world units. These values were converted into

an angle at which the floating debris was to the center of the USV. These values were published

as a shared variable to the myRIO. These values were later extracted as an output for the servo.
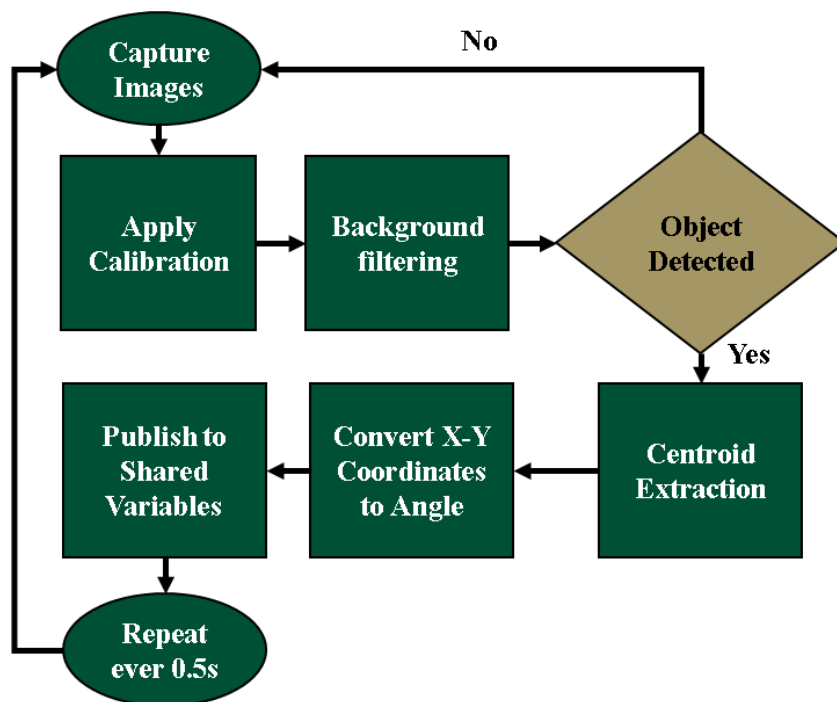
FIGURE 4-3: Image Processing flowchart for the object discovery algorithm

The overall image processing transitioned the image through three main formats. FIGURE 4-4 shows the captured image through each of its format transitions. The image was brought in as a 32-bit RGB image. Once an image was captured, the first step was to remove the luminance plane from the image. This converted the image from the standard 32-bit RGB image to an 8-bit image. Once the image was converted to 8-bit, a threshold filter was used to remove unnecessary information; specifically, pixel values that matched the water's surface. The threshold filter also converted the image into a binary format. Once the image was in binary format, additional filters were applied to remove the remaining excess data.

FIGURE 4-4: RGB image (left), greyscale (middle), and binary (right)

4.3.1   RSDC Calibration

Camera calibration was one of the most critical factors to help relate pixel coordinates to real-world measurements. Calibration was immensely significant to this research. The calibration provides the coordinates of floating debris that was detected. Thus, inaccurate calibration results in inaccurate information being relayed to the operational commands. LabVIEW's Vision Assistant application was used for pixel to real-world unit mapping. LabVIEW offered several different calibration models: simple, perspective, distortion, and microplane. A perspective calibration was chosen for the RSDC. This approach was used because the camera was not mounted directly perpendicular to the plane at which the object under inspection appeared. For perspective calibration to work, a minimum of four known points had to be identified. To increase the calibration accuracy, a template with multiple know distances was created. FIGURE

4-5 illustrates the selected template with the relative know distances. TABLE 4-1 provides the corresponding real-world coordinates to the corresponding letter seen in FIGURE 4-5. The template provided a complete range of coverage of the RSDC's FOV. Several photos with known object coordinates were used to validate the calibration during the testing phase.

TABLE 4-1: Real-World coordinates corresponding with the letters in FIGURE 4-5

Position	Theoretical Real-World Coordinates (ft, ft)
A	(-24, 24)
B	(-12, 24)
C	(0, 24)
D	(12, 24)
E	(24, 24)
F	(-18, 18)
G	(0, 18)
H	(18, 18)
I	(-12, 12)
J	(0, 12)
K	(12, 12)
L	(-6, 6)
M	(0, 6)
N	(6, 6)
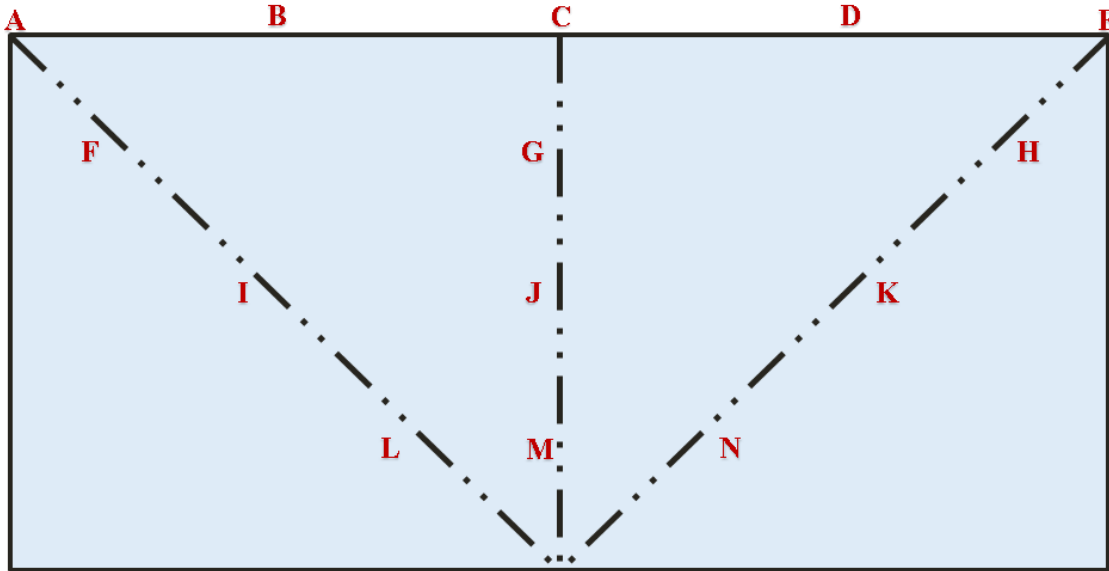
FIGURE 4-5: Image calibration template

Based on this calibration, a relative coordinate system was overlaid onto each processed image. FIGURE 4-6 shows an example of the coordinate overlay from the image calibration. As seen in the figure, the coordinate system is slightly skewed by a few degrees. Due to the camera's mounting and calibration, there was a bias to the left side of the USV, which was represented by the actual calibrated distances of the RSDC camera in the testing phase.

FIGURE 4-6: Example coordinate plane overlay

4.3.2   Intermediate Image processing

Following image calibration, several key image filtering steps were taken to reduce the overall noise experience within the operating environment. The sequence of these filters was found using empirical methods rather than theoretical speculations. Using this method, an overall centroid extraction accuracy of 91.1% was found. Also, the number of overall objects left in the image after processing was 1.19. As this number decreased, the overall accuracy of the process increased.

 The first step was converting the image to an 8-bit greyscale format to allow for further processing. This was done by removing the luminance plane from the captured image. FIGURE 4-7 shows the transition from the captured image to greyscale. One captured image was used as an example for all filtering processes except for the border object extraction.
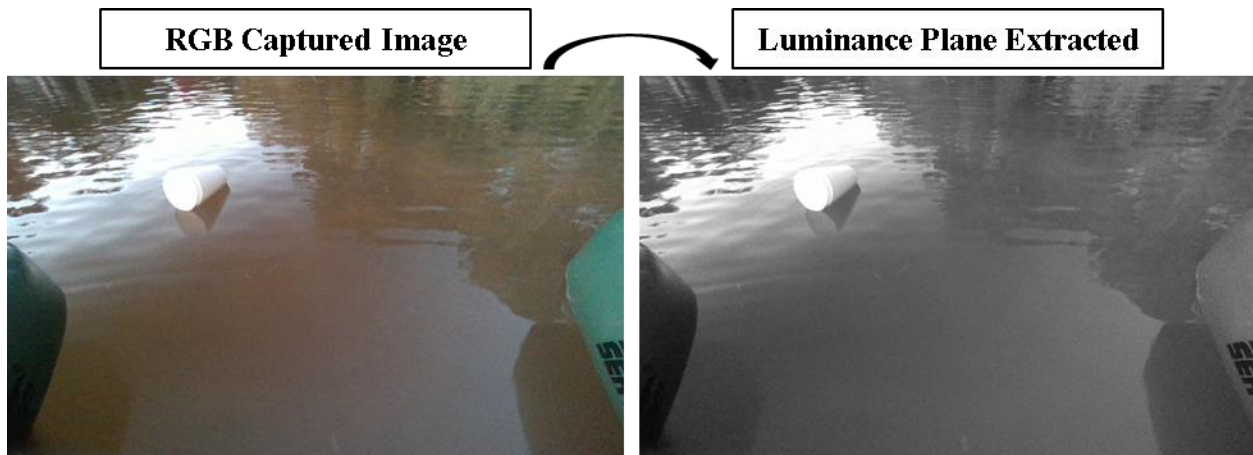
FIGURE 4-7: Transition to greyscale

Once the image had been converted to 8-bit format, an exponential lookup table was applied to the greyscale image. Exponential lookup tables applied an exponential transformation on the image pixels, specifically decreasing overall brightness and increasing contrast in bright regions. FIGURE 4-8 shows the transformation obtained by applying the exponential lookup

table. This filter allowed most of the water pixel intensity values to be transformed to have an intensity level of 0.
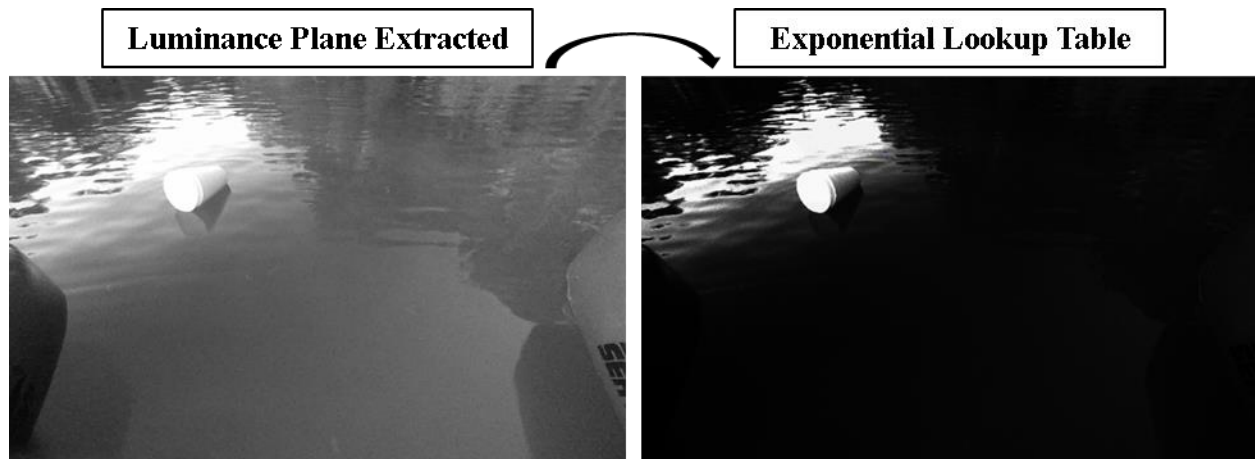
FIGURE 4-8: Transformation obtained through exponential lookup table

Now that the intensity values of the 8-bit image had been adjusted appropriately, the image was converted to binary format. This conversion gave each pixel an intensity value of either 0 or 1 based on the set threshold. Through testing, the threshold value used was 128. This allowed pixels with an intensity value greater than the set value of 128 to be converted to 1. Anything below that value was converted to 0. FIGURE 4-9 shows the conversion from 8-bit format to binary.
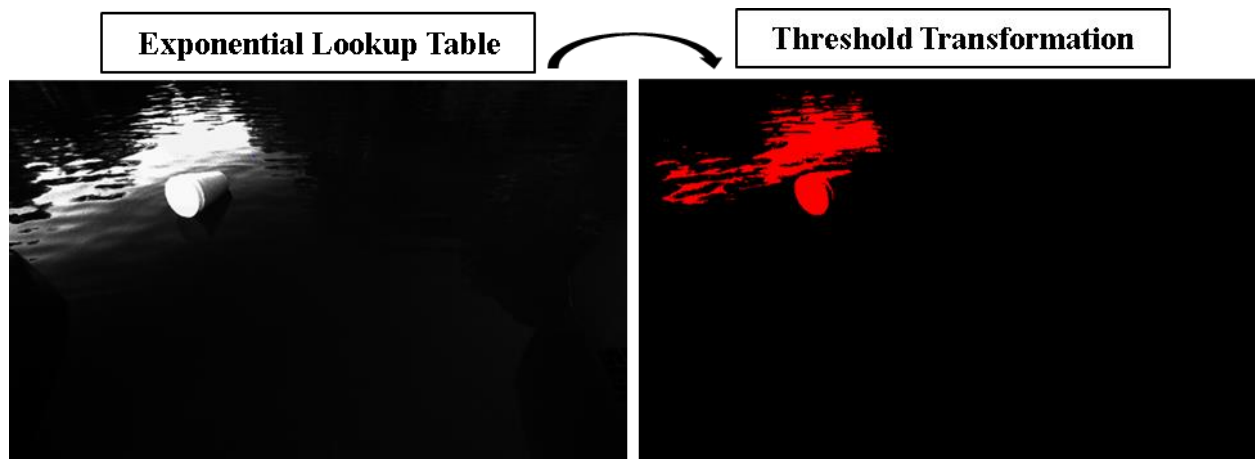
FIGURE 4-9: Binary transformation

Once the image was in binary format, several more filter options became available within Vision Assistant. The first to be used was the advanced morphology to reject any particle that is in contact with the border, and this was done to combat excessive reflection encountered during testing. FIGURE 4-10 shows the transformation obtained when this filter was applied to an image. When this filter was removed from the sequence of filters, the overall accuracy that the centroid extracted matched that of the floating debris decreased from 91.1% to 72.8%. Also, the average number of objects within a given image increased from 1.19 to 1.64. This increase in the average number of objects detected directly affected the overall accuracy of the system.
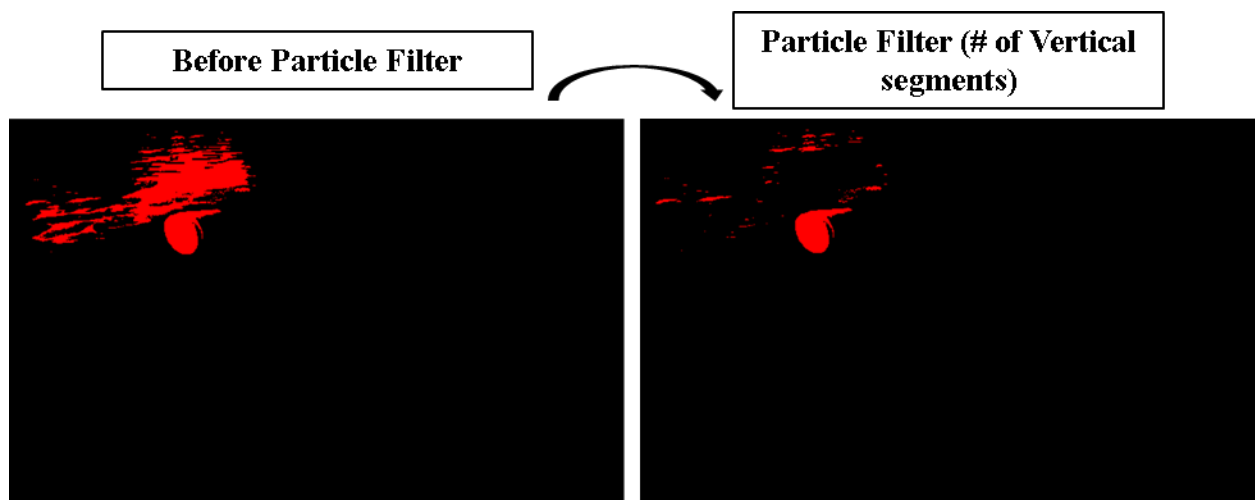
FIGURE 4-10: Border extraction Technique

To filter the background, particularly reflection from the water's surface, a particle filter was used. Specifically, a filter targeting the number of vertical segments within a given particle. As water ripples, the reflection becomes segmented, causing large numbers of vertical segments. This was not the case for floating debris, allowing the filter to be highly effective for removing excessive noise. The range of the particle filter allowed particles with 0-500 segments to remain in the image. FIGURE 4-11 shows the progression before and after the filter is applied.

Removing this filter decreased the centroid extraction accuracy by 5%. This was due to the average number of objects detected in an image increasing from 1.19 to 1.27.
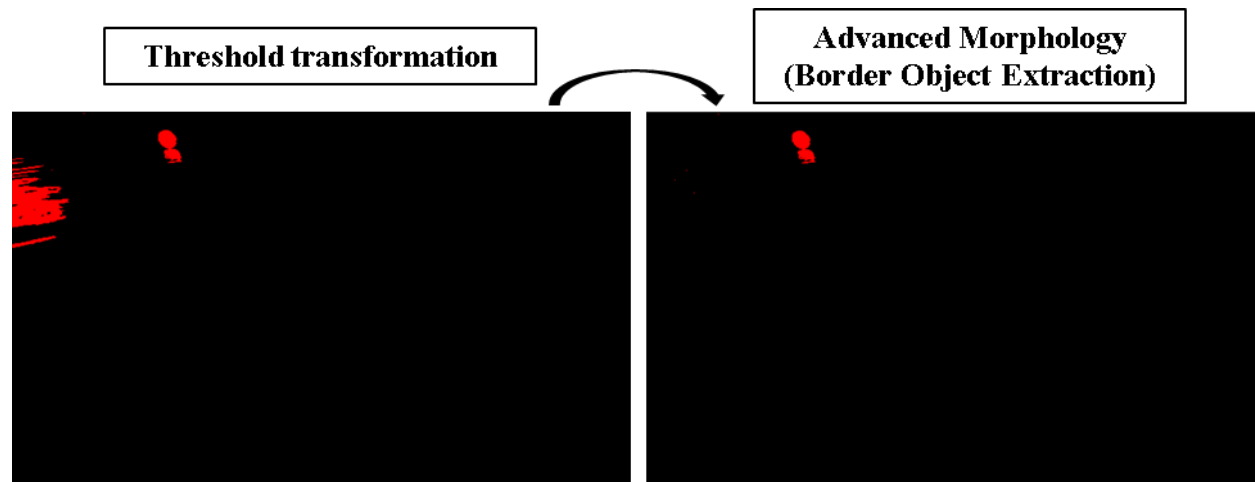
FIGURE 4-11: Evolution of image after first particle filter

A basic morphology filter was the next to be applied to captured images. This used an erode type of morphological transformation, eliminating isolated background particles. FIGURE 4-12 shows the transformation of an image before and after the erosion process. FIGURE 4-13 shows the setting used for the process. As the size and iterations increase, the number of small objects isolated in the background decreases. However, it was found that if this number was too large, it could filter out floating debris located further from the RSDC. Removing the erosion filter decreased the centroid extraction accuracy by 20.6%. This was due to the average number of objects detected in an image increasing from 1.19 to 1.7. This filter had the greatest impact in ensuring the correct centroid was extracted from a given image.
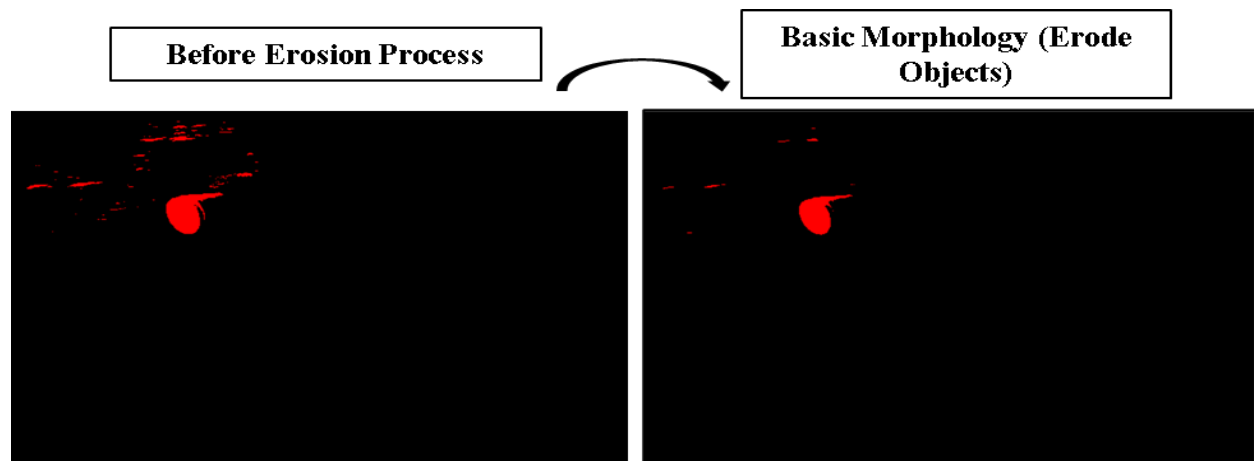
FIGURE 4-12: Erosion transformation example
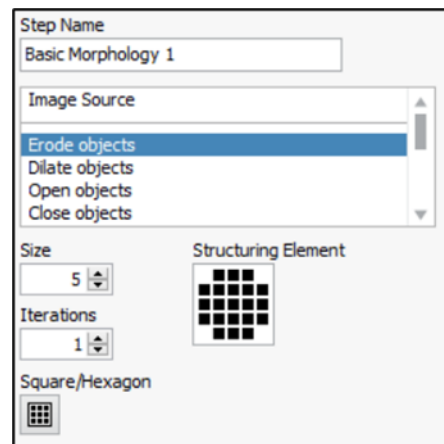
FIGURE 4-13: Settings for Erosion Process

The next step in the image filtering was removing any remaining small objects. This was accomplished using another advanced morphology transformation. The main benefit of using this rather than increasing either the size or number of iterations of the erosion transformation was that the filter only affects the small object, whereas the erosion method affected all the particles in a given image. FIGURE 4-14 displays the transformation of an image before and after the advanced morphology process. FIGURE 4-15 presents the setting used for the advanced morphology transformation. Removing this filter decreased the centroid extraction accuracy by 3.5%. This was due to the average number of objects detected in an image increasing from 1.19 to 1.26.
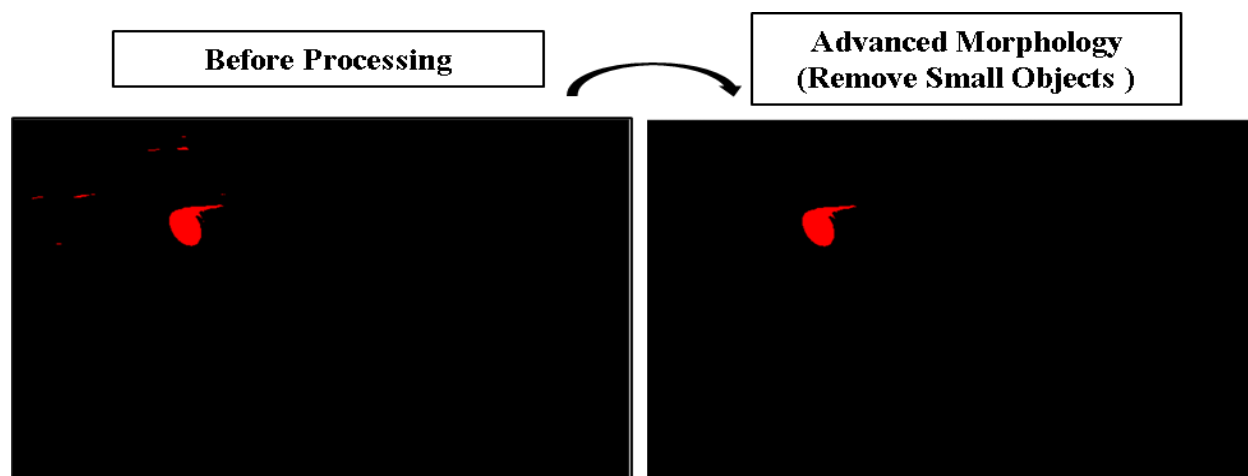
FIGURE 4-14: Small object removal technique
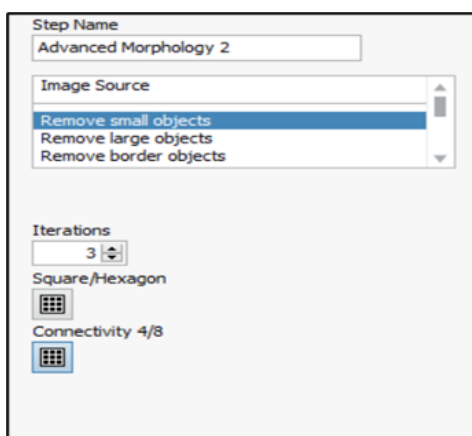
FIGURE 4-15: Removal of small objects from captured image

During the final steps, the captured image underwent a convex hull morphology transformation. This filter removed uneven edges and increased the overall area of a given particle. This was done before applying the final particle filter. FIGURE 4-16 demonstrates the transformation of the image when the convex hull morphology process was used. Removing this filter decreased the centroid extraction accuracy by 3.2%. This was due to the average number of objects detected in an image increasing from 1.19 to 1.2.
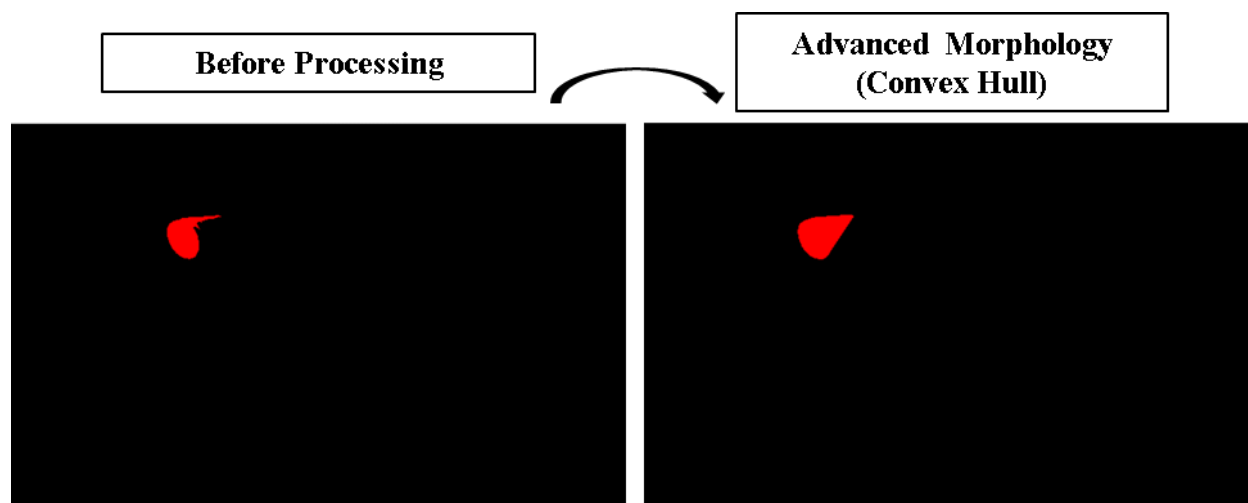
FIGURE 4-16: Advanced morphology (Convex Hull) transformation

The final filter used was based on particle area. The filter removed any particle that had

an area larger than 70,000 pixels or an area less than 200 pixels. These values were determined

during testing. The lower bound referred to the approximate size of debris located at 24 ft in

front of the USV. The larger threshold value referred to the maximum pixel size that could fit

between the two hulls of the USV. Removing this filter decreased the centroid extraction

accuracy by 4.2%. This was due to the average number of objects detected in an image

increasing from 1.19 to 1.25. FIGURE 4-17 shows a basic transformation of an image that had

the particle filter based on particle area applied.
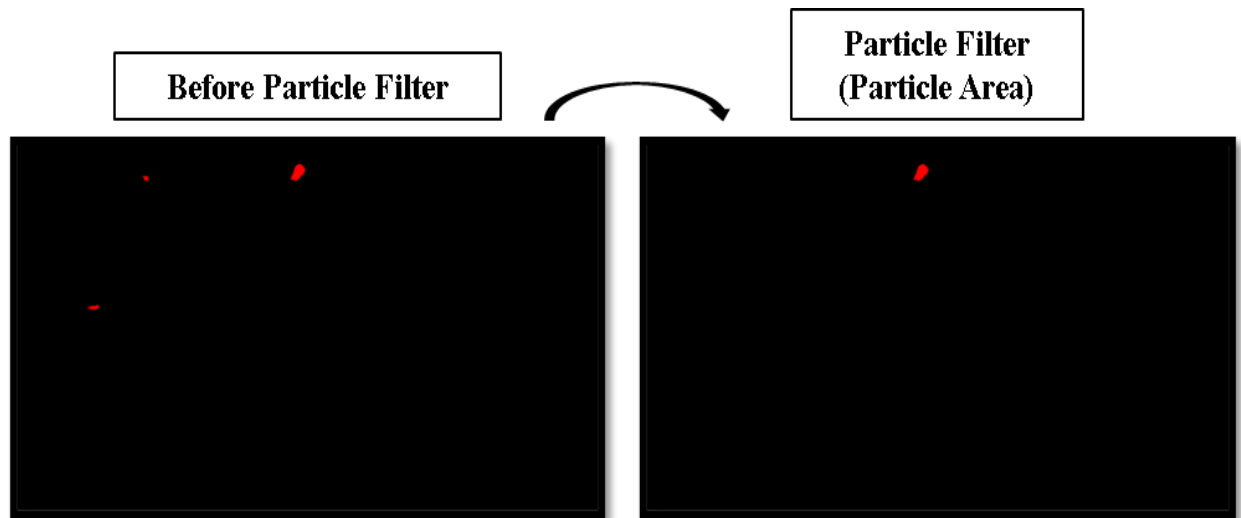
FIGURE 4-17: Image transformation using particle filter based on area

Though the object discovery algorithm was complex, it was not a taxing operation regarding the inspection time for a captured image. This was due to the image being converted early to binary format. FIGURE 4-18 presents inspection time results for the object discovery algorithm. This was accomplished using the Vision Assistant performance analysis tool. As presented in FIGURE 4-18, the average inspection time was between 9-10 milliseconds, with the color plane extraction step being the most time taxing. This time was used to create delays between this program initiating and running the maneuvering commands.
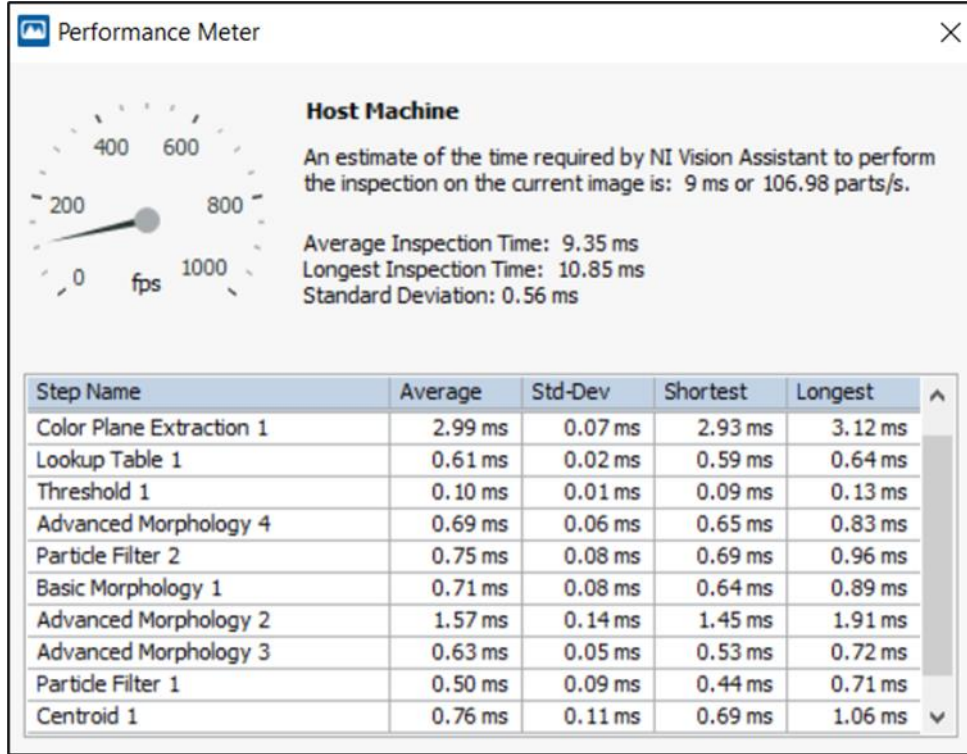
FIGURE 4-18: Average inspection time for object discovery algorithm

4.3.3 Centroid Extraction

The final step in the image processing for the object discovery system was centroid extraction. This was done using the particle analysis VI within LabVIEW. The object centroid (X and Y) was calculated by equations 4.5 and 4.6, respectively.

$$X = \sum_{i=1}^{n} \frac{\Sigma(X_i * PV_i)}{\Sigma PV_{i)}}$$ $\qquad$ 4.5

$$Y = \sum_{i=1}^{n} \frac{\Sigma(Y_i * PV_i)}{\Sigma PV_{i)}}$$ $\qquad$ 4.6

Where X_i is the X coordinate of the ith pixel, Y_i is the Y coordinate of the ith pixel and PV_i is the ith pixel value ranging from 0-1, where 0 is the minimum energy and 1 is the maximum energy. This pixel energy range is due to the format of the image being in binary

form. This range can also be 0-255 when using greyscale images. This same methodology can be

seen in [62].

FIGURE 4-19 shows an example of the centroid extraction of an image with floating

debris. Both the pixel coordinates and real-world coordinates are presented. These values were

used to estimate the distance of the floating debris relative to the center of the USV. For the

given example, the real-world X coordinate is negative. This was due to the calibration of the

camera being relative to the center of the USV. Anything to the left of center was denoted with a

negative to ensure correct angle assignment.
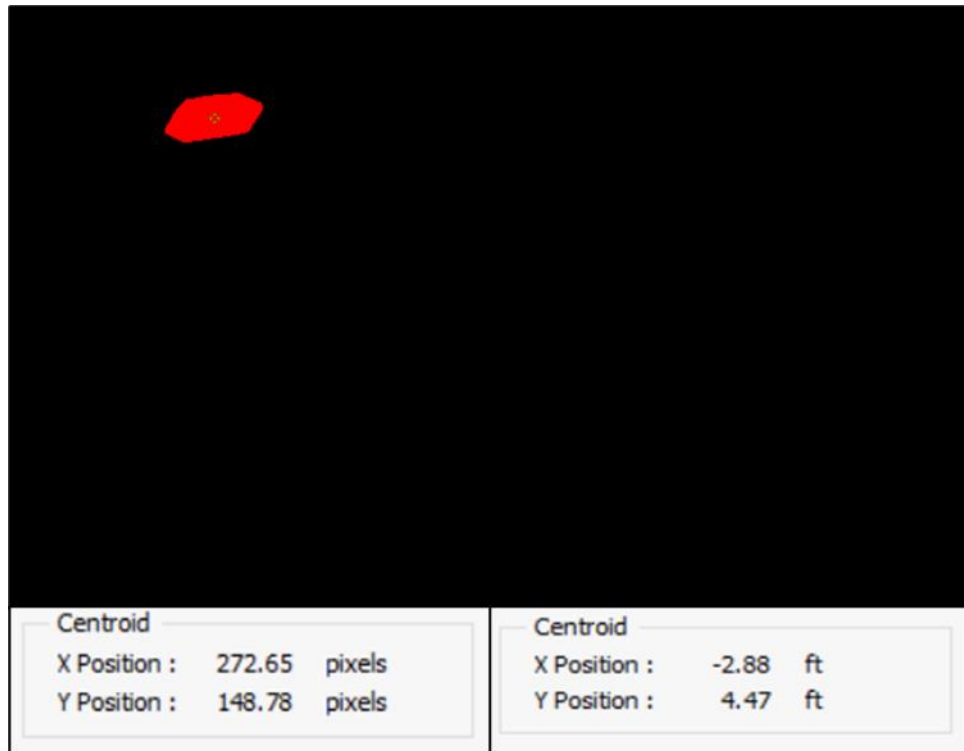
FIGURE 4-19: Example centroid extraction with corresponding X and Y coordinates

The values obtained from this measurement were in feet due to the calibration used in

previous image processing steps. The X and Y coordinates were then used to calculate the angle

at which the floating debris was located from the center of the USV. Utilizing a simple

understanding of trigonometry, this angle was calculated using equation 4.7.

$$\emptyset = \tan^{-1}(\frac{X}{Y}) \qquad\qquad 4.7$$

4.4   USV Maneuvering Autonomy

The overall automation of the USV is implemented by the myRIO controller. To control the USV, the myRIO acquired data from the processed images, and this data was converted and delegated to designated outputs for each driving component. The overall maneuverability of the USV is summarized in the flowchart in FIGURE 4-20. The USV must traverse an obstacle-free aquatic environment to the floating debris to allow extraction. This was accomplished by capturing data from the RSDC to calculate the angle of the floating debris relative to the center of the USV. In response to this data, the servo motor was commanded to adjust the angle of attack (AOA) the USV approached to intercept the floating debris. The AOA was continuously adjusted until the extraction mechanism reached the authentication state.
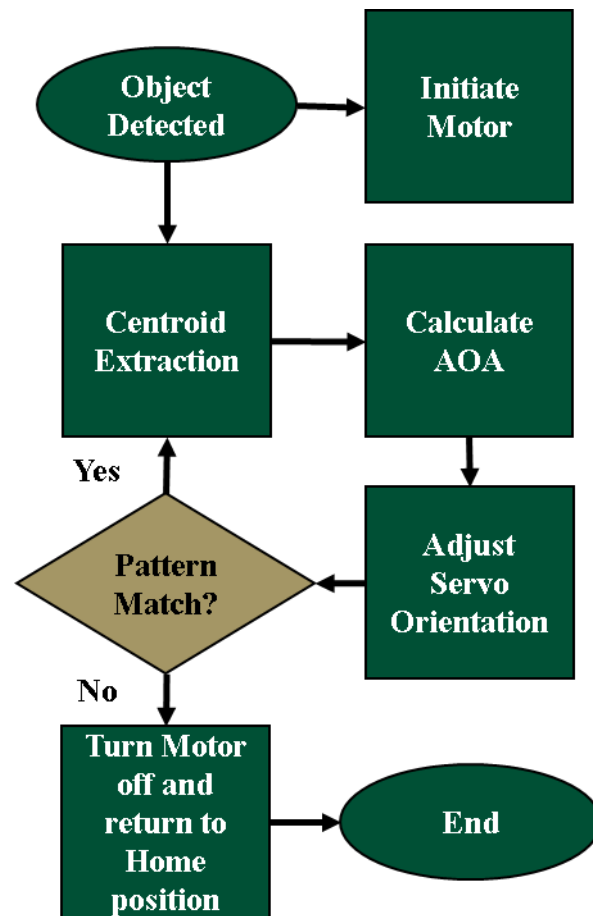
FIGURE 4-20: Maneuvering operations flowchart

The myRIO sends pulse width modulation (PWM) signals to both the motor controller

and servo motor. By varying the PWM signal, speed and direction can be adjusted. The servo

control was designed to be adjusted between negative 90 degrees and positive 90 degrees. The

throttle of the USV motor was adjusted between 0% and 100% in both the forward and reverse

directions. The Talon speed controller and the servo expected a PWM signal between 1 to 2 ms.

A frequency of 333 Hz was used for the PWM signal produced. This value was set due to

hardware limitations of the lowest PWM frequency produced by the myRIO. A frequency of 333

Hz produced a signal period of 3 milliseconds, as obtained by equation 4.1. Using this period as

a base, the forward, stop, and reverse throttle values were calculated using equations 4.2, 4.3, and

4.4 such that the maximum reverse duty cycle was 0.33, the stopping duty cycle was 0.5, and the

maximum forward duty cycle was 0.67. These values were applied to both the TRAXXAS servo

control and Talon SRX motor controller.

$$Period = \frac{1}{f} = \frac{1}{333Hz} = 3ms \qquad\qquad 4.1$$

$$DC_r = \frac{1(ms)}{Period} = \frac{1}{3} = 0.33 \qquad\qquad 4.2$$

$$DC_s = \frac{1(ms)}{Period} = \frac{1.5}{3} = 0.50 \qquad\qquad 4.3$$

$$DC_f = \frac{1(ms)}{Period} = \frac{2}{3} = 0.67 \qquad\qquad 4.4$$

4.4.1   Heading Autonomy

For purposes of this research, the motor controller was set to have a constant duty cycle

signal to allow for uniform velocity. However, the servo required its duty cycle to be varied over

its complete range of 0.33 to 0.67. This provided the USV the ability to adjust its heading

according to the location of the floating debris. The range from 0.33 to 0.5 was used for the USV

to adjust its heading to the left (port). The range from 0.5 to 0.66 was used for the USV heading

to be adjusted to the right (starboard).

To determine the control signals to provide the servo, a simple diagram was created.

FIGURE 4-21 illustrates the diagram used to set the command to the servo based on floating

debris located within the FOV of the RSDC. Since the FOV of the camera was known to be 90

degrees (45 degrees to either side of the center), the maximum distance to the right or left was

calculated to be 24 ft. The center-to-center distance between the USV hulls is known to be 3 ft.

Due to this, the 24 ft distance was broken into equal segments of 3 ft. This allowed the minimum

and maximum angles to be determined for any given segment. Based on this angle, a designated

command was sent to the servo to adjust its position accordingly.
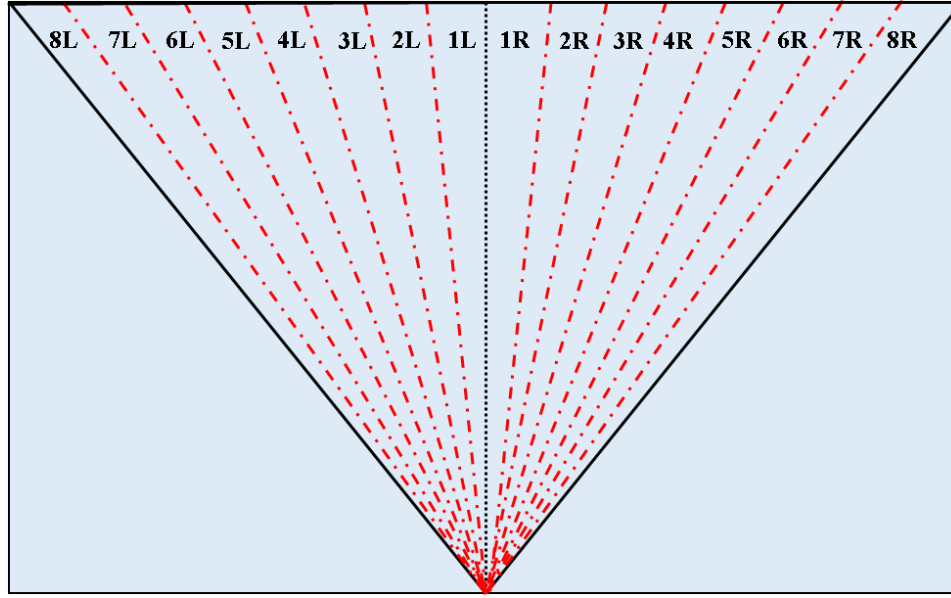
FIGURE 4-21: Each angle range with corresponding reference to dc values in TABLE 4-2

TABLE 4-2 shows each value used with the corresponding angle range for both left and right turns. The duty cycle values were selected based on the measured real-world change in motor angle for each given duty cycle value. These values were also validated during testing.

TABLE 4-2: The duty cycle values used to control AOA of the USV

Turning USV Right					
Reference	Min Ratio (X/Y)	Max Ratio (X/Y)	Min Angle(ø)	Max Angle(ø)	Duty Cycle Input
1R	0	0.125	0	7.125	0.51875
2R	0.125	0.25	7.125	14.035	0.5375
3R	0.25	0.375	14.035	20.555	0.55625
4R	0.375	0.5	20.555	26.565	0.575
5R	0.5	0.625	26.565	32.005	0.59375
6R	0.625	0.75	32.005	36.87	0.6125
7R	0.75	0.875	36.87	41.186	0.63125
8R	0.875	1	41.159	45	0.65
Turning USV left					
Reference	Min Ratio (X/Y)	Max Ratio (X/Y)	Min Angle(ø)	Max Angle(ø)	Duty Cycle Input
1L	0	0.125	0	-7.125	0.48125
2L	0.125	0.25	-7.125	-14.035	0.4625
3L	0.25	0.375	-14.035	-20.555	0.44375
4L	0.375	0.5	-20.555	-26.565	0.425
5L	0.5	0.625	-26.565	-32.005	0.40625
6L	0.625	0.75	-32.005	-36.87	0.3875
7L	0.75	0.875	-36.87	-41.186	0.36875
8L	0.875	1	-41.159	-45	0.35

A LabVIEW program was written to position the servo that utilized the angle obtained

from the object discovery system to determine the correct corresponding duty cycle value. An

example of this can be seen in FIGURE 4-22. In this example, the shared variable *Adjusted*

Angle (Left) was compared to see if it fell between the angle of -20.555 degrees and -26.565

degrees. If this were TRUE, then the duty cycle of the PWM signal sent to the servo would be

0.425. As indicated by the angle, this was implemented for objects to the left of center.
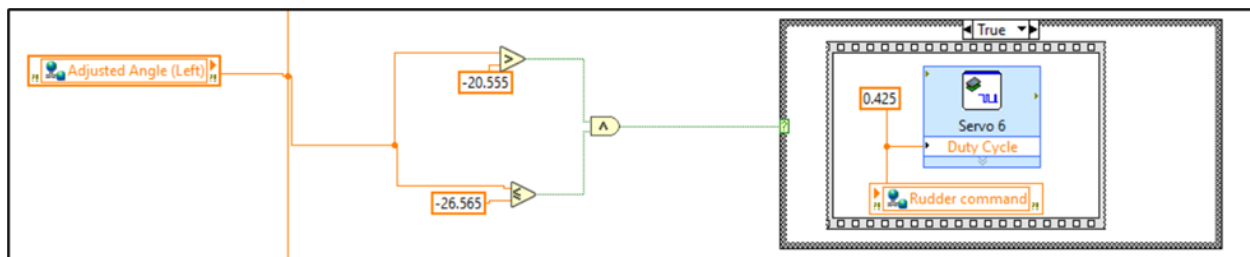
FIGURE 4-22: LabVIEW Example of comparing acquired angle and setting dc for servo input

FIGURE 4-23 provides a more detailed data flow for the automated servo command. The

program was designed to check multiple values before adjusting the dc setting of the servo. Once

the X and Y coordinates of the centroid were extracted from the object discovery program, the

AOA was calculated and stored. Following this, the extracted X coordinate was compared to 0. If

the X value was 0, the identified floating debris was located directly in front of the USV. When

this scenario was encountered, the servo was either set to the home position or maintained the

home position. However, if this was FALSE, then the program moves to the subsequent

comparison. The subsequent comparison determined whether the USV needed to turn right or

left. If the X coordinate was greater than 0, the identified floating debris was located to the right

of center or on the USV's starboard side. If the value was less than 0, then the identified floating

debris was located to the left of center or port side of the USV. In either of these cases, the

program adjusted the servo orientation accordingly. This process continued until the identified

floating debris was captured. Upon capture, the servo was returned to the home position.
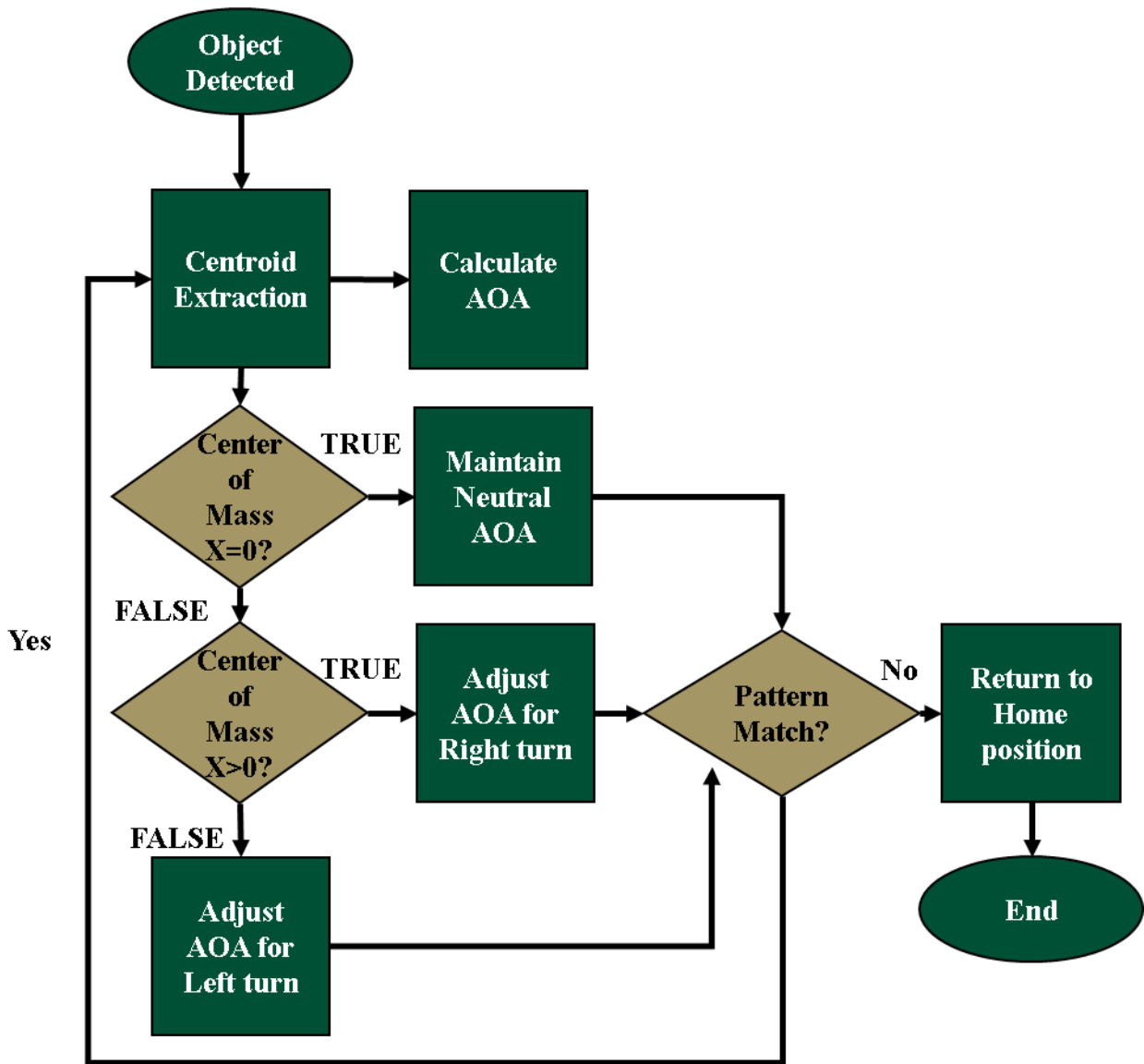
FIGURE 4-23: Data flowchart for LabVIEW program

4.5   Extraction System Autonomy

Once the floating debris was located, the extraction system removed the located debris

from the environment and placed it on the USV. A summary of how the extraction system

operates is presented in FIGURE 4-24. As images were captured and processed in the object

discovery system, the extraction mechanism was maintained in the standby state. Once an object

was detected, the extraction mechanism was positioned into the deployed state. After the

deployed state, the extraction system was placed in the authentication state before performing the

pattern matching algorithm. If the algorithm did not verify the pattern, then the extraction

mechanism disposed of the debris onto the USV and recorded current GPS longitude and

latitude. However, if the algorithm verified the pattern, the extraction mechanism performed a

second run through the extraction deployment. If the pattern was still verified after the second

deployment, the longitude and latitude were recorded, and the extraction system returned to

stand-by.
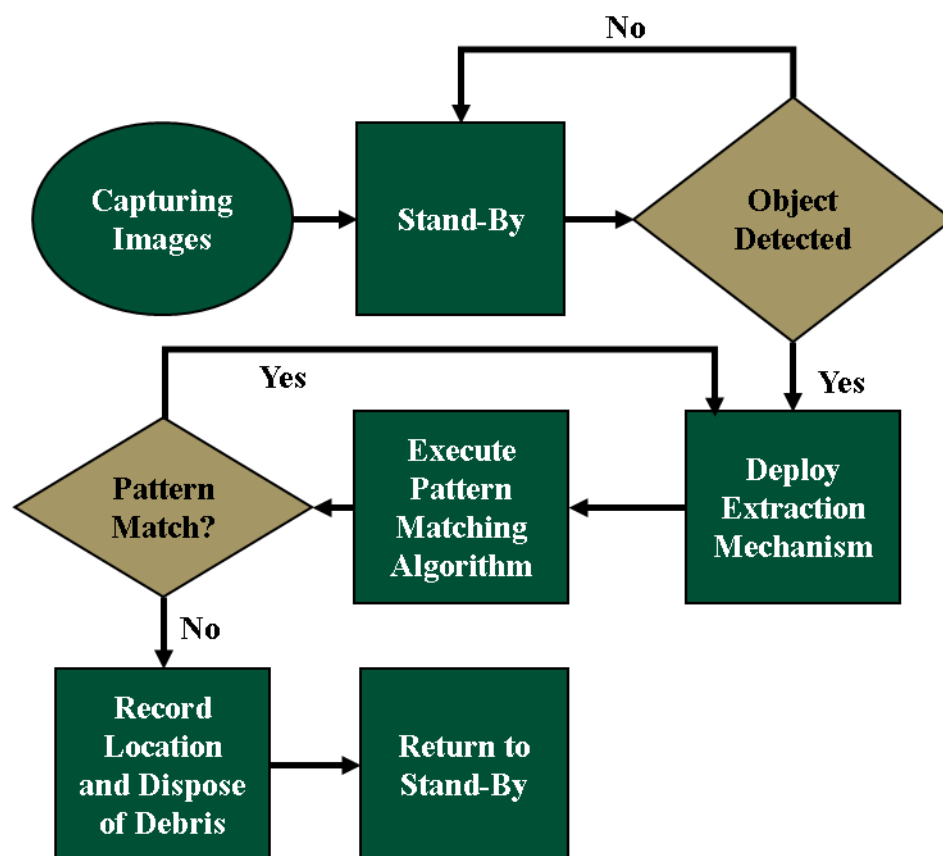
FIGURE 4-24: Extraction system flowchart of operations

4.5.1   Verification Pattern Calibration

To verify whether the floating debris was captured, a checkered pattern was installed at

the base of the extraction mechanism. When the mechanism was empty, the verification camera

would see the pattern. However, when the mechanism was not empty, the verification camera

would not detect the pattern. To accomplish this, a calibrated pattern was created and used as a template to compare to during USV operation.

During the initial stages of testing, several combinations of filters were used and analyzed within the Vision Assistant software. These combinations were narrowed down between two main scripts. The only difference between the two scripts was the incorporation of the brightness correction tool. The overall average inspection time for each of the scripts was found using the performance meter tool within the Vision Assistant software. FIGURE 4-25 and FIGURE 4-26 show the overall processing time for the script with and without the brightness correction, respectively.

Host Machine

An estimate of the time required by NI Vision Assistant to perform the inspection on the current image is: 35 ms or 28.86 parts/s.

Average Inspection Time: 34.65 ms
Longest Inspection Time: 54.71 ms
Standard Deviation: 9.03 ms

Step Name	Average	Std-Dev	Shortest	Longest
Color Plane Extraction 1	5.94 ms	0.03 ms	5.90 ms	5.99 ms
Pattern Matching 1	26.48 ms	5.65 ms	23.51 ms	41.51 ms

FIGURE 4-25: Verification script without Brightness Correction Performance Analysis

Host Machine

An estimate of the time required by NI Vision Assistant to perform the inspection on the current image is: 39 ms or 25.67 parts/s.

Average Inspection Time: 38.95 ms
Longest Inspection Time: 52.89 ms
Standard Deviation: 6.48 ms

Step Name	Average	Std-Dev	Shortest	Longest
Brightness 1	14.74 ms	0.14 ms	14.59 ms	15.09 ms
Color Plane Extraction 2	3.35 ms	0.07 ms	3.29 ms	3.54 ms
Pattern Matching 1	21.22 ms	6.43 ms	17.72 ms	34.88 ms

FIGURE 4-26: Verification script with Brightness Correction Performance Analysis

The overall average inspection time for the script without the brightness correction was approximately 35 milliseconds, while the script with brightness correction was approximately 39 milliseconds. The brightness correction filter inspection time was approximately 15 seconds. However, the color plane extraction and pattern matching inspection times decreased to 3 seconds and 21 seconds, respectively. The difference in the processing time was negligible since either of these scripts only needed to be processed one time. However, knowing the overall average inspection time allowed for the correct wait time between the verification algorithm and the extraction mechanism's next move.

Due to results from testing and the processing speed comparison, the script containing the brightness correction was selected for the extraction verification process. FIGURE 4-27 shows each image processing stage for the extraction verification from the original image to pattern matching. Three main image processing tools within NI Vision Assistant were used to accomplish consistent and accurate pattern matching, brightness correction, color plane extraction, and pattern matching.

Brightness correction was used due to the presence of shadowing. The brightness correction VI included four adjustable parameters, brightness, contrast, gamma, and color plane. The values for each of these parameters can be seen in TABLE 4-3. The brightness values ranged from 0-255, with the neutral value not changing the photo being 128. As this value increases, the return photos brightness also increases. For the second parameter, contrast, the default value is 45 with a range of 1-89. As this value increases, the contrast of the returned image also increases. The gamma parameter provided a unique way of adjusting the contrast within the captured image. The neutral value was 1 and had a range from 0-10. Values greater than 1 gave extended contrast for small pixel values and less contrast for large pixel values. For

values less than 1, the return image had less contrast for small pixel values and extended contrast

for large pixel values. The image after the brightness correction had been completed can be seen

by the top right image in FIGURE 4-27.

TABLE 4-3: Brightness VI parameters

Brightness	128
Contrast	45
Gamma	10
Color Plane	Blue

Once the parameters were set, the next step was performing a color plan extraction of the

image. This converted the 32-bit RGB image to an 8-bit greyscale image. The blue color plane

was extracted, allowing the objects to become variations of grey. The greyscale image obtained

once the color plane had been extracted can be seen via the bottom left photo of FIGURE 4-27.

Once this was complete, the pattern matching was accomplished. To ensure accuracy,

several settings were adjusted within the sub-VI. TABLE 4-4 presents the parameters used for

the pattern matching VI. The rotation parameter allows the pattern to appear between an offset of

-10° and 10° from the original pattern. A pyramidal matching algorithm was selected to improve

the computation time of pattern matching. This specific technique reduced the size of both the

image and template by one-fourth of their original size for every successive pyramid level using

Gaussian pyramids. However, two kinds of data can be used in this algorithm: gray values and

gradients. The gray value method is based on the pixel intensities, whereas the gradient method

is based on selected edge information. For this research, the grey value method was selected.

This method reduced processing time by a third and allowed for better variations in light

intensities. The minimum match score was set based on data captured in the testing phase. This

value ensured that if any floating debris were within the extraction mechanism, the match score would be below the given threshold of 850.

TABLE 4-4: Pattern Matching Parameters

Rotation	-10 to 10
Overlapping Objects	No
Low Contrast	Yes
Large Template	No
Screenshot	No
Algorithm	Correlation - Value Pyramid
Minimum Match Score	850

The Vision Assistant script described above was then transferred into a LabVIEW program as an express VI. Once the script was configured within the LabVIEW application, several indicators and controls were selected and used to gather critical data within the LabVIEW program. The region of interest (ROI) control was used for the express VI. The ROI control allows the user to specify where the program should search for the specified pattern. This resulted in faster processing times and limited the chances of false positives. The ROI parameters can be seen in TABLE 4-5. The ID type refers to whether the program looks within the ROI or outside the ROI for the pattern. An external ID was used, which allowed the program to search within the designated ROI for the pattern. A rectangle ROI was used due to how the verification camera perceived the extraction mechanism. The rectangle shape contour allowed for a close match of the extraction mechanism outline. Once the ID and contour type was selected, the coordinates for the rectangle contour were set. For the rectangle contour, the top-left and bottom-right coordinates were used to map the complete rectangle. The selected coordinates corresponded with the top left and bottom right corners of the extraction mechanism. Due to the majority of the captured images containing irrelevant data, this was a necessary step. The bottom right image from FIGURE 4-27 shows the designated ROI in green.

TABLE 4-5: ROI parameters used in verification matching

ID	External
Shape	Rectangle
Left (X-Coordinate/ Left Corner)	110
Top (Y-Coordinate/ Left Corner)	380
Right (X-Coodinate/ Right Corner)	1460
Bottom (Y-Coordinate/ Right Corner)	1050

Indicators for the express VI were matches, number of matches, and image output. The matches indicator provides crucial data such as the pixel location in the X and Y coordinate plane, offset angle, scaling, and finally, the match's score. However, the most crucial indicator was the number of matches. If this value was anything greater than zero, that meant the program could find a match, meaning that the floating debris was not captured. If the pattern is found within the image, it indicates the pattern using a red rectangle with a point located in the center. This can be seen in the bottom right photo of FIGURE 4-27.
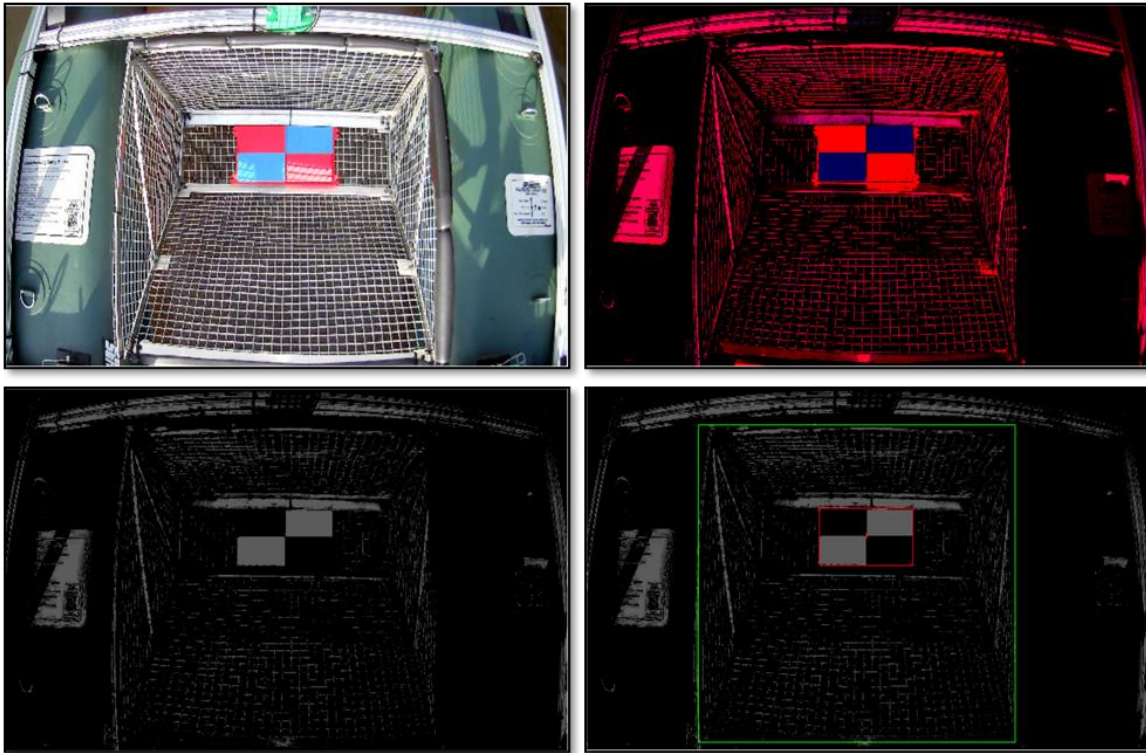
FIGURE 4-27: Verification processed pattern

4.6 Extraction Drive System Autonomy

The extraction drive system was utilized when the extraction mechanism was deployed. This system comprised a NEMA 23 stepper motor, a gearbox with a 77:1 gearing ratio, and a STEPPERONLINE stepper motor micro driver. These components are driven using digital HIGH/LOW signals to provide the angle of rotation and rotation direction. The stepper motor driver allowed the stepper motor to be driven by a technique called "Micro-stepping." This technique allowed for smoother transitions between set points by reducing the number of degrees per step.

The stepper motor driver chosen allowed for various settings to be adjusted, allowing for multiple combinations for any given scenario. TABLE 4-6 shows the setting used for the STEPPERONLINE DM542T stepper motor driver. The table shows that SW1 toSW4 switches controlled the drive current supplied to the stepper motor. Switch 4 (SW4) controlled the standstill current being supplied to the stepper motor when not being operated. Specific combinations are characterized by FIGURE A-1 in the appendix. The maximum rated drive current of the NEMA 23 stepper motor was 2.8 A. Using the combinations presented in TABLE 4-6, the max current allowed to the stepper was 2.84 A with an average drive current of 2.03 A. In the ON state, the standstill current was the same as the dynamic current, while in the OFF state, it was half of the dynamic current.

To adjust the number of steps needed to complete one rotation of the stepper motor switches SW5 to SW8 were changed to the combination seen in TABLE 4-6. Other combinations of these switches and their respective step outputs are detailed in FIGURE A-2 in the appendix. This specific combination allowed a 1.8 degrees per step (200 steps per revolution) stepper motor to be cut in half to 0.9 degrees per step as characterized by equation 4.8. Since the

stepper motor was connected to a gearbox with a 77:1 gearing ratio, the actual amount of rotation

was divided by 77, as illustrated using equation 4.9. Equation 4.10 considers the LabVIEW script

seen in FIGURE 4-28. A NOT function and shift register modified a digital HIGH/LOW signal

into a PWM signal. A NOT function returns a value opposite of the input. If the input were

HIGH, then the output would be LOW. Using this method generated a dc of 50% and required

two iterations to complete one full pulse. Once each of these parameters was adjusted, the degree

per step was 0.0058 degrees per step. This value became the constant from which any set

position could be calculated. For this research, all stepper motor movements were either 90

degrees clockwise or 90 degrees counterclockwise. For 90 degrees, the number of loop iterations

required was 15400, as seen in equation 4.11. This value can be seen in the upper right corner of

the LabVIEW function in FIGURE 4-28.

$$\underline{Stepper\ Driver}: \qquad ADPS = \frac{200\ steps}{1\ rev} * \frac{1\ rev}{400\ steps} = 0.5 * \frac{1.8°}{step} = \frac{0.9°}{step} \qquad\qquad 4.8$$

$$\underline{Gearbox}: \qquad\qquad ADPS = \frac{0.9°}{step} \div 77 = \frac{0.0117°}{step} \qquad\qquad 4.9$$

$$\underline{LabVIEW\ Program}: \qquad ADPS = 0.0117 \div 2 = \frac{0.0058°}{step} \qquad\qquad 4.10$$

$$Loop\ Iterations = \frac{Desired\ Rotation\ (°)}{0.0058} = \frac{90°}{0.0058} = 15400 \qquad\qquad 4.11$$
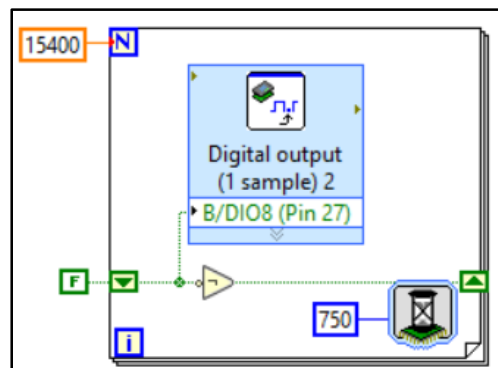
FIGURE 4-28: Example of for loop controlling stepper motor direction

TABLE 4-6: Selected parameters for the stepper motor driver

SW1-SW4 Controls Current	
SW1	ON
SW2	ON
SW3	OFF
SW4	ON
SW5-SW8 Controls Microsteps	
SW5	OFF
SW6	ON
SW7	ON
SW8	ON

FIGURE 4-29 illustrates the overall flow of the extraction drive system autonomy. Once the deployment has been initiated, the extraction mechanism is rotated 90° clockwise. This is known as the *Deployed* state. This allowed the extraction mechanism to be submerged into the water by 7 inches, ensuring any floating debris would be captured. It remained in this position for a set time of 10 seconds. Due to the setup of the RSDC camera, the max distance of an object was known to be 24 ft. As a result, the maximum travel time to an object can be calculated. Once this time had elapsed, the extraction mechanism was rotated counterclockwise 90 degrees before reaching the *Authentication* state. This state is where the pattern matching algorithm was executed. If the algorithm located the pattern, the extraction mechanism returned to the deployed state and captured any missed floating debris. However, if the pattern did not match, the drive system rotated the extraction mechanism counterclockwise another 90 degrees to the *Dispose* state. The captured debris was disposed of onto the USV. The final drive function was a clockwise rotation of 90 degrees to reach the *Stand-by* state.
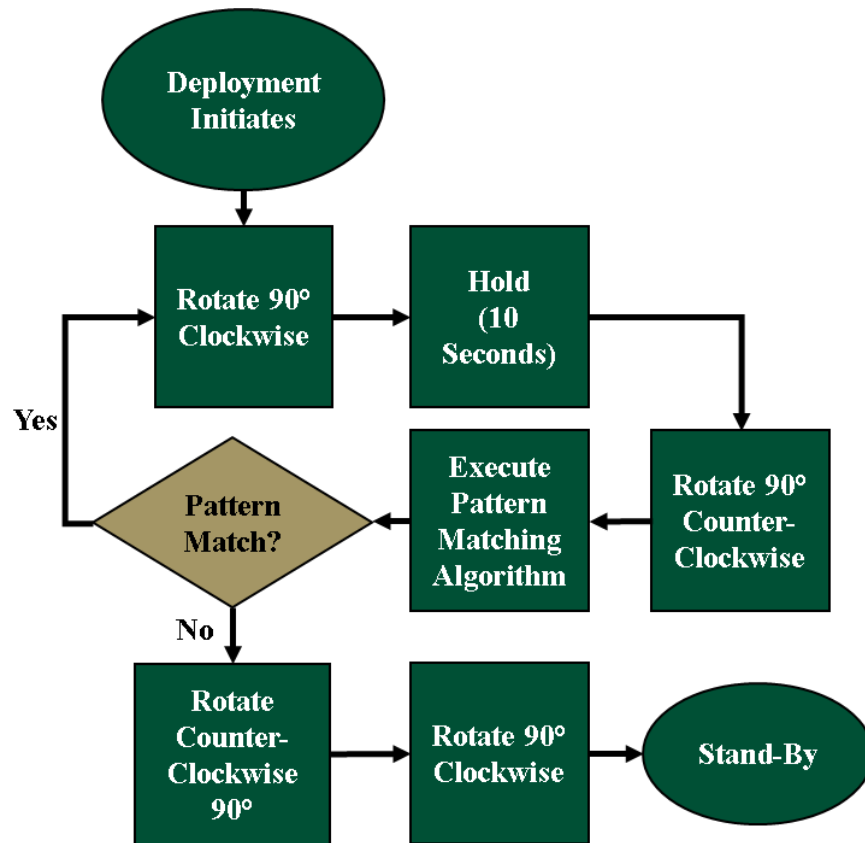
FIGURE 4-29: Extraction drive system flow chart

CHAPTER 5: TEST PLAN

5.1 Aquatic Environment

The OLARP was designed specifically for freshwater environments. Testing of the OLARP was completed at Lake Norman, North Carolina. A specific environment layout was chosen for testing the OLARP design. FIGURE 5-1 represents the general layout of the test environment. A swim lane approach was taken to discover floating debris. As the USV is maneuvering across the environment, it constantly searches for floating debris. Once the USV locates floating debris along the surface of the water, it adjusts the path of the USV as seen in the top right diagram of FIGURE 5-1. It continues adjusting the path to orient the floating debris between the two hulls of the USV. This is represented by the bottom left image in FIGURE 5-1. The final step of the operations included capturing and extracting the floating debris from the aquatic environment, as seen in the bottom right image of FIGURE 5-1.
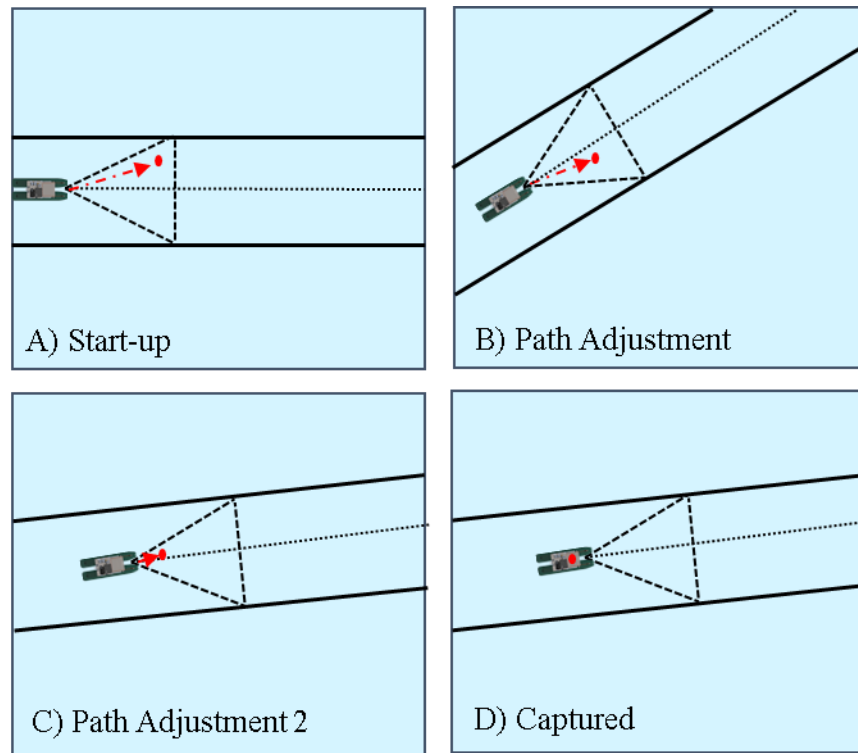
FIGURE 5-1: Aquatic testing environment layout

When the USV was facing towards the sun, images captured from the object discovery system were found to have extreme amounts of reflection. This caused higher inaccuracies in the object discovery algorithm. To prevent this issue, the USV was oriented facing away from the sun. Testing was conducted in both morning conditions and evening conditions. Typically, between the times of 7:30 AM to 12 PM EST and 4:00 PM to 7:PM EST. The last setup requirement that was met before initiating the OLARP was to ensure that the USV was in an open water scenario. This ensured that it would not encounter any obstacles before completing the swim lane.

5.2 Sample Pollution

The sample pollution for this research utilized real-world examples of some of the most commonly found pollution within the world's waterways and oceans. The sample pollutants are as follows: plastic bottle (20 oz), polystyrene cup (24 oz), plastic bottle (2-liters), aluminum can (16 oz), standard take-out container. The sample pollutants are displayed in FIGURE 5-2.
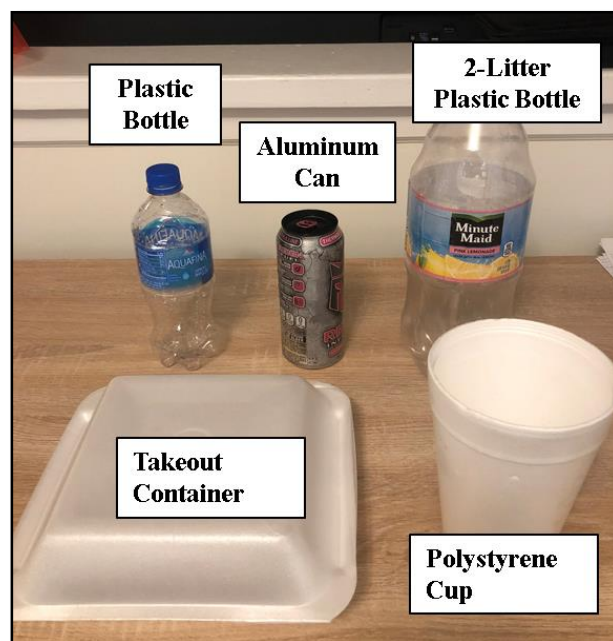
FIGURE 5-2: Sample Pollution used during experiments

5.3   Velocity Testing

One of the first tests performed was to determine the velocity of the USV for a range of

given inputs. This allowed for the max time to locate debris to be determined. To accomplish

this, the USV was transported to Lake Norman, North Carolina. To perform this test, a set of

manual controls were created to allow for real-time adjustment of both the servo command and

the motor controller. Also used for this portion of the testing was a data logging program that

recorded motor command, servo command, and ground speed in feet per second. The ground

speed was obtained using the GlobalSat GPS receiver located on the USV. Once the USV was

placed into the environment, the USV was positioned to be going against any waves or current

present in the environment. At the end of each test, the USV would be repositioned in the same

location, and the next motor command value would be tested and recorded. This was completed

for the entire range of motor command values (0.33 to 0.66). The velocity data gathered would

be assessed to determine the appropriate speed during operation.

5.4   Camera Calibration Testing

Following the velocity test, the second test verified the accuracy of the camera

calibration. To verify the calibration, twenty-five additional images were captured with an object

placed at know distances. The X and Y coordinates of these objects were recorded and used later

for comparison. Once the test images were captured, they were imported into NI Vision

Assistant, where the saved image calibration was overlaid onto the test image. Using the

"measuring" tool within Vision Assistant, the real-world X and Y coordinate of any random

object could be extracted. These values were recorded and compared to the known X and Y

coordinates recorded when the image was taken.

5.5   Pattern Verification Testing

One of the main tests of the extraction system was that of the pattern matching algorithm and determining which combination of filters produced the highest confidence scores. Another factor that was determined to be important was the scenario in which this testing was accomplished. The pattern was tested in a laboratory environment for the first test without any outside variable consideration such as shadowing, brightness changes, and varying contrasts. These factors would later become essential and drive changes to the overall pattern matching algorithm. This led to testing the algorithm while deployed in an aquatic environment. Several samples of the pattern matching algorithm were captured, both with and without floating debris. Once each sample was tested and the confidence score recorded, an appropriate threshold value was selected.

5.6   Extraction System Testing

Before moving into the aquatic environment, the extraction system was tested in a controlled environment to ensure that the loop would execute as intended. The test ensured that the extraction mechanism would rotate the correct amount for each state. Also, the combination of incorporating the pattern matching algorithm to the extraction mechanism program was tested. This test was considered passed if the system could perform the correct sequence based on whether any debris was located in the mechanism.

5.7   Full-Scale Autonomy Testing

As mentioned in Chapter Three, the final test was performed at Lake Norman, North Carolina. Several key data points were recorded during the final tests. These included: 32-bit RGB image from the object discovery and both the greyscale and binary counterparts, the 32-bit

RGB verification images taken during the verification process, USV speed, GPS Latitude, and

Longitude upon extraction, and rudder commands (servo inputs).

Once the boat was placed in the test environment, each LabVIEW program was initiated.

This allowed the USV to operate as intended when given the initiation command from the user

interface. After all the LabVIEW programs were deployed, the USV was positioned facing away

from the sun. The floating debris was then placed at random in front of the USV. Once the

previous steps were complete, the data logging and the USV state machine were initiated using

the user interface. The data was captured and recorded during each run. A minimum of five tests

were completed for each type of sample pollutant. The test was considered finished when the

USV either captured the floating debris or missed the floating debris. This test was performed for

each of the sample pollutants outlined in Chapter three.

CHAPTER 6: RESULTS AND DISCUSSION

6.1   USV Velocity

The velocity test was the first to be accomplished. TABLE 6-1 displays the average

velocities for each respective input signal. FIGURE 6-1 provides a visual representation of the

data seen in TABLE 6-1. The USV velocity was linear in both directions. The max forward

velocity of the USV was found to be 5.1 feet per second. This was when the motor controller was

providing a full 12 V to the drive motor. The max reverse velocity was found to be 4.0 feet per

second. The difference in these maximum velocities can be attributed to the motor propeller

design.

TABLE 6-1: Average velocity values

Duty Cycle	Velocity (ft/s)
0.330	4.0
0.400	2.4
0.450	1.2
0.500	0.0
0.525	0.6
0.550	1.9
0.575	2.9
0.600	3.5
0.625	4.6
0.660	5.1
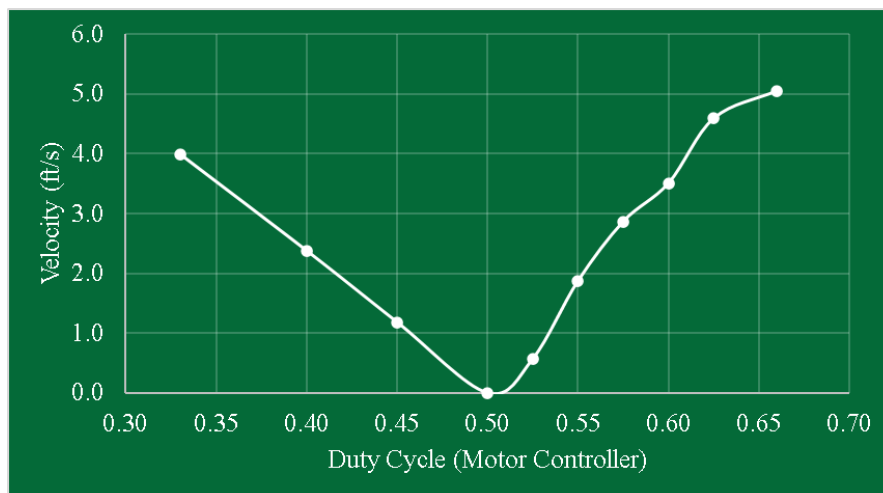
FIGURE 6-1: Velocity as a function of duty cycle

6.2   RSDC Calibration Accuracy

During calibration, key discrepancies between theoretical values and actual values were noticed.

The theoretical maximum distance the RSDC could see, either to the left or right, should be

equal to the max distance that it can see out in front, in this case, 24 feet. TABLE 6-2 presents

the theoretical coordinate values with their respective real-world values. The maximum distance

the RSDC was able to see to the left was slightly over 19 ft compared to the expected value of 24

ft. The maximum distance to the right was approximately 22 ft. The difference between these

two values could be attributed to how the RSDC was mounted to the USV frame. However, this

overall range between the maximum distance to the right and the left would not change. This

range decreased from the theoretical calculation of 48 ft to 41 ft.

TABLE 6-2: Theoretical Vs actual values used during calibration

Position	Theoretical Real-World Coodinates (ft,ft)	Actual Real-World Coodinates (ft,ft)
A	(-24,24)	(-19.25,24)
B	(-12,24	(-10,24)
C	(0,24)	(0,24)
D	(12,24)	(10,24)
E	(24,24)	(22.3,24)
F	(-18,18)	(-15.7,18)
G	(0,18)	(0,18)
H	(18,18)	(-17.1,18)
I	(-12,12)	(-11,12)
J	(0,12)	(0,12)
K	(12,12)	(11.3,12)
L	(-6,6)	(-6,6)
M	(0,6)	(0,6)
N	(6,6)	(6,6)

The calibration template created from the values seen in TABLE 6-2 was then tested for accuracy. TABLE A-1 in the appendix presents the 25 random locations chosen that covered an array of locations within the FOV of the RSDC. Each group of coordinates was converted to obtain a relative angle from the center of the USV. The difference between the actual and calibrated angles was calculated. FIGURE 6-2 presents the actual angle (green bar) between the USV and the point of interest and the error (gold bar) obtained between the actual angle and the calibrated angle. Negative angles refer to points of interest located to the front-left of the USV, and positive angles refer to points of interest located to the front-right of the USV.
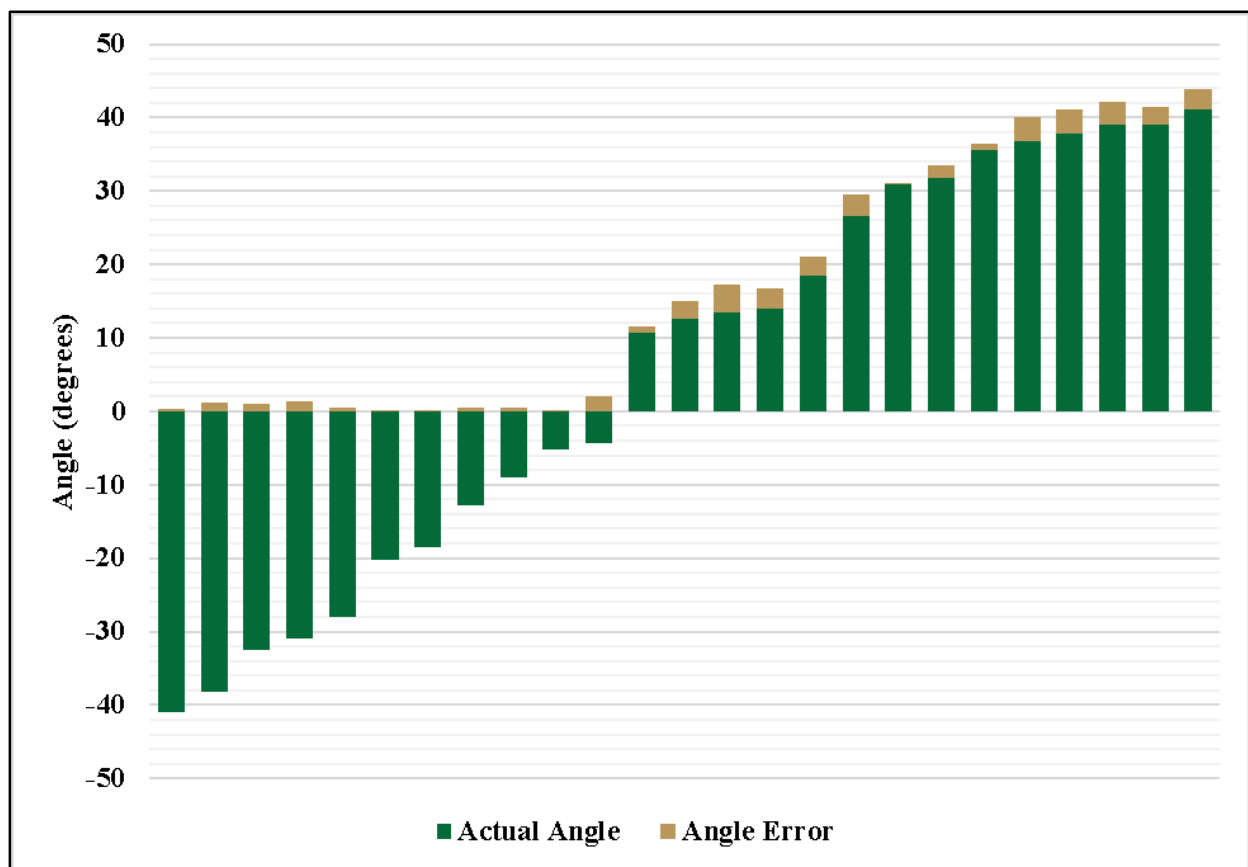
FIGURE 6-2: Angle error experienced in calibration

6.3   Verification Confidence

The main feature of the extraction system is the pattern matching algorithm, which allows the system to decide whether the floating debris was captured or not. This is done by assigning a confidence score from 0-1000 for each captured image. As mentioned in Chapter five, two main algorithms were tested, which alleviated some of the environmental factors that were not an issue during the controlled environment test.

TABLE 6-3 demonstrates the confidence scoring for the extraction mechanism when empty, with a plastic bottle, polystyrene cup, aluminum can, 2-liter bottle, and standard takeout container. These results were under controlled conditions and did not consider any shadowing, lighting changes, or other possible environmental changes that may be experienced during USV operations. These results were captured using the pattern matching algorithm that did not utilize the brightness correction filter. The minimum and maximum scores when the extraction mechanism was empty were 726 and 929.8, respectively. The minimum and maximum confidence scores for when trash was located within the extraction mechanism were 297 and 612, respectively. These values can also be seen in TABLE 6-4. A threshold value of 669 was chosen based on the maximum confidence value when debris was located within the extraction mechanism and the minimum confidence value when the extraction mechanism was empty. The value gives a confidence buffer of 57 in either direction.

TABLE 6-3: Confidence scoring under controlled conditions without brightness correction

Iterations	1	2	3	4	5	6	7	8	9	10	Average
Empty	848	930	875	836	817	776	726	805	838	901	**835**
16 oz plastic bottle	473	476	612	335	477	-	-	-	-	-	**475**
Polystyrene cup	453	411	429	417	297	-	-	-	-	-	**401**
16 oz Aluminum can	305	560	309	306	298	-	-	-	-	-	**356**
2-Liter Plastic bottle	302	372	476	336	425	-	-	-	-	-	**382**
Takeout container	305	339	456	538	582	-	-	-	-	-	**444**

TABLE 6-4: Threshold selection-based on confidence scoring (without brightness correction)

Average Across All Trash	Minimum	Maximum
411.6	297.0	612.0
Average Across Empty Scoop	**Minimum**	**Maximum**
835.1	726.0	929.8

Though this test provided effective results within a controlled environment, that was not the case when the system was moved to the real-world testing environment. The main issue encountered when transiting to the testing environment was shadowing on the pattern. FIGURE 6-3 shows an example of the shadowing experienced within the verification process. This shadowing resulted in excessive false positives using the verification algorithm without brightness correction.
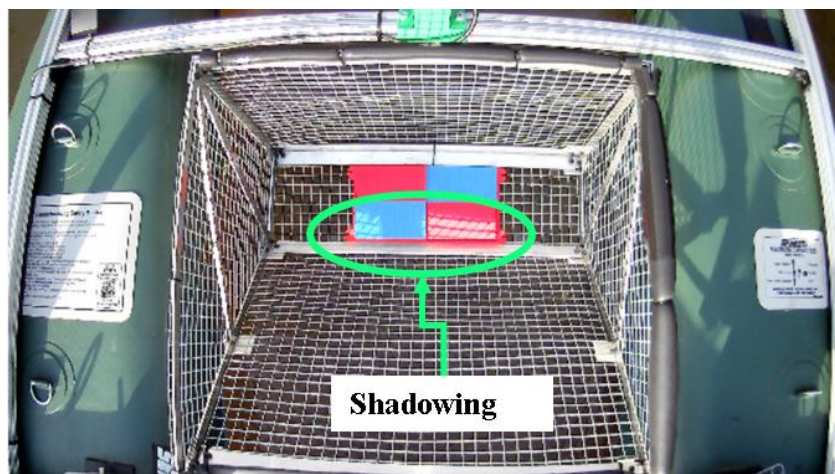
FIGURE 6-3: Shadowing experienced during testing

FIGURE 6-4 shows the image with a corresponding confidence score due to the presence

of the shadowing. As seen in this image, the confidence score was decreased to 370 just from
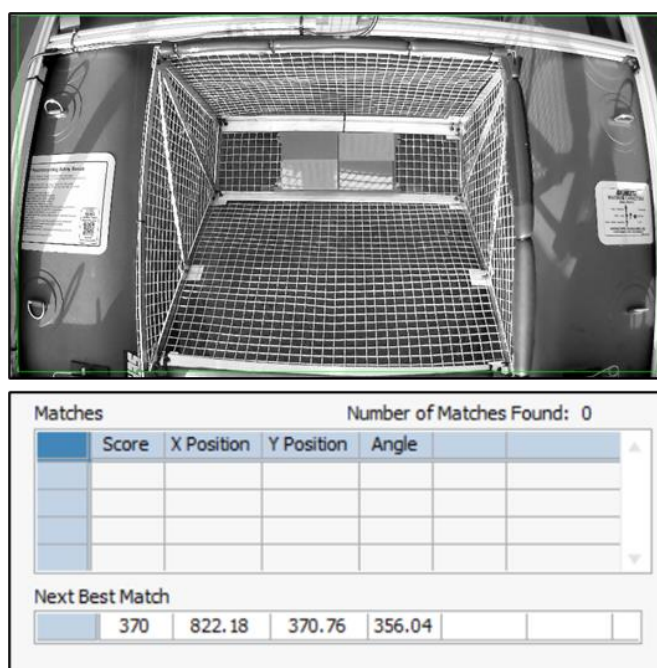
outside lighting and shadowing.

FIGURE 6-4: Confidence score using no brightness correction filter

This same photo was processed using a new script that utilized the brightness correction filter described in Chapter four. FIGURE 6-5 shows the confidence score results of the pattern matching algorithm using brightness correction and the corresponding image. The confidence score was a perfect 1000. One of the critical features illustrated with this image is the lack of shadowing on the pattern, allowing for higher confidence scoring when the extraction mechanism was empty.

Matches				Number of Matches Found: 1	
	Score	X Position	Y Position	Angle	
1	1000	956.00	441.50	0.00	

Next Best Match	
	No Additional Match Found
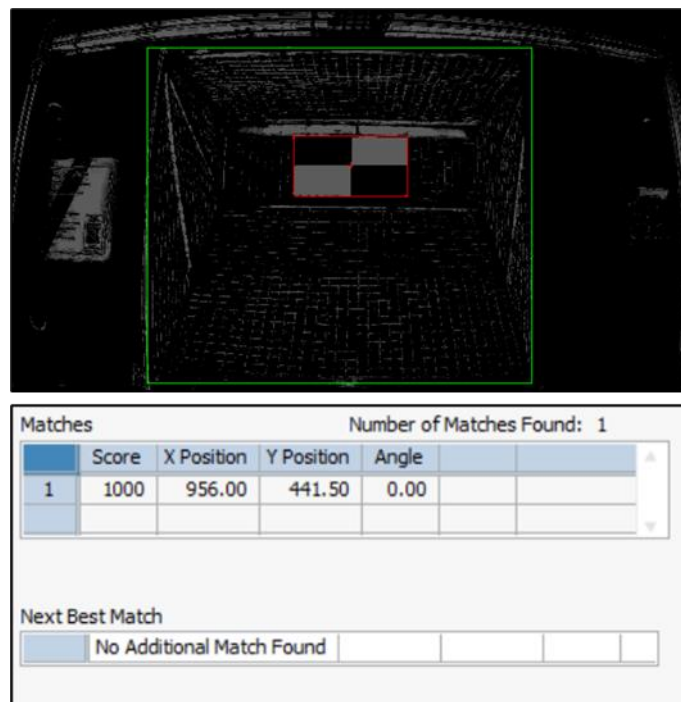
FIGURE 6-5: Confidence score using brightness correction filter

Once the verification algorithm was updated to include the brightness correction filter, data was gathered to determine the correct threshold value to use. TABLE 6-5 shows the results of the confidence scoring test when the extraction mechanism is empty. The average confidence scoring increased drastically compared to the previous results in TABLE 6-3. TABLE 6-6 shows the confidence scoring test when the extraction mechanism had debris located inside. The maximum score increased to 833; however, this was found to be an outlier from the overall data group. When this value was removed, the next highest confidence score was found to be 655.

Also, the average increase in inspection time between when an image had debris and did not was
found to be 0.6 milliseconds.

TABLE 6-5: Empty extraction mechanism confidence scoring

Trial Count	36
Average Confidence Score	927.4
Minimum Confidence Score	862.0
Maximum Confidence Score	1000.0
Standard Deviation	34.6
Average Inspection Time (ms)	22.7

TABLE 6-6: Confidence scoring with debris in extraction mechanism

Trial Count	16
Average Confidence Score	527.3
Minimum Confidence Score	233.0
Maximum Confidence Score	833.0
Standard Deviation	136.2
Average Inspection Time (ms)	22.1

During the confidence scoring, the relative center X and Y coordinates of the best-found
match are also displayed. FIGURE 6-6 shows the distribution of the center coordinate when the
extraction mechanism was empty. The standard deviation for the X and Y coordinates were 6.3
pixels and 21.2 pixels, respectively. This data was over 36 separate tests.

FIGURE 6-6: Matched pattern's center coordinate distribution (empty)

FIGURE 6-7 shows the distribution of the center coordinate when the extraction mechanism had debris inside. The standard deviation for the X and Y coordinates were 136.1 pixels and 101.1 pixels, respectively. This data was over 16 separate tests encompassing all 5 sample variations.
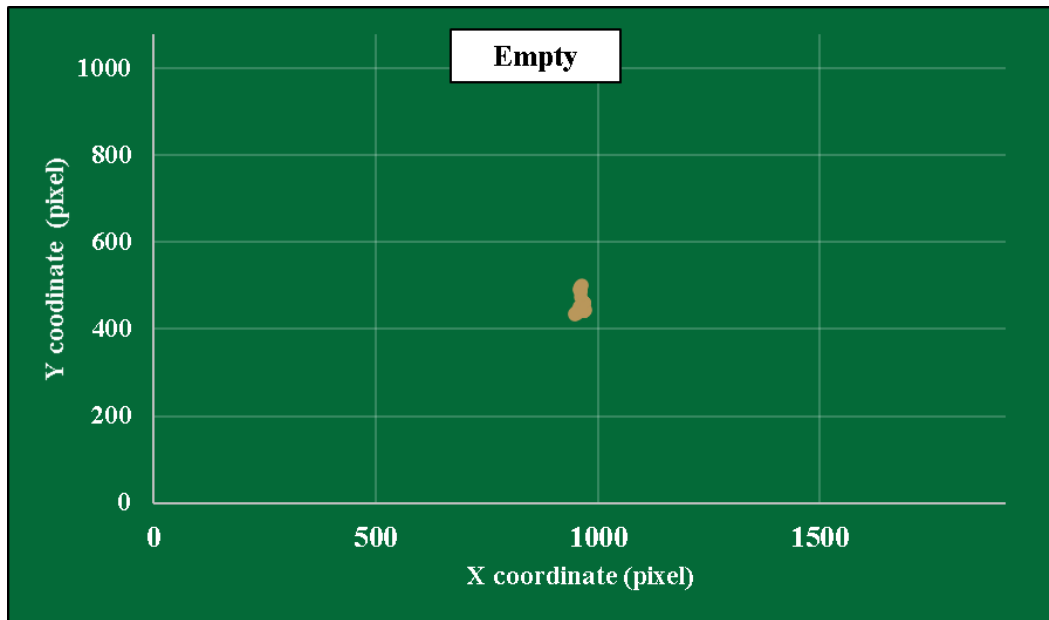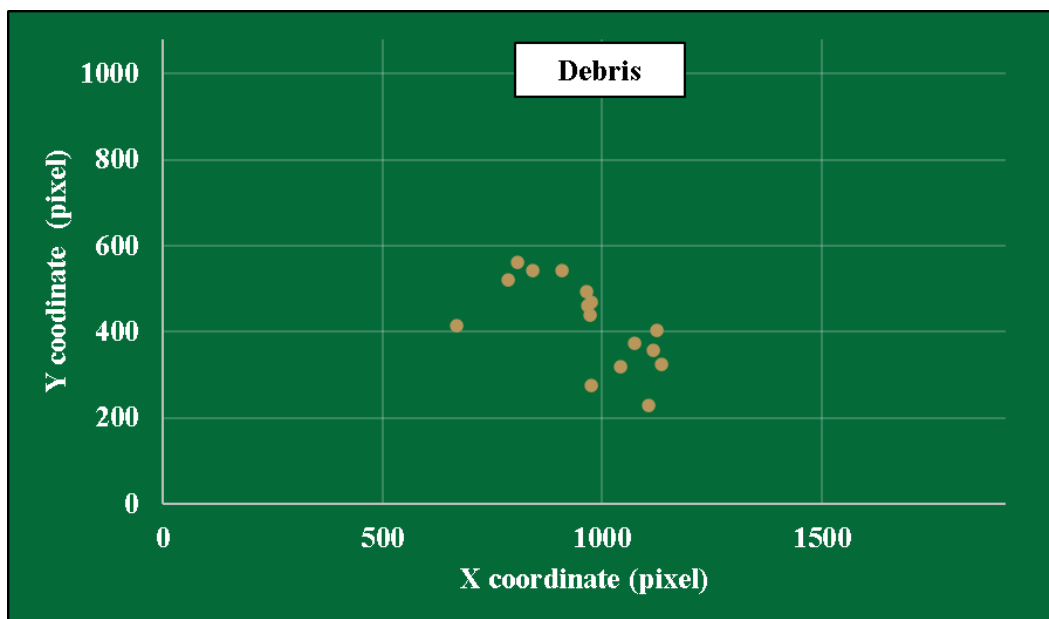

FIGURE 6-7: Coordinate distribution of next best match (with debris)

6.4   Pollution Discovery Testing

During operation, the USV logged each photo captured by the RSDC. These photos were then analyzed to determine the overall effectivity of the discovery algorithm for each of the pollutants. The first pollutant that was examined was the polystyrene cup. This pollutant provided the overall best results. The minimum recognizable particle size of the polystyrene cup was 209 and had an approximate location of -2 ft,19.5 ft (X and Y). This was also the furthest away from the USV that the polystyrene cup was detected. The average detection distance was found to be 16.2 ft. The debris size increased as the USV approached it. The average pixel area for the polystyrene cup was 4254 pixels^2. FIGURE 6-8 shows the trend that the overall particle area as the distance to the USV decreased. Several key aspects of the graph are the exponential trend that the function followed and the distance to the USV being negative. This is because the coordinate system is located at the front of the USV while the RSDC camera is mounted 1.5 feet from the front, allowing for object distance to register as negative. It should be noted that these values also varied with object orientation.
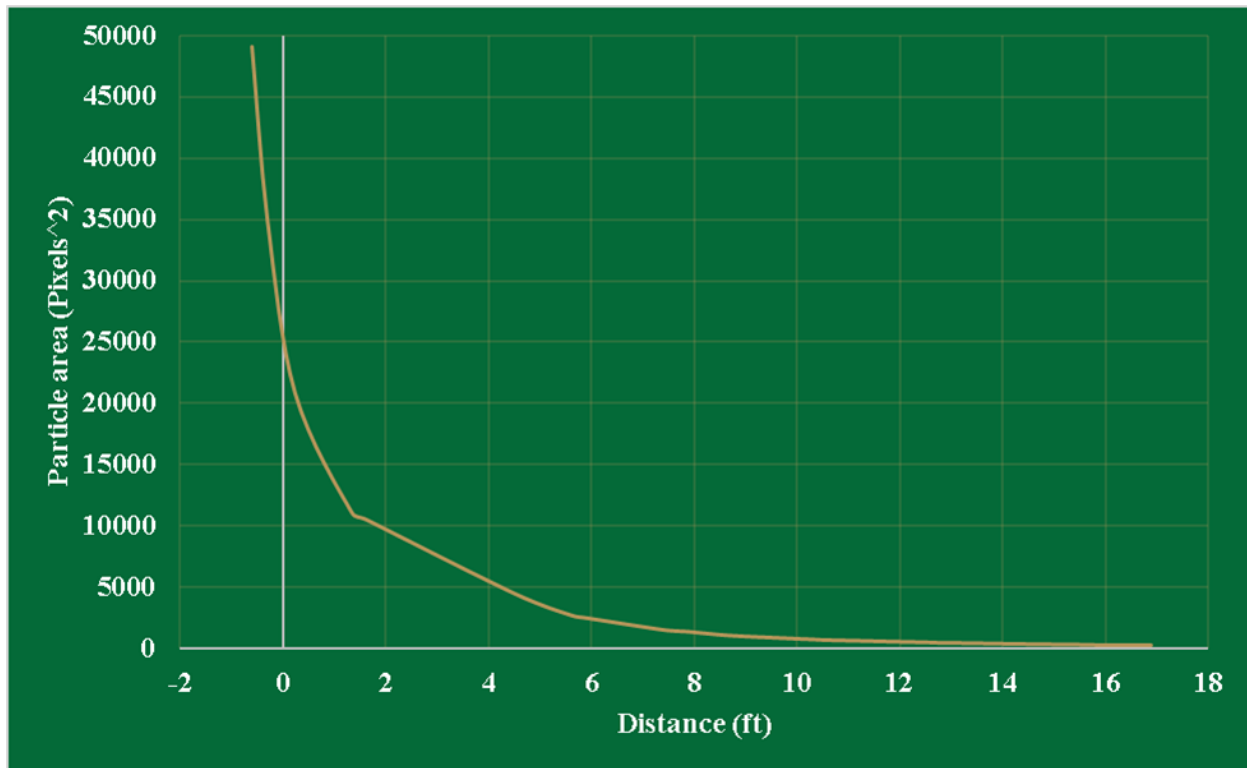
FIGURE 6-8: Pixel area as a function of distance from USV (Polystyrene cup)

Also examined was the percentage that the centroid extracted matched the centroid of the actual floating debris. The match percentage was found to be 90.9%, with only 25 out of 275 images not matching. The cause of this inaccuracy was due to possible reflections that were not filtered out effectively. Over 17 different runs, the maximum number of times that the centroid did not match in a given run was ten times. If this one run were removed from the data pool, the overall accuracy would increase to 94.5%. Also examined was the possibility that one of the filters removed the floating debris from the image resulting in detection errors. For the polystyrene cup, the percentage that one of the filters removed the floating debris from the image was 10.9%. From this 10.9%, 60% was from removing border particles, 27% was from removing particles with an area less than 200 pixels^2, and the remaining 13% was distributed between the erosion filter and removing small objects morphology filter.

The next major sample pollutant tested was the standard takeout container. The maximum pixel area for this debris was 57486 pixels^2 and was located at -0.35 ft, -0.09 ft. The minimum pixel area value captured was 248 pixels^2 and was located 22.48 ft in front of the USV. The average detection distance for the takeout container was 21.9 ft. This was the furthest any debris was detected. This was due to the standard takeout container being the largest of any of the samples. The average pixel area for the takeout container was 5552 pixels^2. FIGURE 6-9 shows the exponential increase in pixel area as the debris approaches the USV.

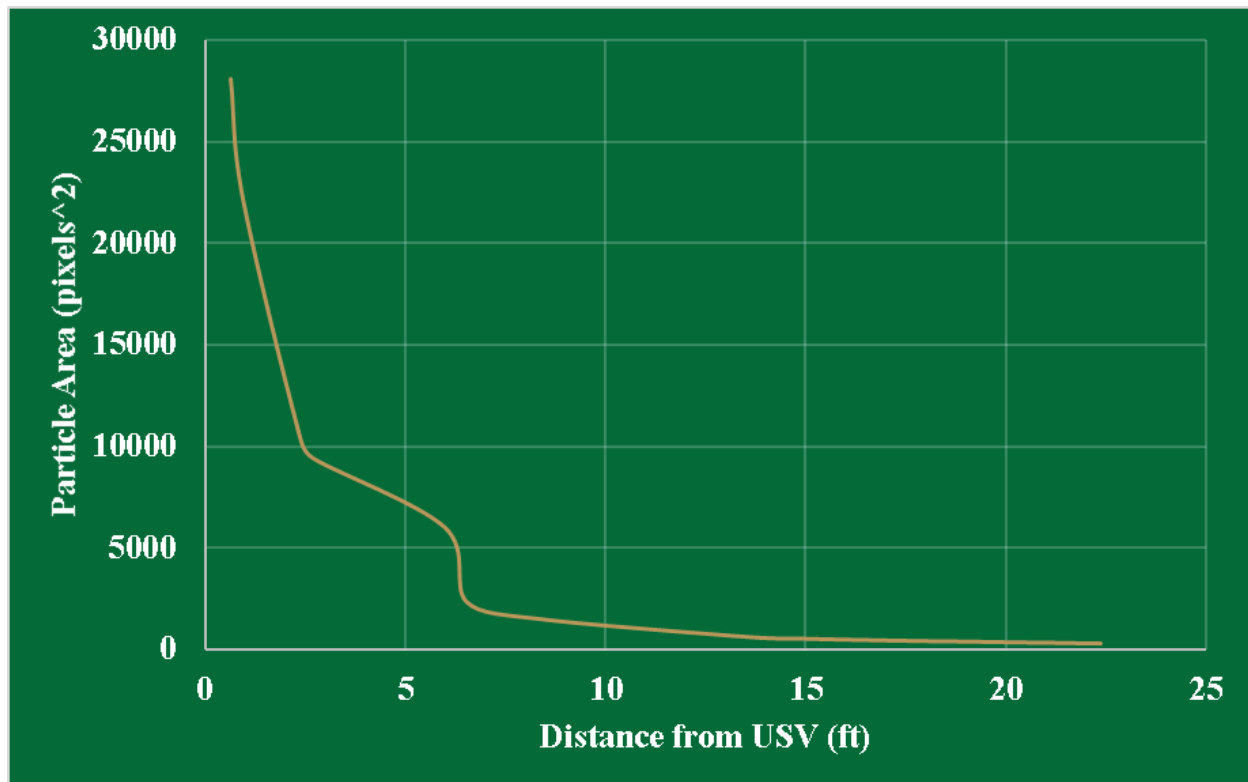*FIGURE 6-9: Pixel area as a function of distance (standard takeout container)*

For the takeout container, the percentage that the actual debris centroid matched that of the extracted centroid was found to be 87.7%. Following this, the percentage of images that filtered out the object was 10.2%, 5.1% due to removing border objects, and the other 5.1% due to the removal of small objects transformation.

For the plastic 2-liter bottle, all the previous values were analyzed. The average detection distance was 8.8 ft. The max distance that a 2-liter bottle was detected was approximately 13 ft and had a pixel area of 215. The greatest pixel area value for the 2-liter bottle was found to be over 13000. The average pixel area for the 2-liter bottle was 2586 pixels^2. FIGURE 6-10 shows the exponential increase in pixel area for the 2-liter bottle as it approaches.
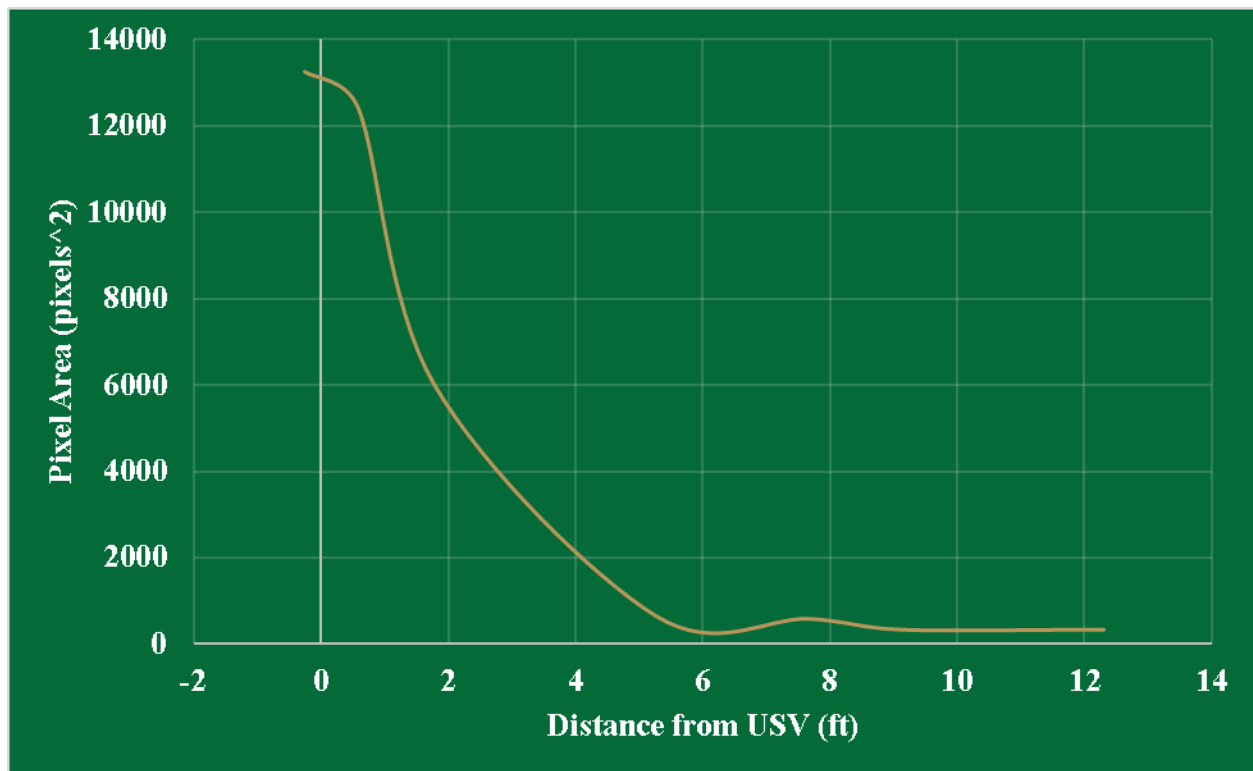
FIGURE 6-10: Pixel area as a function of distance (2-litter plastic bottle)

From the captured images, the plastic bottle was removed through filtering 51% of the time. Of this 51%, 26% was removed due to the removal of hole transformation, 20% from the erosion filter, and the remaining 5% percent split between the particle filter and removal of border objects. Though this percentage was higher than anticipated, removing all instances in which the filter removed the object before the object was even discovered in the image, the percentage drops to 28%, which means that 7 out of 10 images will not filter out the 2-liter

bottle. The percentage in which the perceived centroid differed from the actual percentage was 5%.

The remaining two sample pollutants were the 16-20oz plastic bottle and 16oz aluminum can. The average detection ranges for the 16 oz plastic bottle and aluminum can was 7.16 ft and 13.3 ft, respectively. There was an overall decrease in detection distance from the previously observed pollutants. This can be attributed to the overall size of the aluminum can and plastic bottle. The reason that the aluminum can had a slightly larger detection range was due to the reflectivity of the aluminum and the utilization of the brightness correction filter within the discovery algorithm. The average pixel area for the 16 oz plastic bottle and aluminum can was 710.8 pixels^2 and 809.5 pixels^2, respectively. This again was drastically smaller than the previously tested samples. The removal of small objects transformation was the largest contributor to the reduction in the detection distance.

6.5   Operational Results

FIGURE 6-11 demonstrates a plot of each coordinate extracted from the images captured by the RSDC when trying to locate the polystyrene cup. A flow of every image used to create FIGURE 6-11 can be seen in the Appendix as FIGURE A-3. As the cup became further from the center, the USV began adjusting to realign itself with the debris. Due to the USV being started from a dead rest, more images were captured further away from the USV than close-up. The major direction came when the object reached an AOA greater than 22.5 degrees.

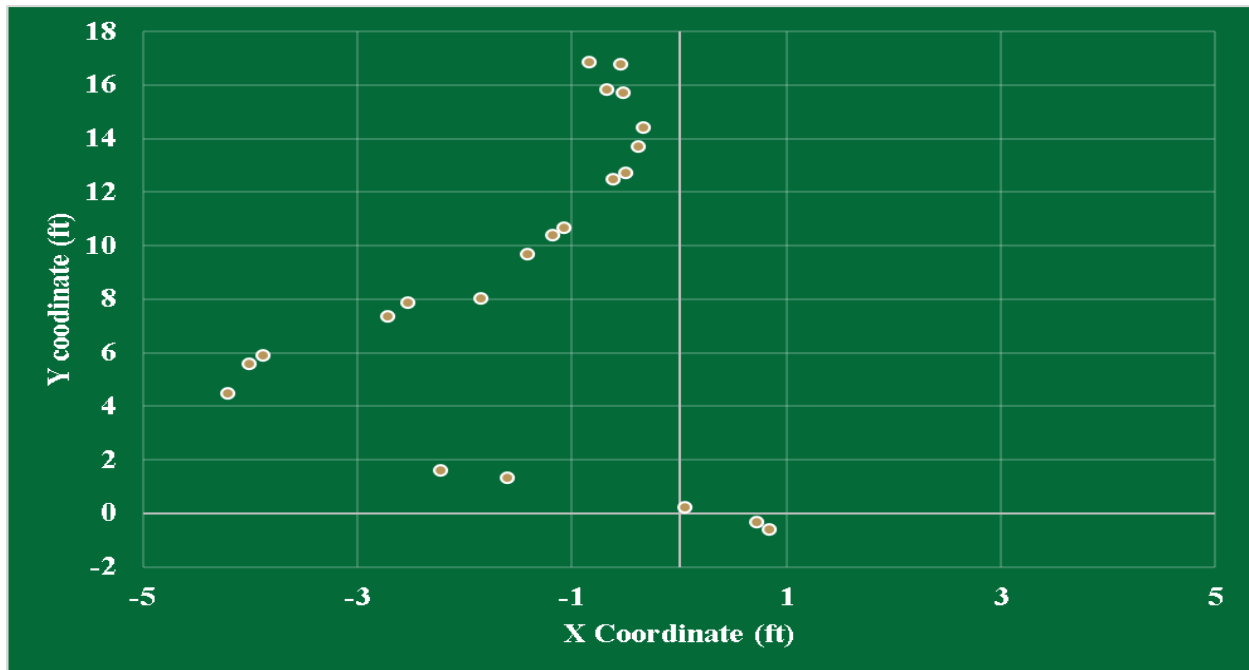*FIGURE 6-11: Polystyrene cup successful capture coordinate plot*

FIGURE 6-12 demonstrates the coordinate set corresponding with a successful extraction operation of the standard takeout container. As the USV detected the object, it began to turn right, overshooting the object but then readjusting before capturing.
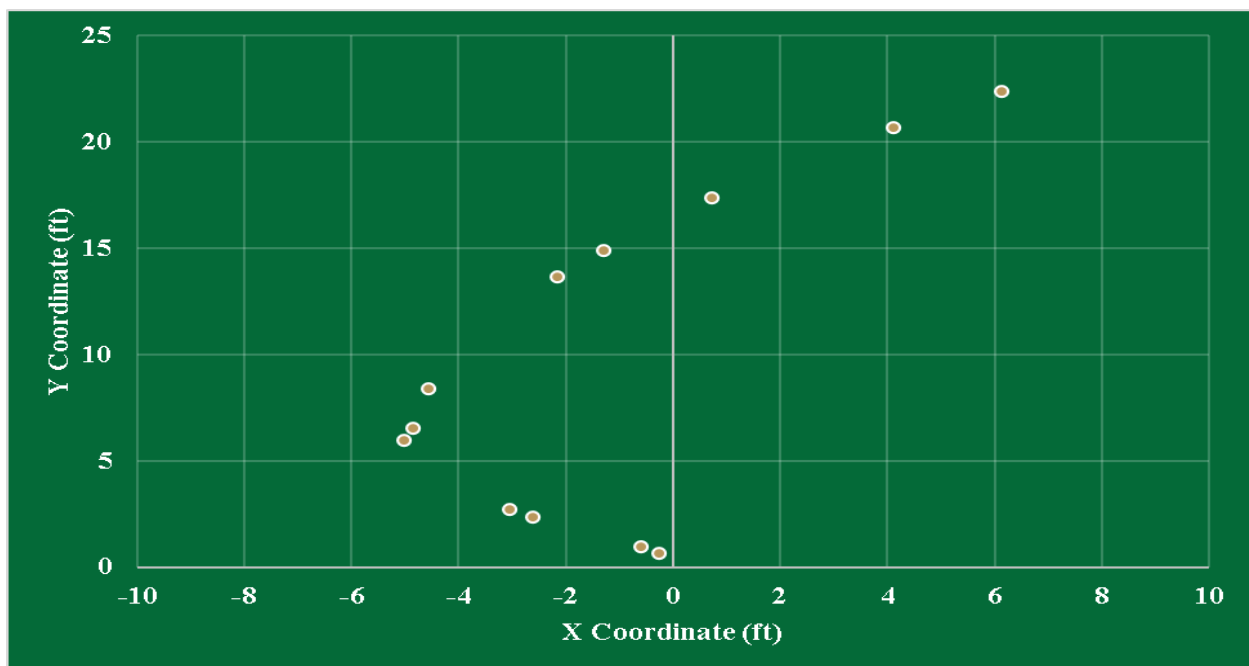
FIGURE 6-12: Standard takeout container successful capture coordinate plot

94

FIGURE 6-13 shows a coordinate plot of successful extraction of the plastic 2-liter bottle. There were significantly fewer coordinate plots due to the USV not locating the debris until it was 12 ft out front of it. Again, as soon as the USV recognized the debris, it began turning to the left before eventually capturing the debris just inside the left hull.
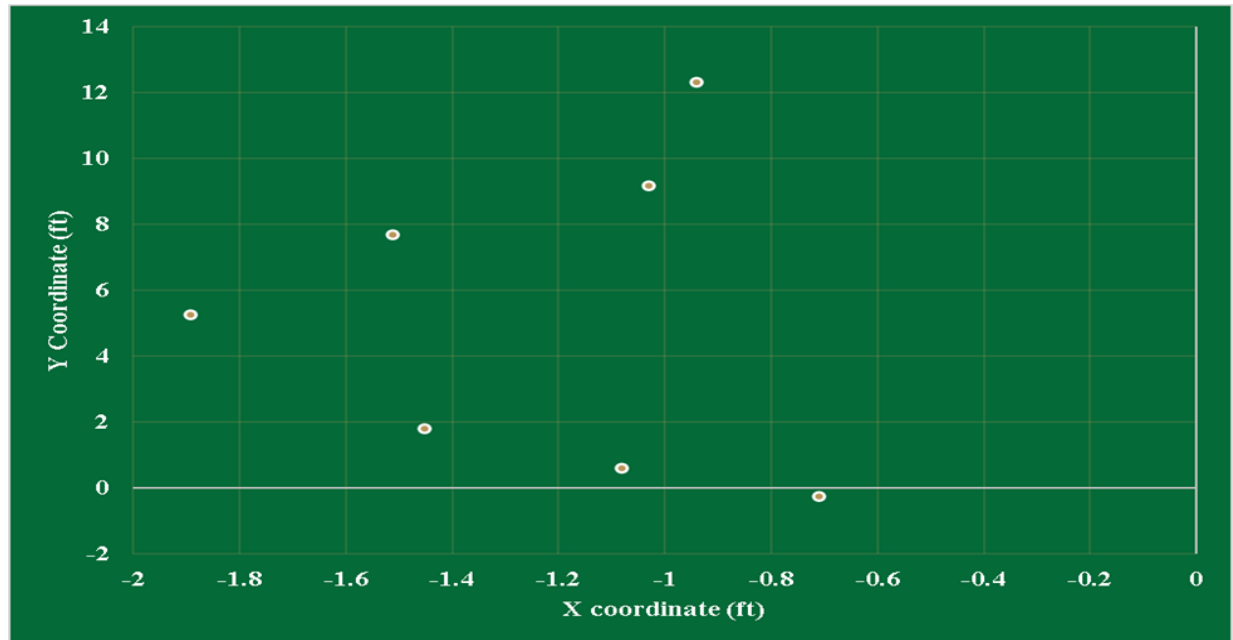
FIGURE 6-13: Plastic 2-liter bottle successful capture coordinate plot

FIGURE 6-14 shows the duty cycle of the signal input from the myRIO to the servo motor with the white line. The extracted centroid locations of the floating debris can be seen by the gold bars. The numbers located across the bottom of FIGURE 6-14 correspond to images captured from the discovery system. FIGURE 6-15 shows the corresponding images for a successful capture of the polystyrene cup. As the discovery system captured images, the floating debris was located to the left of the USV. This required the servo to adjust the USV heading for a left turn. Following this, the debris was located to the right of the USV from overcorrection. This required the servo to adjust for a right turn before finally capturing the debris between the two USV hulls.
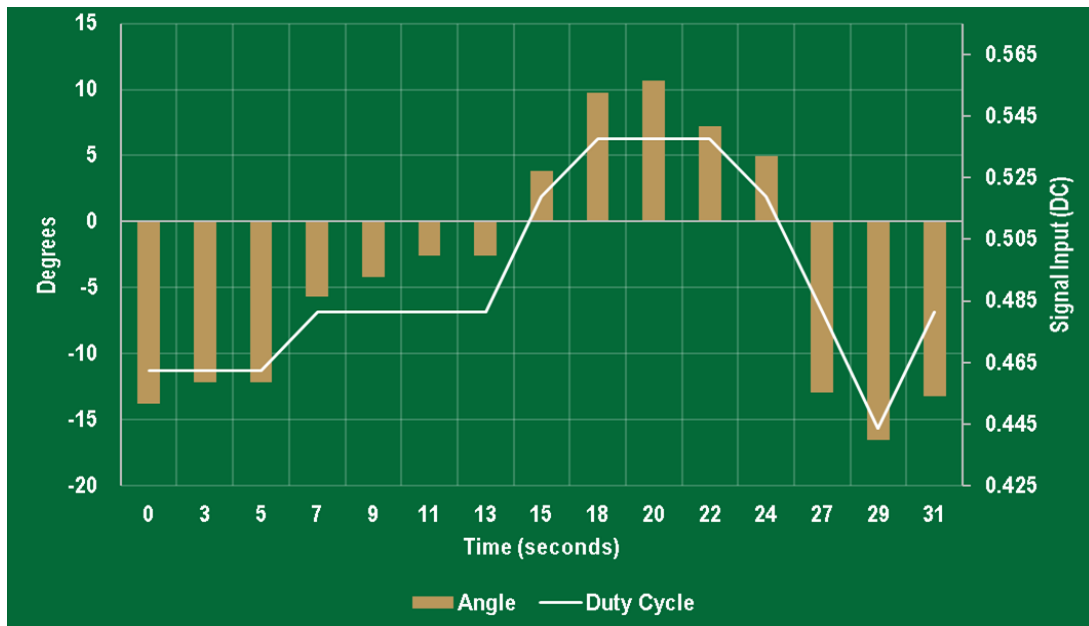
FIGURE 6-14: Servo signal and respective AOA of floating debris relative to USV
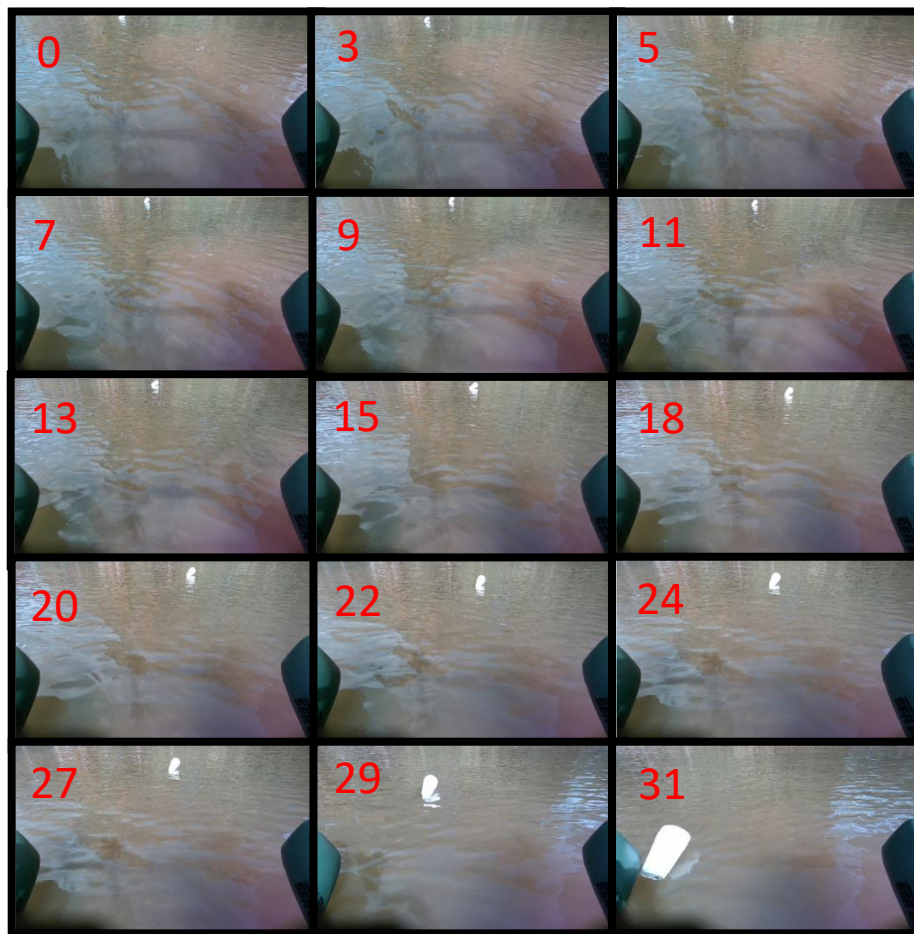
FIGURE 6-15: Corresponding images for each point used in FIGURE 6-14

CHAPTER 7: CONCLUSION

7.1   Summary

The overall objective of this project was to create a proof-of-concept USV that allowed for the autonomous extraction of litter from aquatic environments. To accomplish this task, a vision-based approach was exploited. Vision sensors were used for both the object discovery and verification steps. The overall control of the USV was accomplished using the myRIO. The myRIO allowed for independent control of each main driving system; servo motor stepper motor, and motor controller. This system allowed the USV to maneuver the swim lane as intended adjusting its path as necessary.

The vision system was successful in locating all five separate test samples within the aquatic environment. Each sample provided different results for detection distance, source of error, and how accurate centroid extraction was. As expected, the larger samples of pollutants provided better repeatability. The polystyrene cup and standard take-out container had the farthest detection ranges, 19.5 ft and 22.5 ft, respectively. In comparison, the 16 oz plastic bottle and aluminum had a maximum detection range of 14.8 ft and 18.7 ft, respectively. The average detection distance for the smaller objects decreased compared to that of the polystyrene cup and takeout container. One of the main aspects of this was the number of pixels the debris covered in an image at different distances. Due to how the filtering process was set up, smaller objects would be removed early on. This allowed the excess background to be removed but came at a cost. The largest pixel area covered was from the standard takeout container, taking up over 57,000 pixels. The smallest pixel area that was accurately captured was 209. The reason no

object was detected under this threshold was directly due to the last filter applied in the object discovery algorithm.

The second vision system utilized pattern matching techniques to determine whether or not the located debris had been extracted from the environment. During testing, several changes were made to account for factors such as shadowing and lighting changes. Utilizing the brightness correction filter within LabVIEW Assistant, an average confidence level of 927.4 was found, and this was an increase of 92.4 over the previous algorithm. Based on the response of the pattern matching algorithm, the extraction mechanism was able to either dispose of the debris or redeploy. This system provided extreme repeatability by utilizing the NEMA23 stepper motor. This repeatability could be seen by the standard deviation of the center coordinates of the pattern when the scoop was empty.

The final OLARP design was capable of detecting the sample pollutants through the implementation of the object discovery system. As seen in the results from Chapter six, the detection range was 0 ft to 22.5 ft and was directly related to that of the overall size of the pollutant being located. Due to the variations of pollution size and location, the object discovery system provided a unique solution that did not require the size and location to be pre-determined. The control system assisted in this solution as well by utilizing the information captured within the object discovery system. This was only part of the solution. Due to the long-lasting effects that pollution has on the aquatic environment, the only practical solution was removing the pollution once it was located. This was accomplished through the implementation of the extraction and verification systems. These systems aloud for the USV to autonomously extracted and verified that the sample pollutant had been extracted from the aquatic environment once

detected. Each of these systems working collectively, aloud for a successful prototype system that autonomously detected and extracted floating pollution from the aquatic environment.

7.2   Future Work and Other Applications

Several features could be added to the OLARP design to improve overall functionality in future work. The primary system to make this design whole would include a navigation system and an obstacle avoidance system; LIDAR could be implemented to help detect and avoid obstacles above the water. Sonar transducers are the key feature to depth finders found on boats and could be implemented into this design to help maneuver in shallow waters where most debris accumulates. Once components like these are incorporated into the design, the search area could transition from a swim lane to a search grid. Things like unscented Kalman filters and extended Kalman filters could also be implemented within the navigation scheme of the USV, improving overall accuracy.

One of the major issues encountered throughout this research was being able to extract miscellaneous information that presented itself as noise within images. This included everything from leaves to water reflection. Improvement to the proposed design could come from creating a database of different filters that could be applied for any given situation. As the environment and lighting change, machine learning could be implemented to detect refection and adjust the USV accordingly.

Other applications for design can range from tackling environmental issues to military applications. Depending on the suite of sensors added to the USV design, it could perform water testing to human extraction. Other applications include marine animal tracking, ocean floor

mapping, and even boat hull inspections. The applications of a USV design are endless, each

using its own suite of sensors to accomplish a given task.

REFERENCES

[1]   Spaargaren, L., *The Bubble Barrier.* 2018.

[2]   Borrelle, S.B., et al., *Predicted growth in plastic waste exceeds efforts to mitigate plastic pollution.* 2020. vol. 369(6510): p. 1515-1518.

[3]   Dufau, C., et al., *Satellite Solutions for Tracking Litter & Plastic Pollution in the Ocean.* IEEE, 2019: p. 1-5.

[4]   Moore, C., *Plastic Pollution.* Britannica, 2021.

[5]   Angnunavuri, P.N., F. Attiogbe, and B. Mensah, *Consideration of emerging environmental contaminants in africa: Review of occurrence, formation, fate, and toxicity of plastic particles.* ELSEVIER, 2020: p. 14.

[6]   McCarthy, N., *The World's Oceans Are Infested With Over 5 Trillion Pieces Of Plastic.* 2017.

[7]   Gray, A., *Around 90% of all river-borne plastic that ends up in the ocean comes from just 10 rivers.* 2018.

[8]   Jambec, J., *Plastic waste inputs from land into the ocean.* AAAS, 2015. vol.347: p. 768-771.

[9]   Gall, S.C. and R.C. Thompson, *The impact of debris on marine life.* PubMed, 2015.

[10]   Laist, D.W., *Impacts of Marine Debris: Entanglement of Marine Life in Marine Debris Including a Comprehensive List of Species with Entanglement and Ingestion Records.* Springer-Verlag New York, 1997: p. 99-139.

[11]   UNESCO, *The current status of ocean science around the world* Global ocean science report 2017.

[12]   Cheshire, A., et al., *UNEP/IOC Guidelines on Survey and Monitoring of Marine Litter.* 2009: p. 1-131.

[13]   Hanke, G., *Guidance on Monitoring of Marine Litter in European Seas.* Publications
         Office of the European Union,, 2013: p. 1-128.

[14]   Lippiatt, S., S. Opfer, and C. Arthur, *Marine Debris Monitoring and Assessment:*
         Recommendations for Monitoring Debris Trends in the Marine Environment. NOAA
         Technical Memorandum, 2013: p. 1-88.

[15]   Bernardini, G., A. McConville, and A. Castillo, *Macro-plastic pollution in the tidal*
         Thames: An analysis of composition and trends for the optimization of data collection.
         ELSEVIER, 2020: p. 1-9.

[16]   Blettler, M.C.M., et al., *Massive plastic pollution in a mega-river of a developing*
         country: Sediment deposition and ingestion by fish (Prochilodus lineatus). ELSEVIER, 2019:
         p. 1-10.

[17]   Emmerik, T.v., et al., *Crowd-Based Observation of Riverine Macroplastic Pollution.*
         Frontiers, 2020: p. 1-12.

[18]   Monteiro, R.C.P., J.A.I.d. Sul, and M.F. Costa, *Plastic pollution in islands of the Atlantic*
         Ocean. ELSEVIER, 2018: p. 103-110.

[19]   Blettler, M.C.M., et al., *Freshwater plastic pollution: Recognizing research biases and*
         identifying knowledge gaps. ELSEVIER, 2018: p. 416-424.

[20]   Blettler, M.C.M., et al., *Plastic pollution in freshwater ecosystems: macro-, meso-, and*
         microplastic debris in a floodplain lake. 2017: p. 582-594.

[21]   Esiukova, E., *Plastic pollution on the Baltic beaches of Kaliningrad region, Russia.*
         ELSEVIER, 2016: p. 1072-1080.

[22]   Connors, E.J., *Distribution and biological implications of plastic pollution on the*
         fringing reef of Mo'orea, French Polynesia. 2017: p. 1-14.

[23]   Emmerik, T.v., et al., *Seasonality of riverine macroplastic transport.* 2019: p. 1-9.

[24]   Dris, R., *First assessement of sources and fate of macro and micro plastics in urban*
         hydrosystems : Case of Paris megacity. 2017: p. 1-271.

[25]   Sharma, S.C.S., *Microplastics in our oceans and marine health.* The journal of field actions, 2019.vol.19: p. 1-9.

[26]   Ducan, E.m., et al., *Message in a bottle: Open source technology to track the movement of plastic pollution.* IEEE, 2020: p. 1-13.

[27]   Sebille, E.v., et al., *A global inventory of small floating plastic debris.* IOP Publishing 2015: p. 1-12.

[28]   Sebille, E.v., M.H. England, and G. Froyland, *Origin, dynamics and evolution of ocean garbage patches from observed surface drifters.* IOP Publishing 2012: p. 1-7.

[29]   Legler, D.M., et al., *The current status of the real-time in situ Global Ocean Observing System for operational oceanography.* Journal of Operational Oceanography, 2015: p. 189-200.

[30]   Critchell, K., et al., *Modelling the fate of marine debris along a complex shoreline: Lessons from the Great Barrier Reef.* ELSEVIER, 2015: p. 414-426.

[31]   Block, I., *Four technologies tackling the problem of plastic pollution in rivers.* 2019.

[32]   Liu, Z., et al., *Unmanned surface vehicles: An overview of developments and challenges.* ELSEVIER, 2016: p. 71-93.

[33]   Campbell, S., W. Naeem, and G.W.Irwin, *A review on improving the autonomy of unmanned surface vehicles through intelligent collision avoidance manoeuvres.* ELSEVIER, 2012: p. 267-283.

[34]   Roberts, G.N. and R. Sutton, *Advances in unmanned marine vehicles* 2006: p. 1-433.

[35]   Breivik, M., *Topics in Guided Motion Control of Marine Vehicles.* Thesis, 2010: p. 1-226.

[36]   Caccia, M., et al., *Sampling Sea Surface With SESAMO.* 2005: p. 1-11.

[37]   Rasal, K., *Navigation & control of an automated SWATH surface vessel for bathymetric mapping.* 2013: p. 1-80.

[38]   Murphy, R.R., et al., *Cooperative Use of Unmanned Sea Surface and Micro Aerial Vehicles at Hurricane Wilma.* Wiley InterScience, 2008: p. 164-180.

[39]   Pastore, T. and V. Djapic, *Improving Autonomy and Control of Autonomous Surface Vehicles in Port Protection and Mine Countermeasure Scenarios.* 2010: p. 1-12.

[40]   Bertram, V., *Unmanned Surface Vehicles – A Survey.* IEEE, 2008: p. 1-14.

[41]   Breivik, M., V.E. Hovstein, and T.I. Fossen, *Straight-Line Target Tracking for Unmanned Surface Vehicles.* 2008. vol. 29: p. 131-149.

[42]   Caccia, M., et al., *Unmanned Surface Vehicle for Coastal and Protected Waters Applications: the Charlie Project.* Marine Technology Society Journal, 2007. vol. 41: p. 1-10.

[43]   Sveck, P. and S.K. Gupta, *Automated synthesis of action selection policies for unmanned vehicles operating in adverse environments.* Springer Science+Business Media, 2011: p. 149-164.

[44]   Kiencke, U., et al., *The impact of automatic control on recent developments in transportation and vehicle systems.* Annual Reviews in Control, 2006: p. 81-89.

[45]   Caccia, M., et al., *Basic navigation, guidance and control of an Unmanned Surface Vehicle.* Springer Science+Business media, 2008. vol. 25: p. 349-365.

[46]   Wang, C., et al., *Hydrodynamic Analysis of a SWATH Planing USV Based on CFD.* IEEE, 2016: p. 1-4.

[47]   Brizzolara, S., et al., *Concept design and hydrodynamic optimization of an innovative SWATH USV by CFD methods.* Springer-Verlag, 2011: p. 227-237.

[48]   Zaghi, S., et al., *Hydrodynamic characterization of USV vessels with innovative SWATH configuration for coastal monitoring and low environmental impact.* ELSEVIER, 2016: p. 1562-1571.

[49]   Zaghi, S., et al., *RANS hydrodynamic characterization of a USV SWATH configuration including design optimization.* ResearchGate, 2015: p. 1-7.

[50]   Lin, Y., Q. Yang, and G. Guan, *Automatic design optimization of SWATH applying CFD and RSM model.* ELSEVIER, 2019: p. 146-155.

[51]   Besl, P.J. and R.C. Jain, *Three Dimensional Object Recognition.* 1985: p. 1-71.

[52]   Klimentjew, D., N. Hendrich, and J. Zhang, *Multi Sensor Fusion of Camera and 3D Laser Range Finder for Object Recognition.* International Conference on Multisensor Fusion and Integration for Intelligent Systems, 2010: p. 1-6.

[53]   Carpenter, C.A., S. Grossberg, and J.H. Reynolds, *ARTMAP: Supervised Real-Time Learning and Classification of Nonstationary Data by a Self-Organizing Neural Network.* Neural Networks, 1991.vol. 4: p. 565-588.

[54]   Ecemis, M.I. and P. Gaudiano, *Object recognition with ultrasonic sensors.* 1999: p. 250-255.

[55]   Praczyk, T., *Neuralanti-collisionsystemforAutonomousSurfaceVehicle.* ELSVIER, 2014: p. 559-572.

[56]   Zereik, E., et al., *Priority Task Approach for USVs' Path Following Missions with Obstacle Avoidance and Speed Regulation.* 2015: p. 25-31.

[57]   Motwani, A., et al., *Interval Kalman Filtering in Navigation System Design for an Uninhabited Surface Vehicle.* THE JOURNAL OF NAVIGATION, 2013. vol. 66: p. 639-652.

[58]   Zhang, P., et al., *Navigation with IMU/GPS/Digital Compass with Unscented Kalman Filter.* International Conference on Mechatronics & Automation, 2005: p. 1497-1502.

[59]   St-Pierre, M., D. Gingras, and D. Ing, *Comparison between the unscented Kalman filter and the extended Kalman filter for the position estimation module of an integrated navigation information system.* IEEE Intelligent Vehicles Symposium, 2004: p. 831-835.

[60]   Onunka, C., R. Stopfourth, and G. Bright, *Probabilistic Uncertainty Identification Modelling in USV Obstacle Detection.* ResearchGate, 2013: p. 1-9.

[61]   Dorodnicov, S., *The Basics of stero Depth Vision.* 2018.

[62]   Briggs, B.N., *Vector-Based Mecanum- Drive Robotic system with machine vision and sensor fusion for soccer training* 2019: p. 120.

APEENDIX: SUPPLEMENTARY INFORMATION

Peak Current	RMS Current	SW1	SW2	SW3
1.00A	0.71A	ON	ON	ON
1.46A	1.04A	OFF	ON	ON
1.91A	1.36A	ON	OFF	ON
2.37A	1.69A	OFF	OFF	ON
2.84A	2.03A	ON	ON	OFF
3.31A	2.36A	OFF	ON	OFF
3.76A	2.69A	ON	OFF	OFF
4.20A	3.00A	OFF	OFF	OFF

FIGURE A-1: STEPPERONLINE current combinations

Microstep	Steps/rev.(for 1.8°motor)	SW5	SW6	SW7	SW8
2	400	OFF	ON	ON	ON
4	800	ON	OFF	ON	ON
8	1600	OFF	OFF	ON	ON
16	3200	ON	ON	OFF	ON
32	6400	OFF	ON	OFF	ON
64	12800	ON	OFF	OFF	ON
128	25600	OFF	OFF	OFF	ON
5	1000	ON	ON	ON	OFF
10	2000	OFF	ON	ON	OFF
20	4000	ON	OFF	ON	OFF
25	5000	OFF	OFF	ON	OFF
40	8000	ON	ON	OFF	OFF
50	10000	OFF	ON	OFF	OFF
100	20000	ON	OFF	OFF	OFF
125	25000	OFF	OFF	OFF	OFF

FIGURE A-2: STEPPERONLINE micro step switch combinations

TABLE A-1: Data used in calculating error in calibration

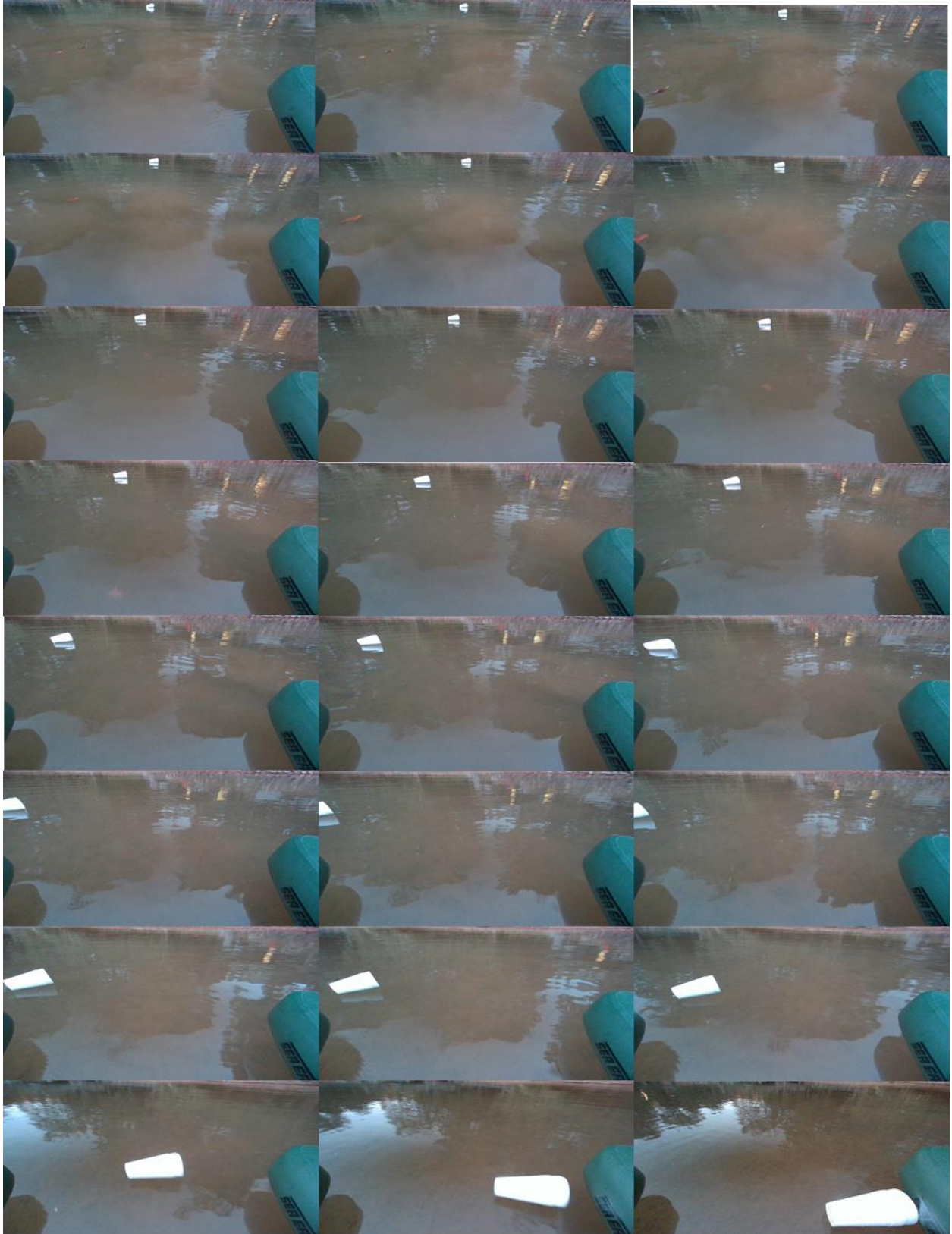| Iteration	Actual X (Ft)	Actual Y (Ft)	Calibrated X (Ft)	Calibrated Y (Ft)
1	-15	19	-15.1	20.0
2	-14	22	-14.7	24.0
3	-13	15	-13.7	16.0
4	-8	15	-8.3	15.8
5	-7	19	-8.1	22.1
6	-5	15	-5.1	15.5
7	-5	22	-5.5	25.0
8	-3	5	-3.1	4.8
9	-3	19	-3.5	21.2
10	-2	22	-2.1	24.3
11	-1	13	-1.4	12.3
12	1	4	1.2	4.1
13	2	9	2.4	9.0
14	2	4	2.3	4.0
15	3	16	3.4	16.8
16	3	9	3.4	8.9
17	3	4	3.4	4.0
18	5	7	4.6	6.2
19	5	21	5.4	17.3
20	6	10	5.5	9.2
21	7	9	7.4	8.5
22	13	21	11.9	18.0
23	13	16	12.4	14.0
24	14	16	13.4	13.9
25	17	21	15.3	21.2

FIGURE A-3: Corresponds with the coordinate display in FIGURE 6-11